Contributions to the FEL'97 Conference, August 18-21, 1997 in Beijing, China

TESLA FEL-Report 1997-06

Contents

Calculation of Coherent Synchrotron Radiation in the TTF-FEL Bunch Compressor Magnet Chicanes

M.Dohlus, T. Limberg

Deutsches Elektronen Synchrotron, Notkestr. 85, 22607 Hamburg, Germany

Abstract
The bunch compression system in the TTF-FEL decreases the bunch length in order to achieve the high peak currents needed for the SASE FEL process. Along the curved trajectories in the bunch compressor magnet chicanes, these short bunches will start to radiate coherently. In this paper, a numerical calculation of the characteristics of this radiation is presented. One-dimensional bunch models are not sufficient for near field effects in particular cannot completely explain the power flow to the EM field, but they can be used to estimate the radiation in the far region. For the calculation of the power flow, in presence of shielding by horizontal conducting planes, and of the far-field, a two-dimensional bunch with time dependent shape was simulated.

1 Introduction

A bunch of ultra-relativistic charged particles radiates incoherent as well as coherent synchrotron light. The incoherent radiation is calculated using a point particle model, leading to the radiated power

$$P_i = \frac{1}{6\pi}\frac{e^2 c_0}{\varepsilon_0}\frac{N\gamma^4}{R_0^2}$$

with N the number of particles, γ the relativistic factor and R_0 the bending radius. As the typical wavelength is of the order of the 'critical wavelength' $\lambda_c = \frac{4\pi}{3}\frac{R_0}{\gamma^3}$, which is usually small compared to the dimensions of the structure and even to the mean particle distance, this radiation is independent of the shape of the vacuum chamber and bunch. In contrast to this, the spectral components with wavelength of the order of the bunch dimensions have to be calculated from a continuous model (e.g.[1, 2]). Although the bunch length needed for FEL applications is significantly smaller than the beam pipe dimensions, the interaction length due to the retarded position of source particles is typically of the order of $L_o = \sqrt[3]{24R_0^2\sigma}$ (with the RMS bunch length σ) and therefore usually not small compared to the chamber size.

In section 2 the coherently radiated synchrotron light power is calculated for bunches in circular motion (CM-case) and the power transfer to the EM field for a TESLA bunch

TESLA FEL-Report 1997-06

compressor III design (BC-case). In both cases the effect of shielding by horizontal perfectly electric conducting (PEC) planes is investigated. For the CM-case with a rigid one-dimensional bunch, compact expressions for the radiated power and its spectrum can be formulated, in which only the shielding functions have to be integrated numerically. The BC-case is much more complex as the essentially two-dimensional charge distribution changes its shape over the hole length of the device. Therefore the E-field in the compressor is integrated numerically for a set of sub-bunches with individual paths.

In the section 3 the electrical far-field in forward direction is derived and time signals as well as spectra are calculated for the BC-case, using the sub-bunch approach.

2 Power Flow to the EM Field

The electrical field $\vec{E}(\vec{r},t)$ of a charge distribution $\rho(\vec{r},t)$ with a given motion $\vec{v}(\vec{r},t)$ can be calculated directly from the retarded potential approach:

$$\vec{E}(\vec{r},t) = -\nabla V - \dot{\vec{A}} = -\nabla \frac{1}{4\pi\varepsilon} \int \frac{\rho(\vec{r}\,',t')}{\|\vec{r}-\vec{r}\,'\|} dV' - \frac{\mu}{4\pi} \int \frac{\dot{\rho}(\vec{r}\,',t')\vec{v}(\vec{r}\,',t')}{\|\vec{r}-\vec{r}\,'\|} dV' \ . \tag{1}$$

This integration can be simplified for the case of a rigid one-dimensional bunch with the charge density $\lambda(s,t) = \lambda(s-\beta ct)$, traveling on a general path $\vec{r}_s(s)$:

$$\vec{E}(\vec{r},t) = \frac{1}{4\pi\varepsilon_0} \int \left\{ \frac{\beta\lambda'}{R} (\beta\vec{e}-\vec{n}) + \frac{\lambda}{R^2}\vec{n} \right\} ds \tag{2}$$

with $\vec{R} = \vec{r} - \vec{r}_s(s)$, $\vec{n} = \vec{R}/R$, $\vec{e} = \partial\vec{r}_s(s)/\partial s$ and $\lambda = \lambda(s+\beta(R-c_0t))$. To avoid the singularity of the kernel, the field is split into $\vec{E}_2 = \vec{E}\,\{\text{path} = \vec{r}_s(s_0) + (s-s_0)\vec{e}(s_0)\}$ and $\vec{E}_1 = \vec{E}\,\{\text{path} = \vec{r}_s(s)\} - \vec{E}_2$. The reference point $\vec{r}_s(s_0)$ is the point of the path which is closest to the observation point. The field $\vec{E}_1$ is integrated numerically while an analytical expression is used for $\vec{E}_2$.

According to Maxwell's equations the total change of electro-magnetic field energy is

$$\frac{d}{dt}W_{\text{field}} = P(t) = -\int \vec{E}(\vec{r},t)\cdot\vec{J}(\vec{r},t)\,dV \ . \tag{3}$$

This includes 'synchrotron light radiation' as well as the change of energy of the field which guides the beam. With the longitudinal electrical field $E(u,t) = \vec{E}(\vec{r}_s(u),t)\cdot\vec{e}(u)$ the power flow caused by an one-dimensional beam can be written as

$$P(t) = -\beta c_0 \int E(u,t)\lambda(u-\beta c_0 t)du \ . \tag{4}$$

2.1 Circular Motion

As the electrical field guiding a rigid one-dimensional bunch in circular motion is stationary, all power $P(t) =: P_c$ is radiated into the far range. The effect of horizontal PEC planes at $z = \pm h/2$ is taken into account by mirror charges $(-1)^\nu\lambda$ at $z = \nu h$. The coherently radiated power is:

$$P_c = \frac{\Gamma(5/6)}{4\pi^{3/2}\sqrt[3]{6}} \frac{e^2 c_0}{\varepsilon_0} \frac{N^2}{R_0^{2/3}\sigma^{4/3}} \cdot S_1\left(\frac{h}{\sqrt[3]{R_0\sigma^2}}\right) \ , \tag{5}$$

with the shielding function

$$S_1(x) = 1 - \frac{\sqrt[3]{6}}{4\Gamma(5/6)} \sum_{\nu=1}^{\infty} (-1)^\nu (\nu x)^{5/2} \int_{-\infty}^{0} e^{-\frac{(\nu x)^3}{4}\left(\frac{s^3}{24}-\frac{1}{2s}\right)} \left(\frac{s^4}{24} - \frac{1}{2}\right) ds \tag{6}$$

as plotted in Fig.1. The essential approximations to derive this formula are: $\sigma \gg \lambda_c$, $\beta \to 1$ and $\lambda(s + R - c_0 t) \simeq \lambda((s-u)^3/24R_0^2 - \nu h/2(s-u) - c_0 t)$ for $s < u$. The same approach leads to the spectral power density

$$p_c(\omega) \propto \sqrt[3]{\omega}\, \mathcal{F}\{\lambda(c_0 t)\}^2 \cdot S_2\left(h \sqrt[3]{\frac{\omega^2}{c_0^2 R_0}}\right) \tag{7}$$

with the spectral shielding function

$$S_2(x) = 1 - \frac{1}{\sqrt[6]{3}\Gamma(2/3)} \sum_{\nu=1}^{\infty} (-1)^\nu \nu x \int_{-\infty}^{0} \sin\left((\nu x)^{3/2}\left(\frac{s^3}{24} - \frac{1}{2s}\right)\right) s ds \ , \tag{8}$$

which is also plotted in Fig.1.

For the end of the TESLA bunch compressor III design (see Tab. 1 where $\sigma = 50\mu$m and $R_0 = 29.233$m) the following values can be calculated: The incoherent radiated power P_i is 0.35W while 54 kW are radiated coherently (P_c). A shielding with horizontal planes $h = 10$mm apart, reduces this radiation to $P_c = 23.3$kW. The half of this power is radiated in the frequency range between 0.81THz and 1.24THz with the maximal spectral density at 0.96 THz.

2.2 TESLA Bunch Compressor III

A third stage of the bunch compression system for the TESLA FEL is composed of a chicane of four magnets with parameters as listed in Tab. 1. Fig. 2 plots the bunch lengths projected in the direction of motion σ_{long} and in the perpendicular direction σ_{trans} along the compressor. For a simulation of the compression process, the bunch has to be synthesized by a set of sub-bunches with the length σ_{sub}, each with a different longitudinal offset at the entrance of the compressor, a different energy and a different path. This approach leads to the two-dimensional charge distribution sketched in Fig. 2. As the field energy of a flat beam in linear motion (with the velocity of light) is

$$W_{\text{linear}} = \frac{q_0}{4\pi^{3/2}\varepsilon_0 \sigma_{\text{ls}}} \ln\left(\frac{\sigma_{\text{ls}}\, C}{\sigma_{\text{sub}}\sigma_{\text{trans}}}\right) \tag{9}$$

with $\sigma_{\text{ls}} = \sqrt{\sigma_{\text{long}}^2 + \sigma_{\text{sub}}^2}$ and C is dependent on the geometry of the beam pipe, the conversion of a 1D to a 2D beam would lead to an infinite loss of field energy (or gain of kinetic energy). To avoid this unphysical behavior of the model, the longitudinal field is observed at a vertical offset of 20μm which corresponds approximately to a transversal width $\sqrt{2/\pi}20\mu\text{m} \simeq 16\mu$m of the sub-bunches (for more details see [1]). The result of a simulation with 500 sub-bunches ($\sigma_{\text{sub}} = 16.7\mu$m) is shown in Fig.3. It has been verified, that the calculated power exchange *in* the compressor (1m$< s <$19m) is insensitive to the parameters of the sub-bunches, but of course the effects at the entrance and exit depend strongly on the transverse dimensions of the bunch before and after compression.

To demonstrate the invalidity of a one-dimensional approach, the power exchange of a single line bunch with the local length as given by Fig.2 is shown as a dashed curve in Fig.3. Especially at the end of the third magnet the $\sigma_{\rm long}(s)$-model underestimates the power transfer. The agreement at the end of the fourth magnet is good because the bunch length is approximately constant and the transverse beam dimensions are defined by the width of the sub-bunches. The small deviation is caused by the slightly longer bunch length $\sqrt{\sigma_{\rm long}^2 + \sigma_{\rm sub}^2}$ of the sub-bunch approach. For the drift spaces, the difference between the one and two-dimensional models can partially be explained by the power flow to space charge fields: $P_s = \partial W_{\rm linear}/\partial\sigma_{\rm trans} \cdot \partial\sigma_{\rm trans}/\partial t$. This formula is valid for an adiabatic transverse compression. As the particle motion in the drift spaces is linear, the field contribution $\vec{E}_2$ describes all effects with exception of the interaction with fields which have been radiated in the arcs. Therefore P_s can also be evaluated by $\int \vec{E}_2 \cdot \vec{J} dV$ which is plotted as a dotted curve in Fig.3.

For the second half of the compressor, the shielding effect of horizontal PEC planes with a separation of h is investigated. Even with shielding, the transfer of kinetic energy to field energy is maximal at the end of the third magnet where the ratio $\sigma_{\rm trans}/\sigma_{\rm long}$ is extreme (see the + curve in Fig.3 and Fig.4). The shielding in the middle of the third drift space seems to be very efficient but this is caused by local interference. At the end of drift space the power flow is approximately P_s which is needed for the energy stored in the near fields. At the beginning of the last magnet a strong oscillation appears until the steady state value is reached as estimated in section 2.1.

3 Far-field Radiation

The far-field radiation to the point $\vec{r}_f = \vec{r}_s(s_0) + X\vec{e}(s_0)$ of a one-dimensional bunch passing the point $\vec{r}_s(s_0)$ is calculated based on the assumption $\vec{n}(s) = \vec{n}(s_0) + O((\delta s/X)^2) \simeq \vec{n}(s_0) =: \vec{n}_0$ for $s_1 \le s \le s_2$. The interval $[s_1, s_2]$ is the location of the retarded bunch. Therefore the field component $E_t = \vec{E} \cdot \vec{e}_t$, perpendicular to the observer-source direction $\vec{n}$, is given by

$$E_t = \frac{1}{4\pi\varepsilon_0} \int R^{-1} \lambda' \sin(\varphi) ds \ , \tag{10}$$

with $\sin(\varphi) = \vec{e}(s) \cdot \vec{e}_t$ and $\beta \to 1$. The factor R^{-1} can be taken as $const = X^{-1}$ only for $s_2 - s_1 \ll X$. Nevertheless this approximation allows a qualitative estimate, even when this condition is not fully satisfied e.g. if X is of the order of few meters. Eqn. (10) is most sensitive to the approximation used in the argument of the line charge density:

$$\lambda' = \lambda' \left(s_0 + X - c_0 t + \frac{1}{2} \int_{s_0}^{s} \varphi(\eta)^2 d\eta \right) \ . \tag{11}$$

A typical property of the far-field is its insensitivity to offsets perpendicular to the source-observer direction, so that only longitudinal properties of the beam ($\propto \sigma_{\rm long}$ see Fig.2) can be detected! To get more information of the compression process in TESLA BC3, one can either compare the radiation from different positions along the chicane or vary the initial energy spread. The time functions and spectra in Fig.5 are calculated by the sub-bunch approach without further simplifications. The radiation in the direction of the drift spaces, caused by the arcs before and behind, is seen as single pulse (curve a and c).

In other directions (e.g. tangential to the 13m position, see curve b) the radiation can be distinguished in time. According to this, the spectrum (curve d) has a strong modulation.

4 Summary

The power flow to the EM field and the far-field radiation of a two-dimensional bunch with time dependent profile has been calculated for a third stage of the TESLA FEL bunch compressor. One-dimensional bunch models are not sufficient to describe near fields, the power flow and the shielding effect by horizontal PEC planes. This has been demonstrated by two examples: 1D bunch in circular motion, 1D bunch in BC3 with local length $\sigma_{\text{long}}(s)$. Especially in the drift spaces, where the bunch changes only its transverse dimensions, a significant contribution of the power exchange is needed for the near field which guides the beam. In contrast to this, the far-field observed in the longitudinal direction is insensitive to transverse bunch dimensions.

References

[1] M.Dohlus, T.Limberg: 'Emittance Growth due to Wake Fields on Curved Bunch Trajectories', FEL Conference, Rome, August 1996, to be published in Particle Accelerators.

[2] M.Dohlus, A.Kabel, T.Limberg: 'Wake Fields of a Bunch on a General Trajectory Due to Coherent Synchrotron Radiation', Particle Accelerator Conference, Vancouver, May 1997.

bunch charge	C	10^{-9}	magnet length	m	3
compression	μm	$250 \to 50$	deflection angle	deg	5.88
energy	MeV	516	length of drift space 1 & 3	m	3
linear energy spread	$\delta E/E$	0.001893	length of drift space 2	m	2

Table 1: Parameters of a design for the third stage of the TESLA FEL bunch compression system.

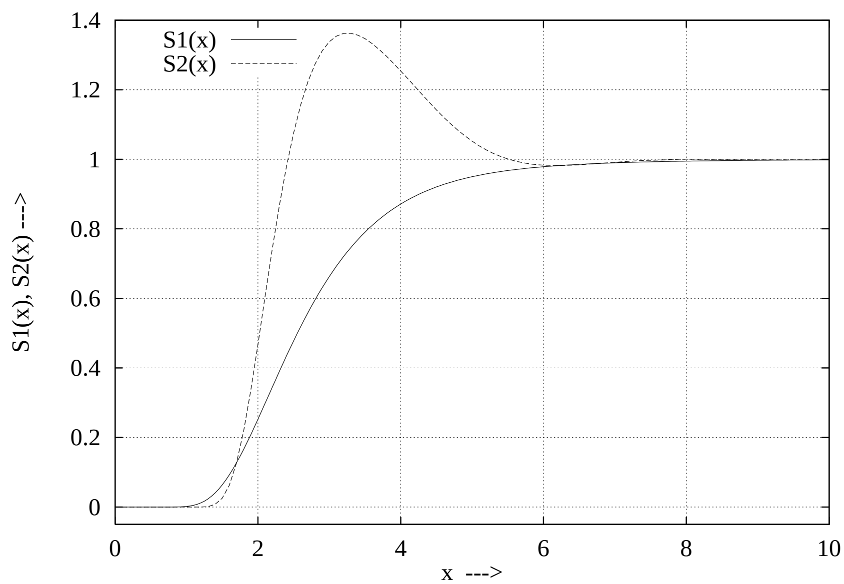

Figure 1: Shielding functions $S_1\left(x = h/\sqrt[3]{R_0\sigma^2}\right)$ and $S_2\left(x = h\sqrt[3]{\omega^2/(c_0^2 R_0)}\right)$.

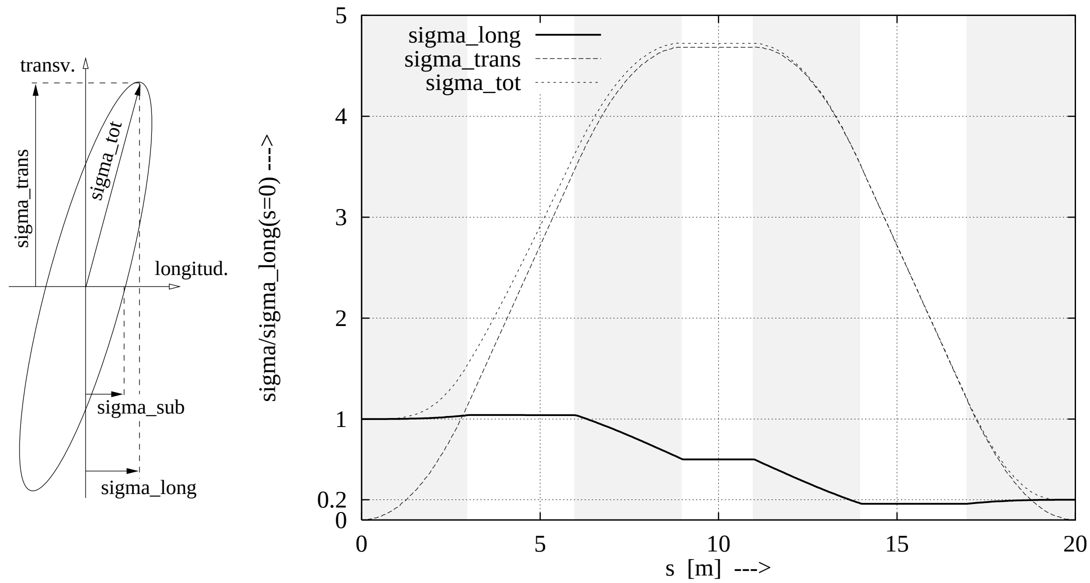

Figure 2: Bunch dimensions in TESLA bunch compressor III. The ranges in the magnets are shaded.

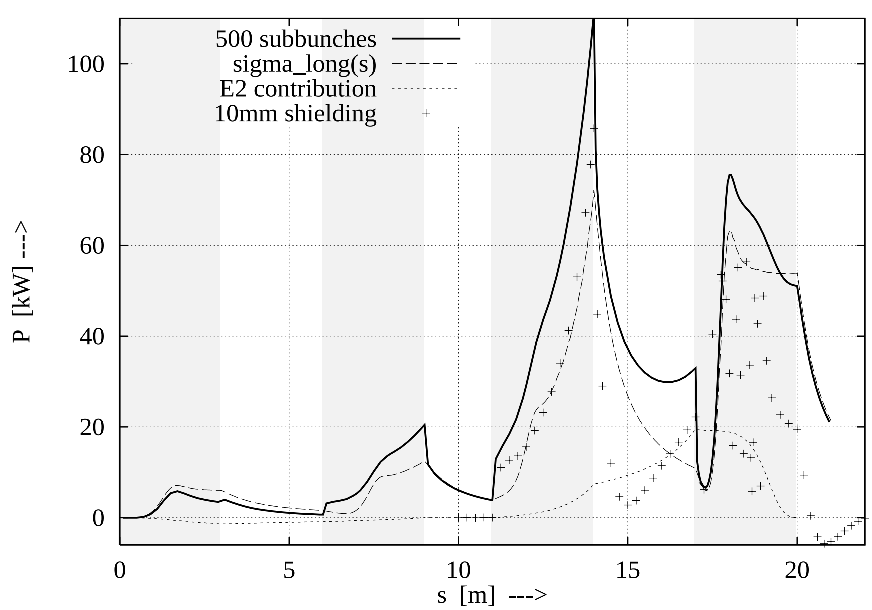

Figure 3: Power flow to the electromagetic field energy vs. bunch position. The shielding is calculated for s =10..20m. The ranges in the magnets are shaded.

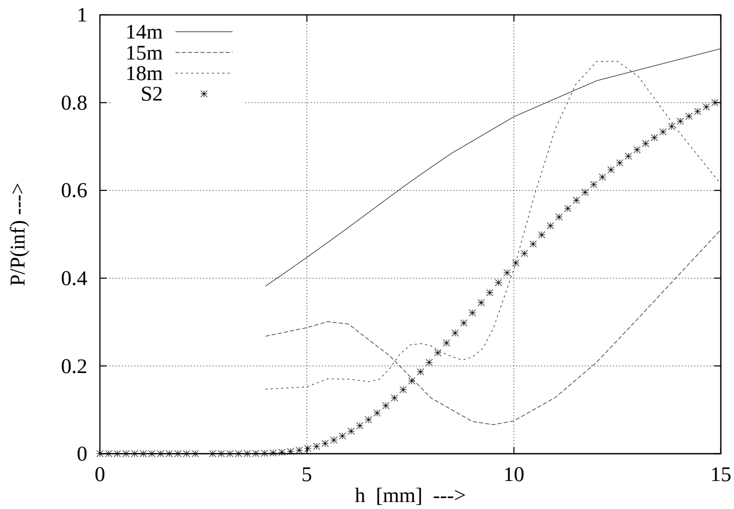

Figure 4: Shielding factor $P(h)/P(\infty)$ at different positions in the compressor and shielding function $S1$ with parameters at the end of BC3.

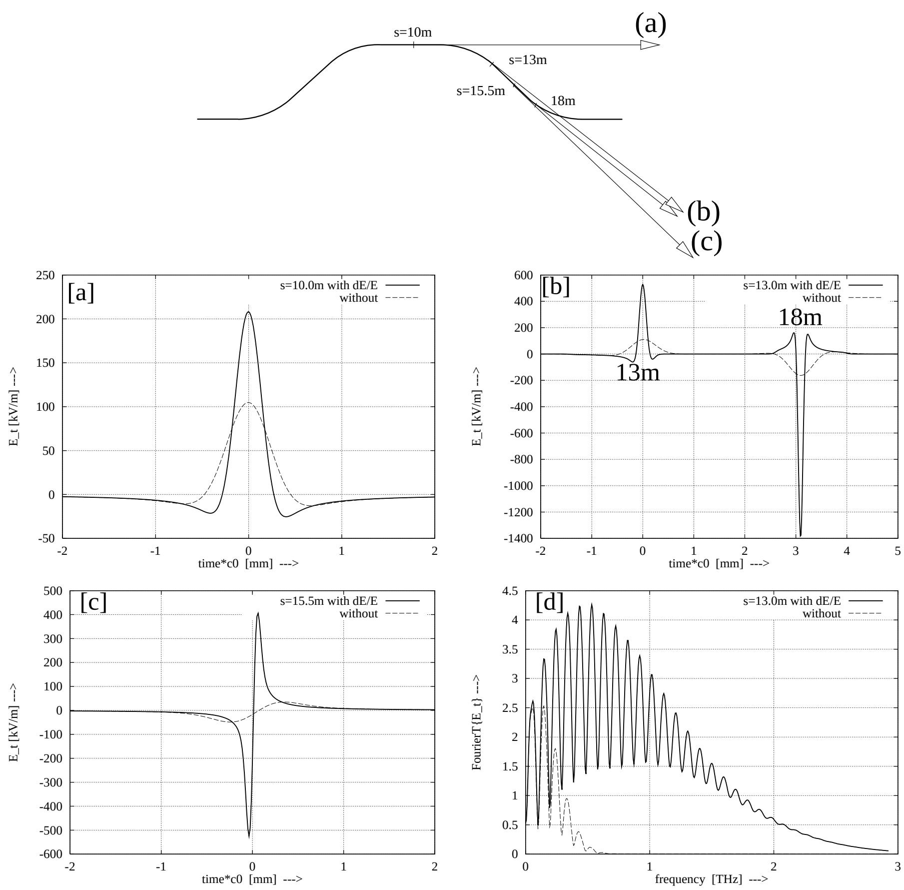

Figure 5: Transverse E-field in the far field region radiated at different locations along the bunch compressor with and without compression (energy spread $\delta E/E$). Oberservation after 15m in tangential direction: (a) $s_0 = 10$m, (b) $s_0 = 13$m and a second pulse radiated at 18m, (c) $s_0 = 15.5$m. (d) Fourier spectra of time signals (b).

Design Consequences of Coherent Synchrotron Radiation Beam Dynamic Effects on the TTF-FEL Bunch Compression System

M. Dohlus, A. Kabel, T. Limberg

Deutsches Elektronen-Synchrotron Notkestr. 85, 22607 Hamburg, Germany

Abstract

The emittance of a coherently radiating electron bunch is increased by self-induced longitudinal and radial wake fields with strong variations along the longitudinal axis[1, 2, 4]. We have written a numerical code which calculates fields and resulting emittance growth in transverse and longitudinal phase space. In this paper, we describe parameter optimization for the Tesla Test Facility FEL[3] bunch compression system to minimize emittance growth. The induced longitudinal wake potential in the center of a gaussian line charge of length σ_s on a circular trajectory with radius R scales with

$$W_| \propto \frac{1}{\sigma_s^{4/3} R^{2/3}}$$

and the 'critical height' of the vacuum chamber where shielding sets in is given by

$$h_c = 4\sqrt{3}(\sigma_s \sqrt{R})^{2/3},$$

so larger bending radii will alleviate emittance growth but will considerably lengthen the compression sections. Thus, numerical calculations taking into account the three-dimensional bunch shape, transition regions going into bending magnets and shielding effects are needed.

1 Introduction

The TTF-FEL requires a single bunch peak current of 2500 Amperes for the SASE process. This is achieved by compressing the bunches longitudinally to 50μm length. This compression is done in 'bunch compressors': magnet chicanes where particles of different energy have different path lengths so that the bunch length can be adjusted by inducing a longitudinal energy gradient.

The bunch compression in the TTF-FEL is done in stages. A first rather small bunch compressor (BC1) ensures that the bunch length is at the required 0.8 mm at the 20 MeV point. At an energy of ca. 150 MeV, the bunch is compressed from 0.8 mm to 0.25 mm in bunch compressor 2. Both these bunch compressors are already frozen where length and bending radii are concerned. The third bunch compressor at a beam energy of about 500 MeV where the final compression to 50μm takes place, has a length restriction of around 25 meters total but is still in the design phase.

The induced correlated energy spread is at least partly transformed into non-correlated energy spread by the compression process. Since the tolerable energy spread at the entrance of the TTF-FEL wiggler is only 0.1%, the path length difference per particle energy offset must be sufficient. That, given overall length limitations, makes the use of strong bending magnets with relatively small bending radii (of the order of meters) attractive.

The first effect to put a lower limit on bending radii R over a length L in a beam line is energy spread and emittance growth due to incoherent synchrotron radiation. The energy spread at a beam of energy of $E = \gamma m_e c^2$ is increased by:

$$\sigma_E \approx 1.94 \cdot 10^{-14}\mathrm{MeVm}\sqrt{\frac{\gamma^7 L}{R^3}}$$

while transverse emittance increases as:

$$\Delta(\varepsilon\gamma) \approx 4.04\ 10^{-8}\frac{\mathrm{m}^2}{\mathrm{GeV}^6}\ E^6 \frac{L}{R^3}\ H \tag{1}$$

with

$$H = \frac{1}{L}\int_0^L \frac{1}{\beta(s)}\left(D(s)^2 + (\beta(s)D(s)' + \alpha(s)D(s))^2\right) ds \tag{2}$$

and β the beam envelope function, α its derivative and D the dispersion function. These effects would limit the bending radii for bunch compressor 3 to one meter (to keep transverse emittance growth below 1%). That would fit a symmetric chicane for a required longitudinal compression factor $R_{56} = 0.15$ within three meters.

However, if short bunches travel along trajectories with small bending radii a simple geometrical condition permits strong longitudinal and radial wake fields to act on the bunch: electro magnetic fields emitted by a particle can 'overtake' on a shorter straight trajectory and interact with particles which are ahead in the bunch. The bunch then starts to radiate coherently.

The longitudinal variation of the wake fields causes a correlated bunch deformation in longitudinal-transversal phase space. We will call that in this paper 'correlated emittance' growth. For moderate growth (¡25%), this leads to an increase of the size of the photon cone. Since the cooperation length is short compared with the bunch length, the laser power is to first order not effected. For larger deformation, the coherent betatron oscillations in the undulato of the bunch regions with big transverse offsets disturb the overlap of radiated field and particle trajectory which is necessary for the SASE process. So parts of the bunch will not lase, overall power will drop. The transverse variation of the wake acts on the bunch like any non-linear field and causes non-correlated emittance growth inside the bunch slices. This emittance growth directly influences the SASE process.

2 Coherent Synchrotron Radiation in the Compression System of the TTF-FEL

2.1 Bunch compressor 2

Bunch compressor 2 had to be fit into a five meter long space while providing a longitudinal compression factor regime of $0.12 < R_{56} < 0.24$ [6]. Calculation on the effect of coherent synchrotron radiation wake fields were done at a setting of $R_{56} = 0.14$ and a corresponding bending radius of 1.6 meters[4]. It was shown that in order to keep correlated emittance growth small, the coherent radiation has to be shielded with a narrow gap vacuum chamber of 8 mm height. Without any shielding, the correlated emittance reaches more than five times the incoming transverse emittance of 1mm-mrad normalized. The observed increase in transverse emittance due to radial variations of the fields was found less than a few percent.

Besides introducing an aperture inconvenient for machine operation, the narrow gap vacuum chamber also excites wake fields due to the necessary steps to lower the chamber profile from the L-Band iris diameter into the chamber and to open it up again. For the BC2 we have calculated these fields with a simple model of stepping in and out of an iris and find the induced correlated energy spread is comparable or less than the nonlinearity of the RF (and of opposite sign) and is not going to disturb the bunching process[7].

2.2 Bunch compressor 3

2.2.1 Shielding and Longitudinal Compression

The longitudinal compression factor (R_{56}) of a symmetric chicane is given by

$$R_{56} = 2 \cdot (\frac{L}{R})^2 \cdot (\Delta L + \frac{2}{3} \cdot L)$$

where L is the bending magnet length, R the bending radius and ΔL the drift length in between bending magnets. To shield coherent synchrotron radiation effectively for a bunch of length σ_s, the vacuum chamber hight must be less than

$$h_c = 4\sqrt{3}(\sigma_s \sqrt{R})^{2/3},$$

where the fields are reduced by a factor between two and four [5]. To keep h_c at a reasonable size so that no severe aperture limitation is introduced to the beam line sets a lower limit for the bending radius R. The total length of a symmetric chicane scales then quadratically with the necessary h_c for a fixed R_{56}:

$$L_{Total} = (\frac{3}{10} R_{56})^{1/3} \cdot \frac{h_c^2}{(3.7 \cdot \sigma_s)^{4/3}}$$

For bunch compressor 3, total chicane length and bending radius are plotted in Fig.1 vs. h_c for a longitudinal compression factor $R_{56} = 0.15$, the uppermost to be required from the compression system design. For that case, a total length of 20 m is needed.

2.2.2 Emittance growth calculations

In the following calculations, bunch compressor 3 is a symmetric chicane with 3 m long bending magnets with deflection angles of 5.9 degrees (corresponding to a bending radius of 29.4 m) and 3 m long straight sections between the bending magnets. A linear correlated energy spread of $1.9 \cdot 10^{-3}$ compresses an incoming bunch with $\sigma_s = 250\mu$m length to $\sigma_s = 50\mu$m.

For the calculation of correlated emittance growth, the bunch is represented by 51 sub-bunches, each being a two-dimensional Gaussian charge distribution (horizontal and longitudinal). At the compressor entrance, the sub-bunches are lined up longitudinally over a range of $\pm 3\sigma_s$, modeling an incoming straight bunch.

The sub-bunches are then tracked through the bunch compressor, simulating the compression process in the dispersive section. The generated wake-fields are calculated and applied to the sub-bunch trajectories. Tracking is still not self-consistent, i.e., the fields are not re-calculated using the perturbed trajectories and then re-applied and so forth.

Fig.4 shows this distribution in phase space weighted with the relative bunch charge. In the core region, horizontal position and angle are strongly correlated. This optical mismatch has to be compensated for by the subsequent beam line optics. At the compressor end, the RMS-sizes of the distribution of the sub-bunch centers are $\sigma_{x,correlated} = 190\mu$m and $\sigma_{x',correlated} = 37\mu$rad which compare with the sub-bunch sizes of $\sigma_x = 113\mu$m and $\sigma_{x'} = 13\mu$rad at a β-function of 10 meters.

The situation is altered significantly as soon as shielding is introduced. The simulations described above were also done with a vacuum chamber, consisting of a pair of conductive plates 8mm apart, parallel to each other and to the plane of motion.

Figures 3 and 4 correspond to 2 and 5, respectively. The induced energy spread has decreased by a factor of two.

Figure 6 compares the beams' phase-space distributions at the end of the compressor section. The area of the included phase-space has decreased drastically. For the RMS values, we find $\sigma^{shielded}_{x,correlated} = 50\mu$m and $\sigma^{shielded}_{x',correlated} = 37\mu$rad. The phase-space distibution still is highly correlated in the area of high statistical weight.

2.2.3 Vacuum chamber heat load

For the above case of a bunch compressor 3 with a total length of 20 meters, bending radii of ca. 30 meters and a R_{56} of 0.15 the radiated power vs. position is shown in Fig.7. The cw heat load is given by

$$P_{cw} = P_{bunch} \cdot t_{bunch} \cdot \frac{n_{bunch}}{sec}$$

where P_{bunch} is the power radiated by a single bunch and t_{bunch} the bunch length in time. If we take the bunch length to be $100\mu m$ and thus t_{bunch} to be ca. 0.4 ps (FWHM) and the number of bunches n_{bunch} per second as 70000 (ten cycles of 7000 bunches), the average power comes out to be only fractions of a Watt.

3 Conclusion

Correlated emittance growth due to coherent synchrotron radiation determines the choice of the bending radius of the compressor chicane magnets and thus the length of the system. The correlated emittance growth is accompanied by an optical mismatch which has to be compensated by the subsequent beam line optics. The heat load of the vacuum chamber due to coherent synchrotron radiation should be negligible if parameters have been chosen which avoid strong correlated emittance blow up.

References

[1] Y.Derbenev, J.Rossbach, E.Saldin, V.Shiltsev: 'Microbunch Radiative Tail-Head Interaction', TESLA-FEL 95-05, September 95.

[2] Y.Derbenev, V.Shiltsev: 'Transverse Effects of Microbunch Radiative Interaction', Fermilab-TM-1974, May 1996.

[3] A VUV Free Electron Laser at the TESLA Test Facility at DESY. Conceptual Design Report. DESY Print June 1995, TESLA-FEL 95-03

[4] M.Dohlus, T.Limberg: 'Emittance Growth due to Wake Fields on Curved Bunch Trajectories', To be published in the proceedings of the FEL'96 in Rome.

[5] M.Dohlus, T.Limberg: 'Calculation of Coherent Synchrotron Radiation Power Spectrum in the TTF-FEL Bunch Compressor Magnet Chicanes', Contribution to this conference.

[6] T.Limberg, A.Molodozhentsev,V.Petrov,H.Weise: 'The bunch compression system at the TESLA test facility FEL', NIM in Physics Research A 375 (1996) 322-324

[7] H. Schlarb, priv. com.

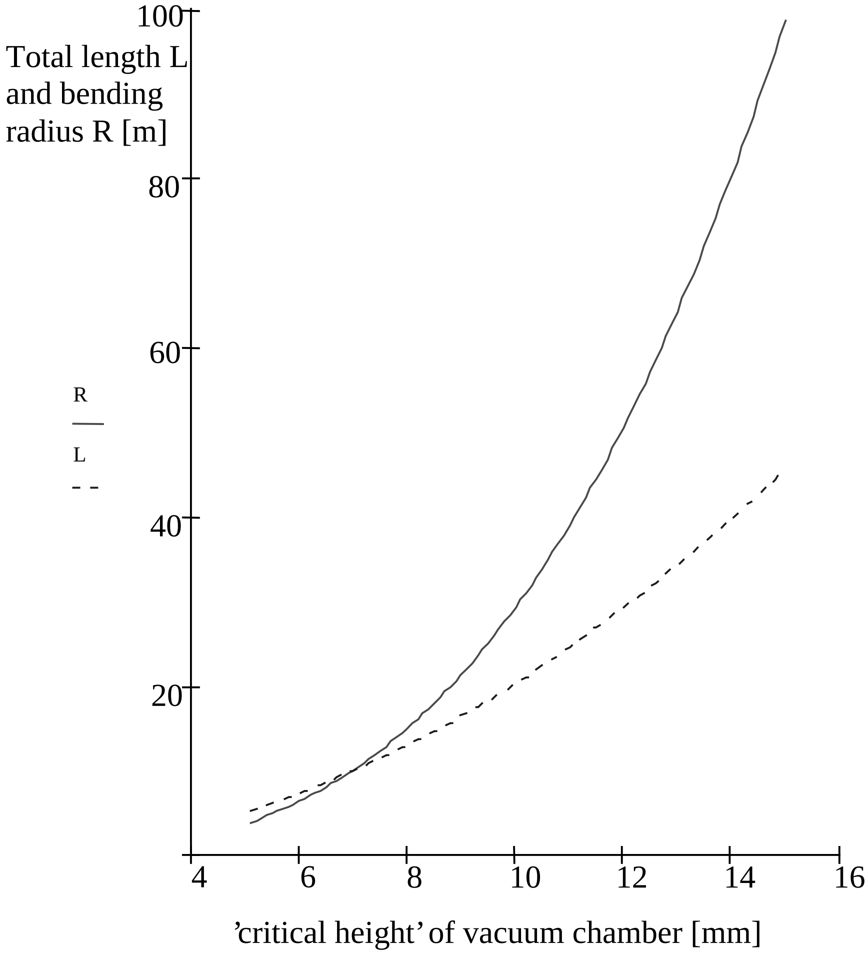

Figure 1: Bending radius and total length of magnet chicane vs. critical height of vacuum chamber for the case of TTF-FEL bunch compressor 3 (final bunch length $\sigma_s = 50\mu$m, longitudinal compression factor $R_{56} = 0.15$)

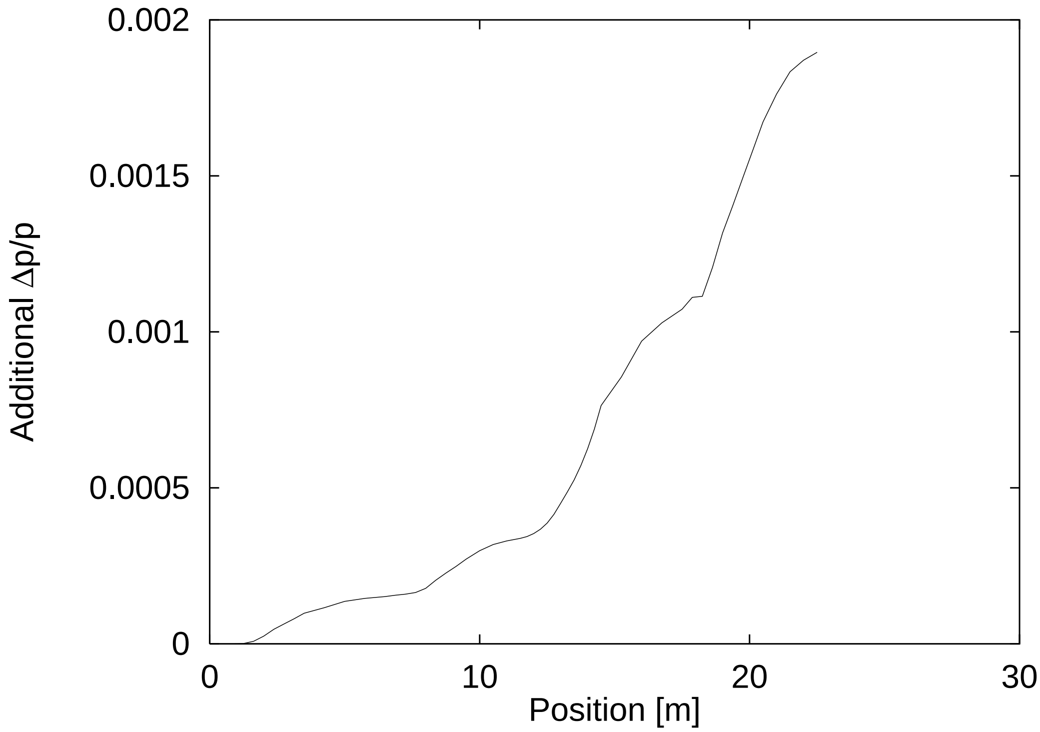

Figure 2: Energy spread gained by a bunch transversing the bunch compressor 3

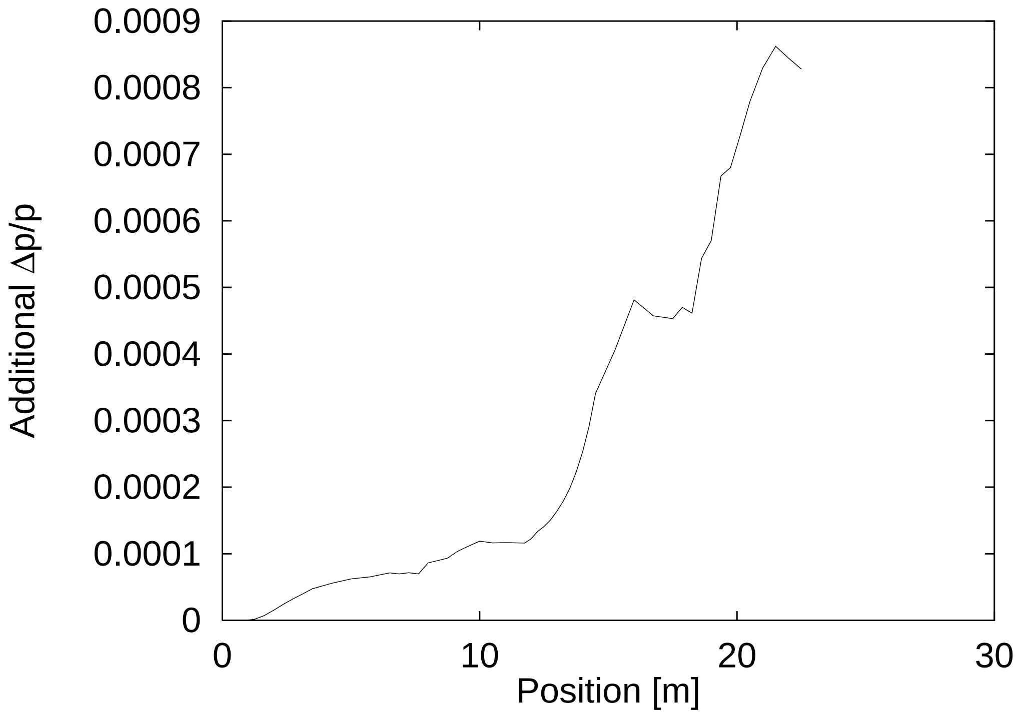

Figure 3: Energy spread gained by a bunch transversing the shielded bunch compressor 3

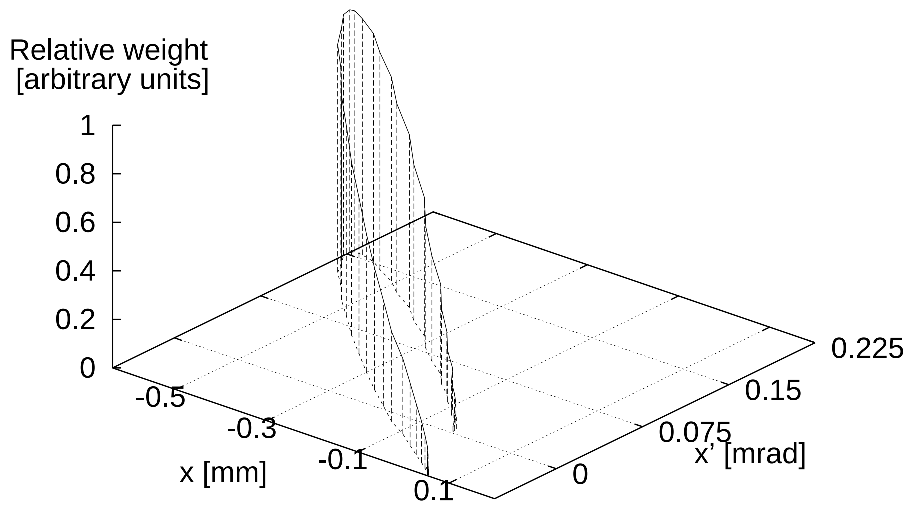

Figure 4: Phase space distribution of sub-bunch centers weighted with charge density of the bunch at the end of bunch compressor 3

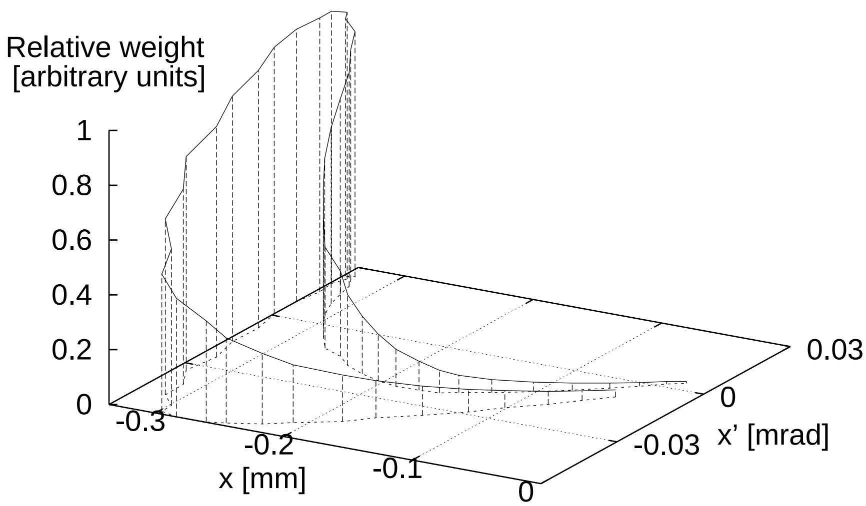

Figure 5: Phase space distribution of sub-bunch centers weighted with charge density of the bunch at the end of bunch compressor 3 for the shielded case

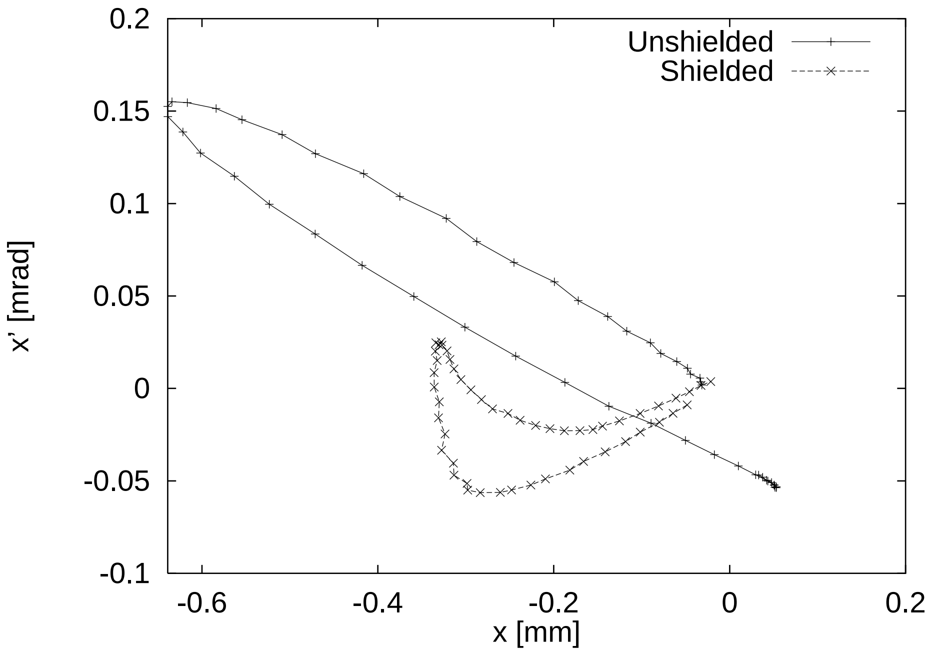

Figure 6: Comparison of phase space distribution at the end of bunch compressor 3 with and without shielding

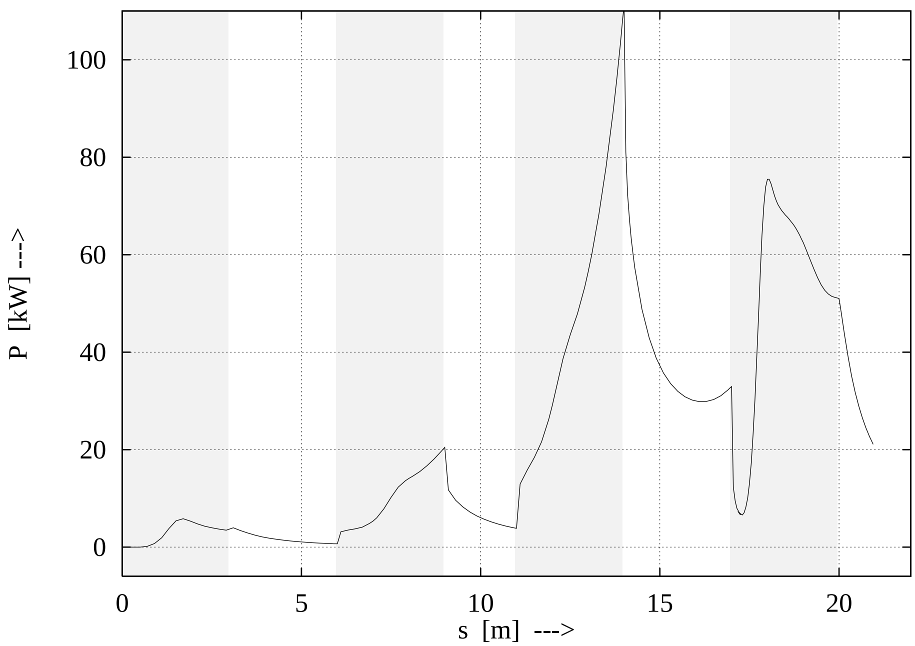

Figure 7: Total power radiated by the bunch during compression in bunch compressor 3 vs. longitudinal position

Beam Based Alignment Procedure for an Undulator with Superimposed FODO Lattice

P. Castro, B. Faatz, K. Flöttmann

Deutsches Elektronen Synchrotron DESY
Notkestraße 85, 22603 Hamburg, Germany

Abstract

Since the FEL process is based on the interaction of an electron beam with the photon beam, an excellent spatial overlap of the two beams is mandatory. The aim of beam based alignment techniques is to determine the relative offset of beam position monitors with respect to the magnetic axis of quadrupole magnets by means of beam observations. A local and a global procedure to correct the effect of misalignments and field errors on the beam orbit will be presented and compared.

1 Introduction

At Deutsches Elektronen-Synchrotron (DESY) a large effort is dedicated to build a Free Electron Laser (FEL) starting up from noise, i.e. in the so-called Self-Amplified Spontaneous Emission (SASE) mode [1]. The superconducting TTF accelerator will in its final stage deliver an electron beam with an energy of 1 GeV. In the first stage, however, only a part of the accelerator will be built for a proof-of-principle experiment at 300 MeV to 390 MeV. For this stage a 15 m long undulator is under construction. Table 1 summarizes relevant parameters for the undulator and the beam optics. For the final stage at 1 GeV the undulator will be extended to about 30 m.

The FEL process requires a high density of the electron beam, which is achieved by focusing the beam size to about 50 μm inside the undulator. This requires quadrupoles with a spacing of 0.5 m realized with permanent magnets integrated into the undulator structure [2]. Besides a strong focusing, a good overlap of the electron beam trajectory with the photon beam is required for the FEL process. A reduction of the overlap may be caused by magnetic errors of the undulator field and by alignment errors (offsets) of the quadrupole magnets. Simulation studies [3] indicate that the rms deviation of the electron beam from a straight line has to be below 10 μm at least over the length of one undulator module (4.5 m). For the correction of the electron orbit Beam Position Monitors (BPMs) and corrector magnets will be integrated into the undulator vacuum chamber. Due to the geometrical constrains inside the undulator gap, it is impossible to optimize the position of the BPM and the corrector independently.

While the resolution of the BPMs might allow relative measurements of 1 μm accuracy, the absolute alignment of the BPMs is expected to be of the order of 100 μm. In this paper we discuss methods to achieve the required alignment of the electron beam by means of beam based alignment techniques. The aim is to determine the relative offset between BPMs and the magnetic axis of quadrupole magnets from beam observations. While the offset information

TESLA FEL-Report 1997-06

Table 1: Undulator and optics parameters for the TTF FEL at 300 MeV (Phase I).

Undulator	
number of modules	3 (6)
length of module	4.5 m
period length	27.3 mm
undulator peak field	0.497 T
peak field error ΔB/B	$\leq 4 \times 10^{-3}$
Quadrupole	
number per module	10
length	136.5 mm
separation	341 mm
offset error	$\leq 50\,\mu$m
integrated strength	2.5 T
focal length	0.4 m
Optics	
$\beta_{\max}$	1.5 m
$\beta_{\min}$	0.5 m
phase advance per FODO cell	65°
betatron wavelength	$\approx$6.3 m

could be used to improve the mechanical alignment of the components it is in general sufficient to correct orbit errors with the corrector magnets, i.e. the offset information is the basis for improved trajectory corrections. Therefore, beam based alignment procedures mediate between classical accelerator alignment and orbit correction techniques.

In the following, two procedures will be discussed and compared: a local [4] and a global correction technique [5]. In the first approach one corrector after the other is optimized and the beam is forced onto a straight line defined by the position and angle of the incoming beam before the undulator. In case of the global correction the effect of each corrector onto the downstream beam orbit is taken into account and the beam is forced onto the line defined by the average position of the quadrupoles.

2 Local Correction

Figure 1 shows schematically the correction method in the first half FODO cell of the undulator. The position of the beam at the BPM located in the center of the next quadrupole is given in thin lens approximation by

$$x_1 = x_0 + x_0' \cdot s + \frac{K_q}{p} \cdot s_q + \sum_i \frac{D_i}{p} \cdot s_i + \frac{C}{p} \cdot s_c$$

where x_0 and x_0' are the beam initial conditions at the entrance of the quadrupole. Here K_q is the kick generated by the quadrupole, D_i are the dipole kicks and C is the kick of the corrector. p denotes the momentum of the beam and s, s_q, s_i and s_c indicate the distance from each element to the BPM. In order to have the beam onto a straight line, $x_1 = x_0 + x_0' \cdot s$ and the sum of all kicks has to be zero. Obviously, this is the case when the measured beam position at the next

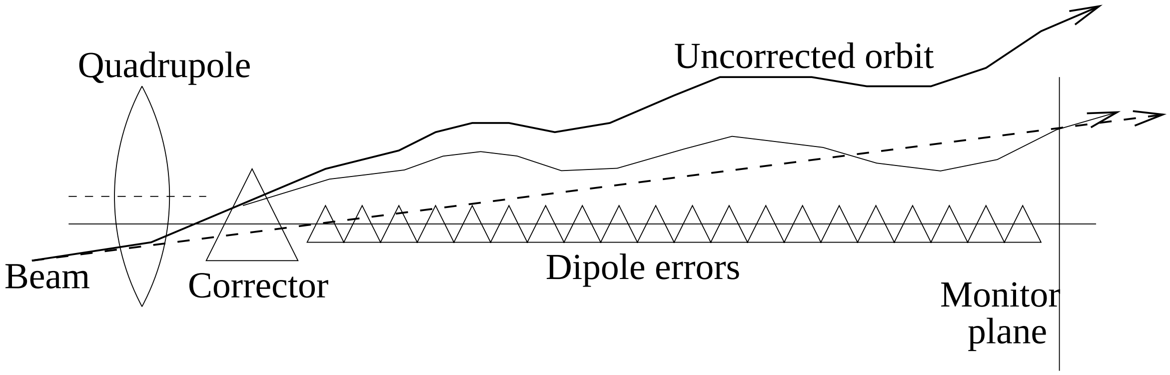

Figure 1: Schematic overview of the local beam based alignment. At the BPM positions the beam continues in the direction of the incident beam.

BPM is independent of the beam energy. Thus the beam can easily be forced onto a straight line at the positions of the BPMs. (It will, of course, deviate from a straight line in between the BPMs.) Note that while the position at the BPMs is independent of energy the angle will slightly change when the energy is changed. This in conjunction with the thick lens behavior of the quadrupoles will lead to a slow drift from a straight line. A simple way to determine the required excitation of the corrector coil is to measure the beam position at the next BPM as function of the excitation for two different energies (typically with 10% energy variation). The intersection of both measured lines indicates the required corrector setting. The lines can be determined with very high accuracy even if the BPM resolution is not very good by taking more measurement points. Since the beam is forced to follow the incoming beam vector its trajectory can in principle be far off axis at the end of the undulator. In this case, the corrector settings will show a linear growing amplitude in order to compensate the quadrupole orbit kicks. Therefore, a beam trajectory far off axis can be detected and corrected in a second step. Thus, it is also possible to correct displacements of individual undulator modules.

3 Global dispersion correction using Micado algorithm

Micado [6] is an algorithm used to correct the orbit in storage rings. This algorithm searches for a set of corrector strengths which minimizes the beam position at the BPMs. Here, Micado is applied at the undulator of the TTF-FEL in order to solve the system of linear equations

$$d_i + \sum_{j=1}^{N_{\rm corr}} a_{ij} c_j = 0 \qquad \text{for} \;\; i = 1, ..., N_{\rm mon} \tag{1}$$

with $N_{\rm mon}$ the number of BPMs and $N_{\rm corr}$ the number of correctors. The vector c_j represents the corrector strengths to be calculated and the vector d_i is given by the measured dispersion at the BPMs. The *correction matrix* a_{ij} is calculated as

$$a_{ij} = \left. \frac{x_i(E-\Delta E) - x_i(E)}{\Delta E / E} \right|_{c_j\,=\,1} \qquad \text{for} \;\; i = 1, ..., N_{\rm mon} \;\; \text{and} \;\; j = 1, ..., N_{\rm corr}$$

where x_i is the beam displacement due to the corrector strength c_j and ΔE is energy change used for dispersion measurements. A ΔE about 20% is needed in order to obtain precise dispersion measurements. For BPMs with less resolution, ΔE needs to be larger.

In linear transfer lines, the correction matrix is triangular, i.e., $a_{ij} = 0$ for $j \geq i$. In the case of the TTF-FEL with $N_{\text{mon}} = N_{\text{corr}} = 30$, the dispersion correction is local because the solution of the system of equations is:

$$c_1 = \frac{-d_2}{a_{21}} \ , \qquad c_2 = \frac{-d_3 - a_{31}c_1}{a_{32}} \ , \qquad \dots \ , \qquad c_i = \frac{1}{a_{i+1,i}} \left(-d_{i+1} - \sum_{j=1}^{i-1} a_{i+1,j} \ c_j \right)$$

In the case that $N_{\text{mon}} = N_{\text{corr}}$, each corrector i cancels the dispersion measured at BPM $i+1$ and corrects the dispersion created by upstream correctors at this BPM. Thus, the dispersion is vanishing at the BPMs. However, the orbit is not corrected because the dispersion correction introduces dispersion bumps between BPMs which lead to orbit distortions.

The dispersion can be corrected better in the whole beam line by limiting the number of correctors used in each iteration with Micado to four or five. Then, the dispersion correction is global, since Micado tries to minimize the dispersion measured at 30 BPMs with a maximum of five correctors. After 15 or 20 iterations with Micado, the beam is well aligned. Since the effect of each corrector in all monitors has to be small, the corrector strengths are minimized and the beam is forced onto the line defined by the average position of the quadrupoles.

The beam alignment obtained in the simulations is further improved using only the correctors at the focusing quadrupoles, i.e., with $N_{\text{corr}} = 16$. In this case, the correction is also global, since $N_{\text{mon}} > N_{\text{corr}}$ and needs only one iteration with Micado.

With 16 correctors, the number of BPMs can be reduced by half. However, with one BPM per focusing quadrupole the number of BPMs and the number of correctors are equal and the correction is again local. Using two more BPMs at the end of the undulator avoids this situation and forces a global correction. The configuration of 16 correctors and 17 BPMs is shown in fig. 2.

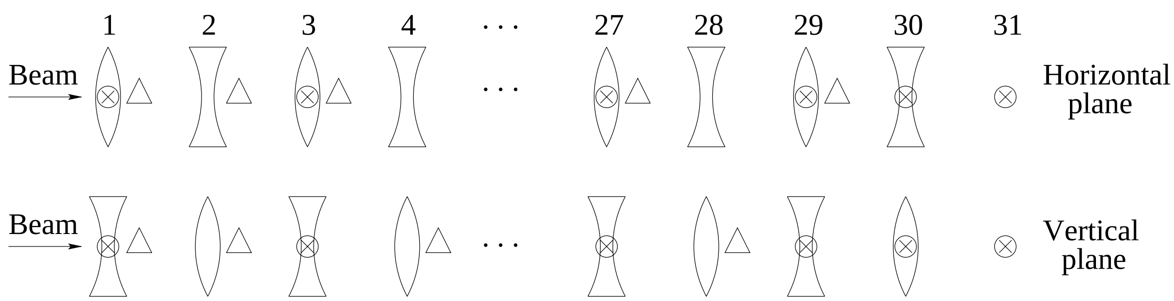

Figure 2: Undulator configuration with 16 correctors (triangles) and 17 BPMs (crossed circles).

The rms beam orbit obtained in simulations with $N_{\text{mon}} = 17$ is in average similar as with $N_{\text{mon}} = 30$. However, the beam position measurement can not be decoupled and one has to choose whether the BPMs are installed at the horizontal or at the vertical focusing quadrupoles. If the BPMs are placed at horizontal focusing quadrupoles, the resulting vertical orbit rms is about 10% larger than with 30 BPMs (at 300 MeV).

4 Simulation results

The upper limit of quadrupole alignment assumed in this paper is $\pm 50\,\mu$m. The undulator dipole field error has been distributed randomly with a $\Delta B/B$ rms of 0.4%, with the first and the second field integrals, proportional to the beam deviation from a straight line, corrected to zero every 10 undulator periods. In this correction, the influence of the quadrupoles has not been taken into account. Therefore, one can assume that the quadrupole offsets are the main source of errors. A monitor resolution of 1 μm rms is included in the simulations. The simulations are carried out at the beam energy of 300 MeV. With higher beam energies, the beam alignment is expected to be better since the effect on the orbit of quadrupole misalignment and undulator field errors is smaller.

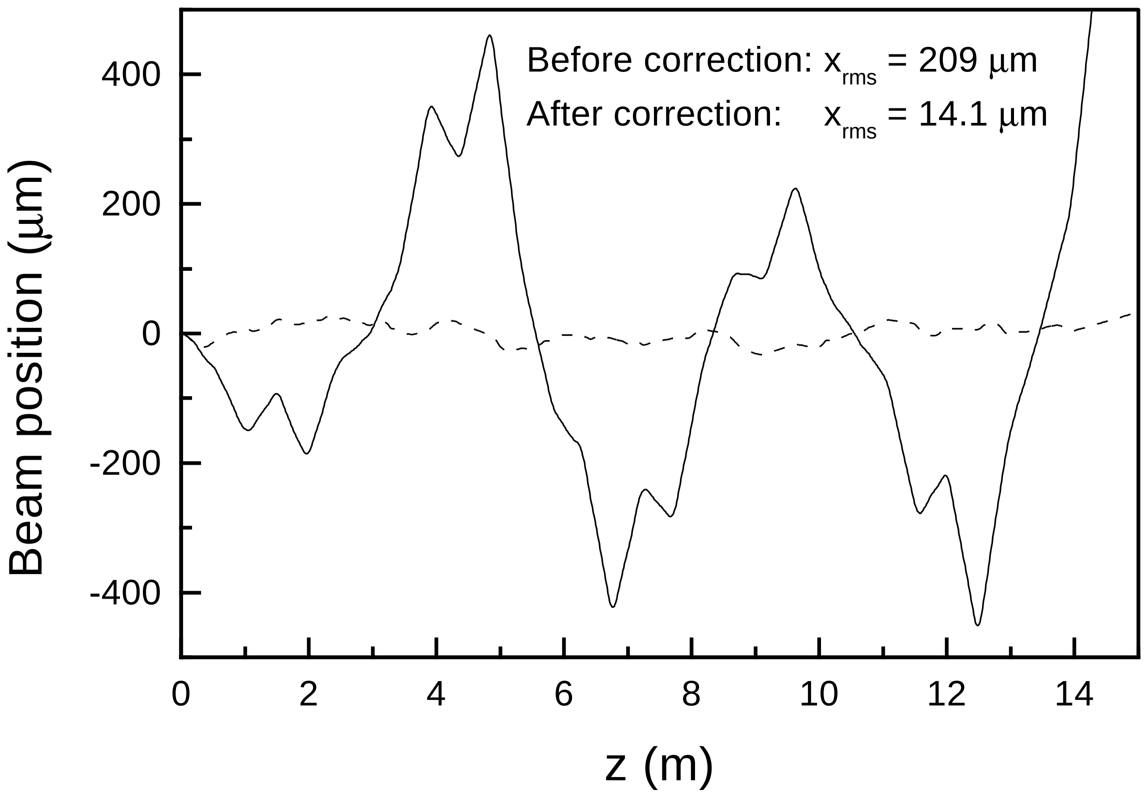

Figure 3: Example of a beam trajectory before (solid line) and after global correction (dashed line). A similar result is obtained with the local correction method (16.6 μm).

The simulation programs for the local and the global correction were developed independently by the authors. An example of orbit correction with the global method is shown in fig. 3. Both programs give identical results for the uncorrected orbit using the same input of random errors. Using the global method the rms orbit after correction is about 14 μm. A similar result is obtained with the local method with a rms orbit of 17 μm.

The results of simulations of both methods using 50 sets of random errors are shown in fig. 4.

As can be seen, the results with the local method exceed the required beam alignment by a factor two, whereas the global method meets the desired beam alignment. Both programs used give approximately the same results when 30 correctors and BPMs are used. The additional constrains in the global procedure result in a better alignment. In case of the local method, additional correction procedures can use correlations between the calculated corrector settings to reduce the overall misalignment. This would result in a narrowed distribution and a reduction of the average rms. This procedure has also been successfully employed to find initial beam offsets and angles as well as displacement or rotation of individual undulator modules.

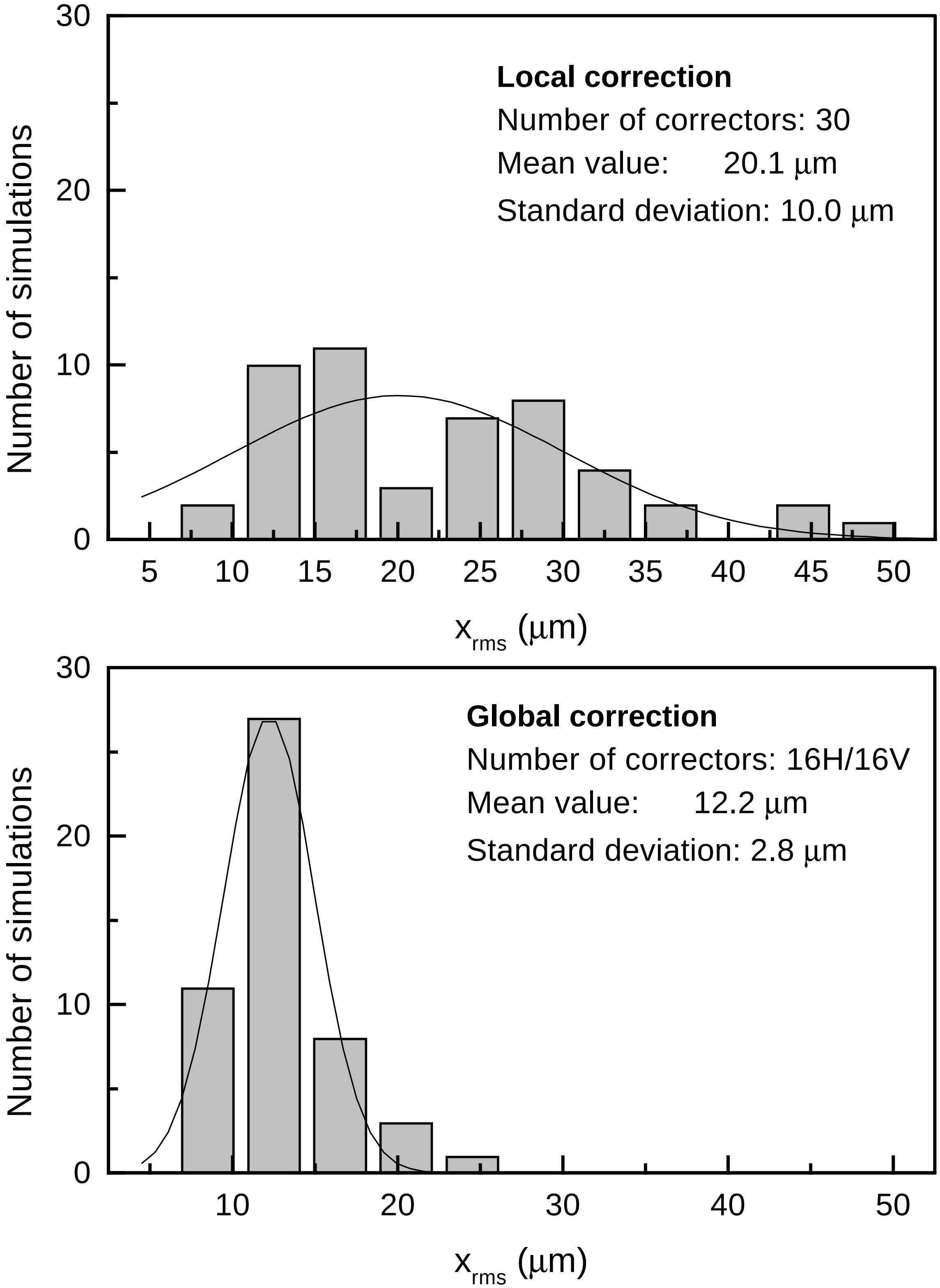

Figure 4: Histogram of rms beam orbits for 50 random seeds with the local correction method (top) and the global correction method (bottom).

5 Conclusions

Based on simulation results, beam based alignment procedures can provide the required beam alignment needed at the TTF FEL undulator. The local correction procedure is limited by the fact that the weak and rather long correctors do not overlap with the quadrupoles. This leads to energy dependent angles in the quadrupoles, which act as thick lenses, and a deviation of the trajectory from the ideal straight line. With correctors overlapping the quadrupoles it would be possible to correct the orbit well below 10 μm even with a poor BPM resolution. The local procedure requires one corrector and one BPM per quadrupole. The global correction procedure allows, however, to reduce the number of correctors and BPMs inside the undulator by a factor of ~ 2. It meets the FEL specifications and is compatible with all hardware constrains that arise due to the integration of the BPMs and correctors into the undulator gap.

References

[1] "*A VUV Free Electron Laser at the TESLA Test Facility: Conceptual Design Report*", DESY TESLA-FEL 95-03, Hamburg, 1995.

[2] J. Pflüger, Y. Nikitina, 'Undulator Schemes with the Focusing Properties for the VUV-FEL at the TESLA Test Facility' DESY TESLA-FEL 96-02, Hamburg 1996.

[3] B. Faatz, J. Pflüger and Yu.M. Nikitina, *Study of the undulator specification for the VUV-FEL at the TESLA Test Facility*, presented at the 18th FEL conference, Rome, Italy, 1996. B. Faatz, J. Pflüger and Yu.M. Nikitina, *Geometrical Undulator Tolerances for the VUV-FEL at the TESLA Test Facility*, presented at the 18th FEL conference, Rome, Italy, 1996.

[4] K. Flöttmann, B. Faatz, E. Czuchry and J. Roßbach, *Beam Based Alignment Procedure for an Undulator with Superimposed FODO Lattice*, DESY TESLA-FEL 97-05, Hamburg, 1997.

[5] P. Castro, *TTF FEL Beam Based Alignment by Dispersion Correction using Micado algorithm*, DESY TESLA-FEL 97-04, Hamburg, 1997.

[6] B. Autin and Y. Marti; *Closed Orbit Correction of A.G. Machines using a Small Number of Magnets*; CERN/ISR-MA/73-17, March 1973.

Parameter Optimization of X-ray Free Electron Lasers at a Linear Collider

B. Faatz[a], J. Pflüger[a], J. Rossbach[a],
E.L. Saldin[b], E.A. Schneidmiller[b], M.V. Yurkov[c]

[a] *DESY, 22607 Hamburg, Germany*

[b] *Automatic Systems Corporation, 443050 Samara, Russia*

[c] *Joint Institute for Nuclear Research, Dubna, 141980 Moscow Region, Russia*

Abstract

Within the TESLA Linear Collider concept X-ray FELs together with different kinds of conventional undulators and wigglers will serve as radiation sources for an X-ray user facility which is considered as integrated part of the laboratory. Parameters of these radiation sources exceed significantly those available at present.

1. Introduction

Nowadays there exist two proposals for an X-ray FEL operating in an Å wavelength region [1, 2]. The project of a 6 nm Self Amplified Spontaneous Emission (SASE) free electron laser (FEL) is now under construction at the TESLA Test Facility at DESY [3, 4]. This project is considered as a step towards an X-ray FEL which is planned to be integrated into the TESLA-500 linear collider project [2]. It is planned to organize simultaneous operation of the TESLA linear accelerator for high energy physics and for generation of powerful coherent radiation (see Fig. 1).

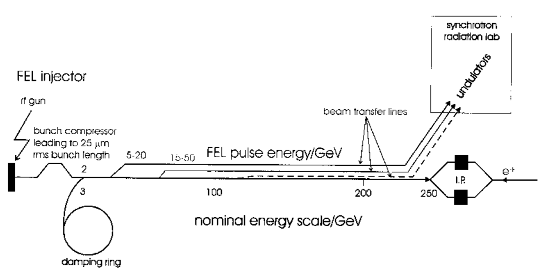

Fig. 1. Schematic layout of X-ray laboratory at TESLA.

Starting points for optimization of FEL parameters are the tunability of radiation from 15 Å down to a fraction of Angstrom, normalized emittance of 1π mm mrad, energy spread in the electron beam of 1 MeV, the value of the peak current of 5 kA and the available electron energy (in the range of 10 – 25 GeV and 25 – 50 GeV for the first and the second beamline, respectively). The main factors influencing the choice of the FEL parameters are diffraction effects, quantum fluctuations of undulator radiation and technical limitations on manufacturing of the undulator and the external focussing system.

2. Limitations of an X-ray FEL operation

The peculiarity of the region of parameters of an X-ray FEL at a Linear Collider is that the space charge fields do not influence significantly the FEL process and optimization of the FEL parameters can be performed by taking into account only diffraction effects and the longitudinal velocity spread in the electron beam (which occurs due to the emittance and energy spread in the beam). When the latter effect is negligible, the FEL operation is described with three param-

TESLA FEL-Report 1997-06

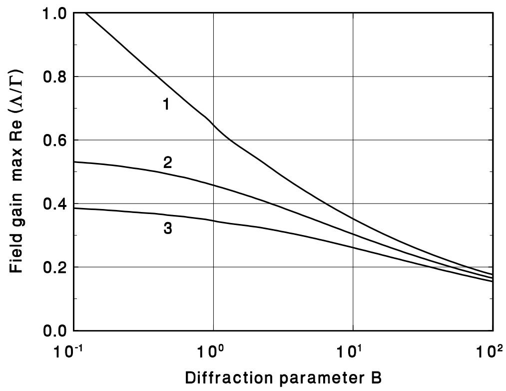

Fig. 2. The dependence of the maximum field gain on the diffraction parameter B. Curve (1) – TEM_{00} mode, curve (2) – TEM_{10} mode and curve (3) – TEM_{01} mode.

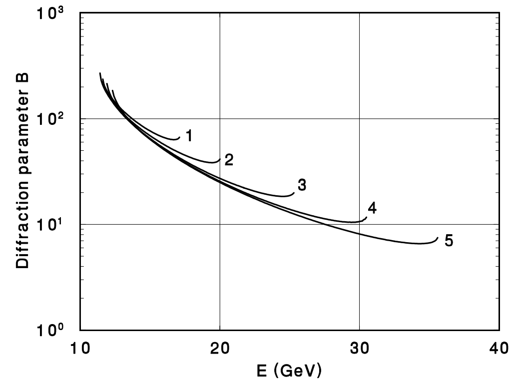

Fig. 3. Diffraction parameter B for a 1 Å FEL with planar undulator versus the energy of the electron beam. Curve (1) – $\lambda_{\mathrm{w}} = 3.5$ cm, curve (2) – $\lambda_{\mathrm{w}} = 4$ cm, curve (3) – $\lambda_{\mathrm{w}} = 5$ cm, curve (4) – $\lambda_{\mathrm{w}} = 6$ cm and curve (5) – $\lambda_{\mathrm{w}} = 7$ cm.

eters: the gain parameter Γ, the diffraction parameter B and the efficiency parameter ρ_{3D} [5]:

$$
\begin{aligned}
\Gamma &= \left[I\omega^2\theta_s^2/(I_{\mathrm{A}}c^2\gamma_z^2\gamma)\right]^{1/2} \quad , \\
B &= 2\Gamma\sigma_{\mathrm{r}}^2\omega/c \quad , \\
\rho_{\mathrm{3D}} &= c\gamma_{\mathrm{z}}^2\Gamma/\omega. \qquad (1)
\end{aligned}
$$

Here $\lambda = 2\pi c/\omega$ is the radiation wavelength, I is the beam current, $I_A = mc^3/e \simeq 17$ kA is Alfven's current and $\gamma_{\mathrm{z}}^2 = \gamma^2/(1+K^2)$. In this paper all formulae are written for the case of a helical undulator.

To provide full transverse coherence of the output radiation, it is necessary to provide mode selection. Figure 2 shows the relative dependence of the field gain for different radiation modes on the value of the diffraction parameter B. It is seen from this plot that obtaining full transverse coherence at high values of the diffraction parameter becomes problematic.

2.1. Limit 1

The effect of the longitudinal velocity spread (due to energy spread and emittance) imposes a limit on the minimal achievable wavelength in the FEL amplifier [6]. When designing X-ray free electron laser operating at the wavelength around 1 Å one should take into account that the energy spread in the electron beam is increased due to quantum fluctuations of the undulator radiation. This effect grows drastically with energy and imposes a principle limit on achieving very short wavelengths. Even in the case of zero initial energy spread the minimal achievable wavelength is about [6]:

$$
\lambda_{\min} \simeq 45\pi \left[\lambda\!\!\!^{-}_{\mathrm{c}} r_{\mathrm{e}} \right]^{1/5} L_{\mathrm{w}}^{-7/15} \left[\epsilon_n^2 \frac{I_A}{I} \right]^{8/15} , \quad (2)
$$

or, in practical units

$$
\lambda_{\min}[\AA] \simeq 4 \frac{\pi\epsilon_n[\mathrm{m}m\ mrad]}{\sqrt{I[\mathrm{k}A]L_w[\mathrm{m}]}} ,
$$

where $\lambda\!\!\!^{-}_{\mathrm{c}} = \hbar/mc$.

3. Parameters for an X-ray FEL laboratory at TESLA

The theoretical considerations formulated in the previous sections formed the basis for parameter studies for different X-ray FELs. A more detailed optimization of the output characteristics has been performed using numerical simulation codes FS2R and TDA3D [7, 8, 9]. During steady-state simulations the value of the effective power of shot noise has been chosen in accordance to [10, 11]:

$$
W_{\mathrm{sh}} \simeq \frac{3\sqrt{4\pi}\rho^2 P_{\mathrm{b}}}{N_\lambda\sqrt{\ln(N_\lambda/\rho)}} , \quad (3)
$$

where $\rho = \rho_{\mathrm{3D}}B^{-1/3}$ is the saturation parameter of the one-dimensional theory [12], $P_{\mathrm{b}} = \gamma m_{\mathrm{e}}c^2 I/e$ is the power of the electron beam and $N_\lambda = I\lambda/(ec)$.

While it is not a significant problem to optimize the parameters of SASE FEL operating at a wavelength of a few Angstrom, optimization becomes complicated for an 1 ÅFEL because of the strong influence of the quantum fluctuations of undulator radiation. For the electron beam of the TESLA FEL

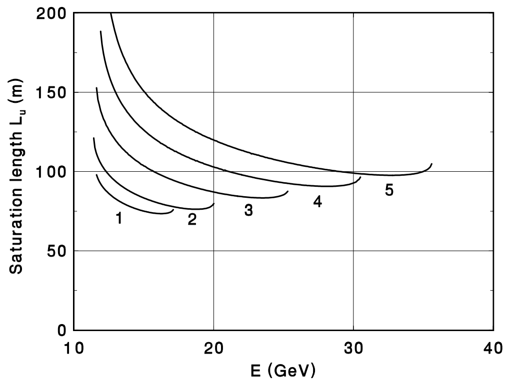

Fig. 4. Saturation length for a 1 Å FEL with planar undulator versus the energy of the electron beam. Curve (1) – λ_w = 3.5 cm, curve (2) – λ_w = 4 cm, curve (3) – λ_w = 5 cm, curve (4) – λ_w = 6 cm and curve (5) – λ_w = 7 cm.

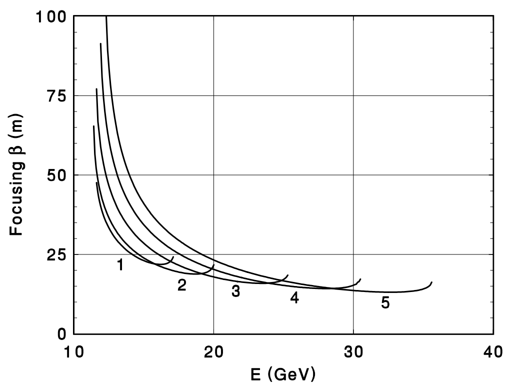

Fig. 5. External focussing beta function for a 1 Å FEL with planar undulator versus the energy of the electron beam. Curve (1) – λ_w = 3.5 cm, curve (2) – λ_w = 4 cm, curve (3) – λ_w = 5 cm, curve (4) – λ_w = 6 cm and curve (5) – λ_w = 7 cm.

(1πmm mrad rms normalized emittance, 1 MeV rms energy spread, 5 kA peak current) and at an undulator length $L_w \sim 50 - 100$ m the operation of the X-ray FEL at the wavelength near 1 Å becomes possible at an electron energy of about 12 GeV [6] and an undulator period larger than 3 cm. Figures 3, 4 and 5 illustrate the dependence of the diffraction parameter, the saturation length and the external focussing beta function as a function of energy for different undulator periods. Analysis of Figs. 2 and 3 shows that reliable operation of an 1 Å FEL providing full transverse coherence of the radiation becomes possible only at relatively high energies of approximately 25 GeV. Parameters of the 1 ÅFEL amplifier operating at the electron beam energy of 25 GeV are presented in Table 1. Undulator tapering is nesessray because the large energy loss of the electron due to incoherent undulator radiation. Tuning of the electron beam energy in the limits of 25 GeV – 10 GeV allows to tune the radiation wavelength in the range of 1 Å – 6.25 Å.

Parameters of an FEL amplifier, covering the radiation wavelength ¿from 2.4 Å to 15 Å, are presented in Table 1. The choice of parameters of this FEL amplifier is defined mainly by limitations due to quantum fluctuations of undulator radiation, while there is no significant problem to provide full transverse coherence of the radiation.

It should be noticed that the undulators for the low energy beamline could be manufactured as planar or as helical. Both designs are within the limits of the present day technology (see next section).

In the present design an option for a 1 Å FEL at the high energy beamline (25 GeV – 50 GeV) is considered as a perspective allowing to achieve higher radiation power (see Table 1). The undulator for this FEL amplifier is a helical one which makes FEL operation less sensitive to the quantum fluctuations of the undulator radiation. A peculiar feature of this FEL amplifier is that the energy spread in the electron beam at the undulator exit exceeds significantly the initial energy spread. It means that requirements for the value of the initial energy spread in the electron beam could be relaxed significantly compared with the requirements for operation at lower energy of electron beam (see Table 1). Another argument in the favor of a higher energy option for the driving electron beam refers to the improvement of the transverse coherence of the radiation and the reduced sensitivity to undulator field errors.

In case an even smaller wavelength is required by future users, the present design can be easily extended to harmonic generation in a second undulator, using the fact that the electron beam is already bunched by the FEL interaction [13, 14]. The bunched electron beam contains fourier components at all higher harmonics. Therefore, a short undulator tuned to either second or third harmonic could extend the wavelength range down to 0.3Å. In principle, going to even higher harmonics is conceivable.

Simulations have been performed for the two undulators of beamline I, employing the same undulator period as for the fundamental wavelength, with as only difference a changed undulator parameter K to tune to the proper wavelength. The most important results, extending the wavelength range to 0.33 Å, are shown in Table 2.

As can be seen, the additional undulator length needed is only some ten percent of the length required for 1 Å radiation. The peak power is still in the order of a GW, approximately two orders of magnitude below the saturation power of the fundamental. Simulations for 10 GeV, or for both energies for undulator II show similar results.

The flux reduction from fundamental to third harmonic for an energy of 10 GeV is two orders of magnitude. For the 25 GeV case, the flux in the third harmonic is only two orders of magnitude larger than spontaneous emission. For higher electron beam energies (undulator III), the power is again in the GW range, with a corresponding increase in flux by an order of magnitude. The only way to extend the wavelength range to smaller wavelengths with a larger peak power is to generate it ¿from an initially unbunched beam, with an undulator length increased by an order of magnitude.

References

[1] R. Tatchyn et al., Nucl. Instrum. and Methods **A375**(1996)274.

[2] Conceptual Design of a 500 GeV e+e− Linear Collider with Integrated X-ray Laser Facility (Editors R. Brinkmann, G. Materlik, J. Rossbach, A. Wagner), DESY Print DESY97-048, Hamburg, 1997.

[3] "A VUV Free Electron Laser at the TESLA Test Facility: Conceptual Design Report", DESY Print TESLA-FEL 95-03, Hamburg, DESY, 1995.

[4] D.A. Edwards, editor, "TESLA Test Facility Linac: Design Report", DESY Print TESLA 95-01, Hamburg, DESY, 1995.

[5] E.L. Saldin, E.A. Schneidmiller and M.V. Yurkov, Phys. Rep. **260**(1995)187.

[6] J. Rossbach, E.L. Saldin, E.A. Schneidmiller and M.V. Yurkov, Nucl. Instrum. and Methods **A374**(1996)401.

[7] E.L. Saldin, E.A. Schneidmiller and M.V. Yurkov, Opt. Commun. **97**(1993)272.

[8] E.L. Saldin, E.A. Schneidmiller and M.V. Yurkov, Opt. Commun. **95**(1993)14.

[9] T.-M. Tran and J.S. Wurtele, Comp. Phys. Commun. **54**(1989)263.
P. Jha and J.S. Wurtele, Nucl. Instrum. and Methods **A331**(1993)477.

[10] K.J. Kim, Phys. Rev. Lett. **57**(1986)1871.

[11] E.L. Saldin, E.A. Schneidmiller and M.V. Yurkov, DESY Print April 1996, TESLA-FEL 96-07, Hamburg, DESY, 1996.

[12] R. Bonifacio, C. Pellegrini and L. Narducci, Opt. Commun. **50**(1984)373.

[13] R. Bonifacio, L. De Salvo Souza, P. Pierini and E.T. Scharlemann, Nucl. Instrum and Methods **A304**(1991)224.

[14] F. Ciocci, G. Dattoli, A. De Angelis, B. Faatz, F. Garosi, L. Giannessi, P.L. Ottaviani and A. Torre, IEEE J. Quantum Electr. **QE-31**(1995)1242.

Table 1. X-ray free electron lasers at TESLA

	Units	U1	U2	U3
Electron beam				
Energy	GeV	10/25	10/25	25/50
Peak current	kA		5	
rms bunch length	μm		23	
Bunch separation	ns		93	
# of bunches per train	#		11315	
Repetition rate	Hz		5	
Normalized rms emittance	π mm mrad		1	
External β-function	m	6/15	8/20	7.5/15
rms beam radius	μm	18	20	12
rms energy spread (entrance)	MeV	1	1	1/4
rms energy spread (exit)	MeV	1.1/3.5	1.1/3.5	3/18
Energy loss in undulator (SR)	MeV	1.7/27	1.7/27	22/185
Undulator				
Type		planar	planar	helical
Period	cm	5	7	7
Peak magnetic field	T	0.887	0.85	0.785
Undulator parameter	#	4.14	5.55	5.13
Coherent radiation				
Wavelength	Å	6.25/1	15/2.4	4/1
Saturation length	m	33 /87	35/87	45/95
Peak power	GW	74 /65	85	280/200
Average power	kW	0.9 /0.8	1	3.4/2.4
rms spot size at the undulator exit	μm	27/25	28	21/17
rms angular divergence	μrad	3.6/0.75	6/1.4	3.2/0.8
Bandwidth	%	0.2	0.2	0.2
Peak spectral brilliance	B*	1.2/6.6	0.57/3.5	7/20
Average spectral brilliance	B**	1.4/8	0.68/4.2	8.5/24
Incoherent radiation				
Average SR power	kW	0.1/1.6	0.1/1.6	1.3/11

*In units of 10^{33} photons/sec/mrad^2/mm^2/(0.1 % bandwidth).
**In units of 10^{25} photons/sec/mrad^2/mm^2/(0.1 % bandwidth).

Table 2. Harmonic generation at 25 GeV

	Units	2nd harm.	3rd harm.
Undulator			
Type		planar	planar
Period	cm	5	5
K-parameter	#	2.84	2.25
Radiation			
Wavelength	Å	0.5	0.33
Peak power	GW	3	0.2
Saturation length	m	11	12
Peak flux*	#	8.6×10^{23}	3.3×10^{22}
Peak brilliance**	#	6.9×10^{32}	6.0×10^{31}
Average brilliance**	#	8.3×10^{24}	7.2×10^{23}

*In units of photons/sec.
**In units of photons/sec/mrad^2/mm^2/(0.1 % bandwidth).

Two-stage SASE FEL as Fully Coherent X-ray Laser

J. Feldhaus[a], E.L. Saldin[b], J.R. Schneider[a],
E.A. Schneidmiller[b], M.V. Yurkov[c]

[a] *Hamburger Synchrotronstrahlungslabor (HASYLAB) at Deutsches Elektronen-Synchrotron (DESY), Notkestrasse 85, D-22607 Hamburg, Germany*

[b] *Automatic Systems Corporation, 443050 Samara, Russia*

[c] *Joint Institute for Nuclear Research, Dubna, 141980 Moscow Region, Russia*

Abstract

A novel scheme of a two-stage single-pass SASE FEL has been proposed in paper [1]. The scheme consists of two undulators and an X-ray monochromator located between them. The process of amplification in a two stage SASE FEL starts from noise as in the case of conventional SASE FEL, but characteristics of the output radiation differ significantly from those of conventional SASE FEL. It is shown in this paper that the output radiation from a two-stage SASE FEL possesses all the features which usually refer to laser radiation: full transverse and longitudinal coherence of the radiation within the radiation pulse and stability of the output power.

1. Introduction

Free-electron laser technique provides the possibility to extend the energy range of lasers into the X-ray regime using a single-pass FEL amplifier scheme starting from noise [2, 3, 4, 5]. One particular feature of the FEL amplifier is its rather large amplification bandwidth. This can be considered an advantage when the FEL amplifier amplifies the narrow bandwidth radiation of a master laser, but in the case when the process of amplification starts from noise, it produces relatively wide band output radiation. For instance, the bandwidth of the 6 nm conventional single-pass SASE FEL at DESY would be about 0.5 %. The shape of the spectrum is not smooth but spiked. To perform experiments which require a narrow bandwidth of the output radiation, a monochromator has to be installed at the FEL amplifier exit. The shot-to-shot fluctuations of the radiation power after this monochromator will increase with increasing energy resolution. Moreover, conventional X-ray optical elements will suffer from heat load due to the high output radiation power and probably filters have to be installed before the monochromator. As a result, the brilliance of the FEL radiation available at the experimental station might be reduced significantly.

A novel scheme of a two-stage single-pass SASE FEL has been proposed in paper [1]. The FEL scheme consists of two undulators and an X-ray monochromator located between them (see Fig.1). The first undulator operates in the linear regime of amplification starting from noise and the output radiation has the usual SASE properties. After the exit of the first undulator the electron is guided through a bypass and the X-ray beam enters the monochromator which selects a narrow band of radiation. At the entrance of the second undulator the monochromatic X-ray beam is combined with the electron beam and is amplified up to the saturation level.

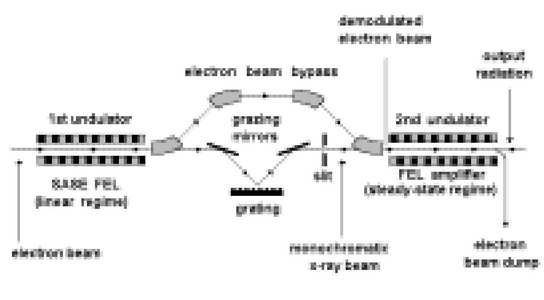

Fig. 1. The principal scheme of a single-pass two-stage SASE X-ray FEL with monochromator.

In this paper we study characteristics of the output radiation from a two-stage SASE FEL. Operation of a two-stage SASE FEL is illustrated for the example of the 6 nm option SASE FEL at the TESLA Test Facility under construction at DESY [3, 4].

2. Operation of a two-stage SASE FEL at DESY

Optimization of parameters for a two-stage SASE FEL at the TESLA Test Facility at DESY has been performed in ref. [1]. All main parameters of the electron beam (peak current, energy spread and emittance) and of the undulator (period, magnetic field and external focusing) are identical to those of a single-pass SASE FEL at DESY [3].

The first stage of the SASE FEL of 12 m length operates in a linear high-gain regime with a power gain of $G^{(1)} \simeq 10^5$. This value is by 1000 times less than the power gain at saturation, $G_{\mathrm{sat}}(\mathrm{SASE}) \simeq 10^8$. At such a choice of the power gain in the first stage the energy spread induced by the FEL process is $\Delta\sigma_{\mathcal{E}}/\mathcal{E} \simeq 10^{-4}$ which is much less than the initial energy spread in the beam, $\sigma_{\mathcal{E}}/\mathcal{E}/\mathcal{E} \simeq 10^{-3}$. Fluctuations of the beam current act as input signal, and the effective power of shot noise at the undulator entrance is equal to 100 W. The output power averaged over the radiation pulse is equal to 10 MW. The spectral bandwidth of the output radiation is about $(\Delta\lambda/\lambda)_{\mathrm{SASE}} \simeq 0.5\%$. Output radiation from the first stage has full transverse coherence and transverse distribution of the radiation field corresponds to fundamental TEM_{00} mode of the FEL amplifier.

The monochromator for the TTF-FEL should be able to select any energy between $\simeq$ 50 eV and $\simeq$ 200 eV with a resolution $\Delta\omega/\omega \simeq 5\times10^{-5}$. Rowland circle grating monochromator appears to be ideally suited for this purpose since the magnification of the spherical grating is always unity, independent of wavelength. A preliminary estimation of the transmission shows that a value of the order of 10 % is realistic: for all mirrors we use carbon coatings and grazing angles of incidence of $\simeq 4^0$, giving a reflectivity of 90 % for each mirror. Assuming a grating efficiency of 15 % and five mirrors with 90 % reflectivity we obtain a total transmission of nearly 9 %.

The modulation of the electron beam induced in the first undulator is suppressed prior arrival of the electron bunch to the entrance of the second undulator. This is possible because of the finite value of the natural energy spread in the beam and special design of the electron bypass. As a result, at the chosen parameters for the first stage of the SASE FEL and the monochromator the radiation power from the monochromator dominates significantly over the shot noise and the residual electron bunching, and the second stage of the FEL amplifier operates in the steady-state regime.

3. Characteristics of the output radiation

The characteristics of the two-stage SASE FEL operating at saturation are presented in Figs.2–6. The FEL process in the second stage has been calculated using the 2-D steady-state code FS2R [6]. Application of the steady-state approach is justified by the fact that the bandwidth of the radiation at the entrance of the second stage is much less than the bandwidth of the FEL amplifier.

The first undulator of the two-stage SASE FEL operates in the high gain linear regime starting from noise. The probability for a certain power $P(t)$ at a time t at the output of the first undulator is given by the negative exponential probability density function [7]:

$$w(P)dP = \exp(-P/\langle P\rangle)dP/\langle P\rangle ,$$

where $\langle P(t)\rangle$ is the temporal profile of the radiation pulse and $\langle\ldots\rangle$ denotes shot-to-shot averaging. The monochromator does not change this distribution since it is merely a linear filter. However, it changes the characteristic time scale to $(\lambda/c)(\Delta\lambda/\lambda)_{\mathrm{m}}^{-1}$ because its bandwidth $(\Delta\lambda/\lambda)_{\mathrm{m}}$ is considerably smaller than that of the FEL amplifier. This also ensures that the second amplifier works in the steady state regime. The radiation power at the exit of the monochromator (averaged over shot-to-shot fluctuations) is much

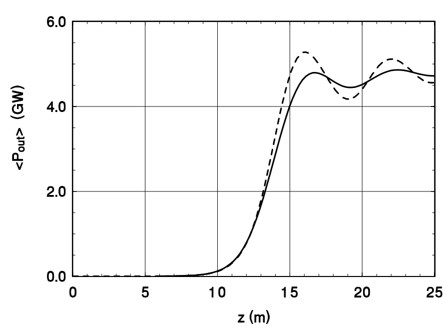

Fig. 2. Average output power at the exit of the second stage of the two-stage FEL amplifier as a function of undulator length (solid curve). The input power fluctuates in accordance with the negative exponential distribution with the average value of 10 kW. The dashed curve represents the output power of the FEL amplifier operating in the steady-state regime at the value of input power P_{in} = 10 kW.

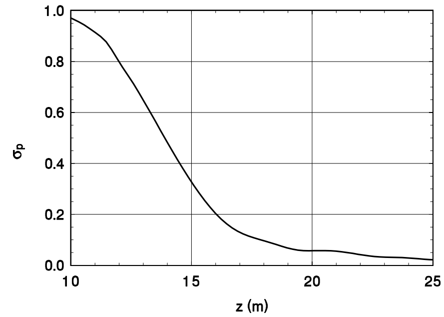

Fig. 3. The dependence of the standard deviation of the fluctuations of the output power as a function of the undulator length ($\sigma_P^2 = \langle P^2 - \langle P \rangle^2 \rangle / \langle P \rangle^2$).

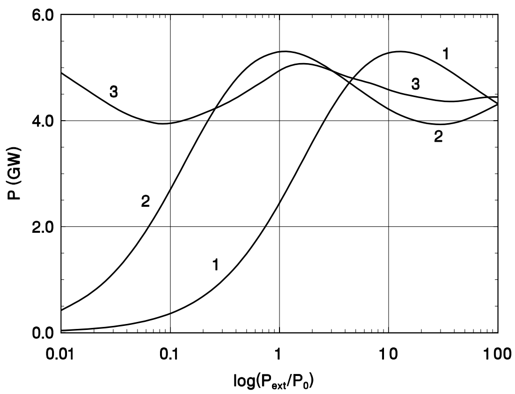

Fig. 4. Dependence of the output power on the input power for the FEL amplifier operating in the steady-state regime, (1): For an undulator length $L_{\mathrm{w}} = 14$ m, (2): $L_{\mathrm{w}} = 16$ m, (3): $L_{\mathrm{w}} = 20$ m. Nominal input power $P_0 = 10$ kW.

larger than the effective power of shot noise at the entrance of the second undulator. Therefore, the second stage operates in the steady-state regime with the probability close to unity.

The dependence of the average (shot-to-shot) output radiation power on the undulator length of the second stage is presented in Fig. 2. The input power fluctuates in accordance with the negative exponential distribution with the average value of 10 kW. It is seen from Fig. 3 that the fluctuations of the output power reduce significantly when the second stage of the FEL amplifier operates in a nonlinear mode. This feature can be simply understood when one plots the dependence of the output power on the input power for the FEL amplifier operating in the steady-state regime (Fig. 4). It is seen that a higher stability of the output radiation power can be achieved by increasing the length of the undulator. In Fig. 5 we present

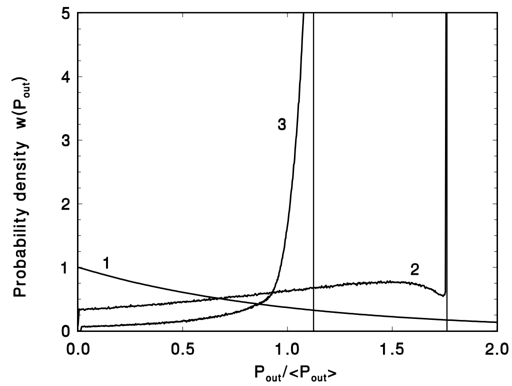

Fig. 5. The probability density function of the output radiation of the two-stage SASE FEL for different lengths of the second undulator. Curve (1) is the probability density function of the input radiation (negative exponential distribution), and curves (2) and (3) correspond to a length of the second undulator of $L = 14$ m and $L = 16$ m, respectively.

the probability density function for the output radiation power[1]. It is seen that in the nonlinear mode of operation the distribution shrinks. For instance, at a length of the second undulator of 20 m, the mean-squared fluctuations of the output power are below 10 %. In the case under study the length of the longitudinal coherence is about the same as the length of the radiation pulse, so shot-to-shot fluctuations of the energy of the radiation pulse show the same behaviour as the fluctuations of the radiation power.

Fig.6 presents the spectral distribution of the energy in one radiation pulse of the FEL amplifier operating in the steady-state regime for an input power P_{in} = 10 kW and an undulator length $L_{\mathrm{w}} = 16$ m (saturation point). Curve 2 in this plot represents the typical spectrum of a conventional SASE FEL operating at saturation. The output radiation power of the two-stage SASE FEL is close to that of the conventional SASE FEL while the spectral bandwidth is by two orders of magnitude narrower. Thus, the brilliance of the output radiation exceeds the corresponding value of a conventional SASE FEL by two orders of magni-

[1] In the case under study the probability density function of the input radiation power is given by the negative exponential distribution, so the probability density function of the output radiation power is given by the expression:

$$w(P_{\mathrm{out}}) = \frac{1}{< P_{\mathrm{in}} >} \sum_n \exp\left[-P_{\mathrm{in}}^{(\mathrm{n})}(P_{\mathrm{out}})/ < P_{\mathrm{in}} >\right] |\frac{dP_{\mathrm{in}}^{(\mathrm{n})}}{dP_{\mathrm{out}}}| ,$$

where the sum over n must be taken over all branches of the function $P_{\mathrm{in}}(P_{\mathrm{out}})$ (see Fig. 4). The singularities of the probability density functions plotted in Fig. 5 correspond to the saturation point in Fig. 4 where $|dP_{\mathrm{out}}/dP_{\mathrm{in}}| = 0$.

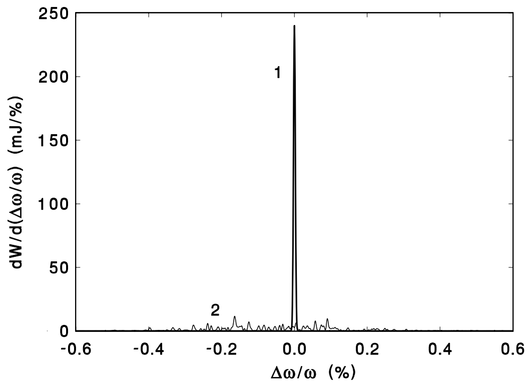

Fig. 6. Spectral distribution (1) of the energy in one radiation pulse of the FEL amplifier operating in the steady-state regime for an input power $P_{\rm in} = 10$ kW and an undulator length $L_{\rm w} = 16$ m (saturation point). Curve (2) presents the typical spectrum of a conventional SASE FEL operating at saturation.

tude. The spectral bandwidth of $\Delta\lambda/\lambda \simeq 5 \times 10^{-5}$ is close to the limit given by the finite duration of the radiation pulse.

4. Conclusion

It is shown in this paper that realization of a two-stage FEL scheme at the TESLA Test Facility at DESY will allow one to reduce the bandwidth of the output radiation (and to increase the brilliance) by two orders of magnitude with respect to a single-pass scheme, while the peak and the average output power are the same. Shot-to-shot fluctuations of the output radiation power from a two-stage SASE FEL can be reduced to below 10 %. Moreover, in a two-stage scheme the heat load on the monochromator is 10^3 times less than that on a monochromator installed at the exit of a conventional single-pass SASE FEL. The output radiation from a two-stage SASE FEL possesses all the features which usually refer to laser radiation: full transverse and longitudinal coherence of the radiation within the radiation pulse and stability of the output power. The realization of this scheme at the TESLA Test Facility at DESY would allow to construct a tunable X-ray laser with a minimum wavelength around 6 nm, a micropulse duration of 200 fs, a peak power of 5 GW and an average power of 100 W. The degeneracy parameter of the output radiation of such an X-ray laser would be about 10^{14} and thus have the same order of magnitude as that of quantum lasers operating in the visible.

Acknowledgement

We thank G. Materlik, D. Trines and B.-H. Wiik for their interest in this work. We are grateful to J. Rossbach and M. van der Wiel for many useful discussions.

References

[1] J. Feldhaus, E.L. Saldin, J.R. Schneider, E.A. Schneidmiller and M.V. Yurkov, "Possible Application of X-ray Optical Elements for Reducing the Spectral Bandwidth of an X-ray SASE FEL", presented at XVIII International Free Electron Laser Conference (Rome, 1996).

[2] R. Tatchyn, J. Arthur, M. Baltay et al., Nucl. Instrum. and Methods **A375**(1996)274.

[3] "A VUV Free Electron Laser at the TESLA Test Facility: Conceptual Design Report", DESY Print TESLA-FEL 95-03, Hamburg, DESY, 1995.

[4] J. Rossbach, Nucl. Instrum. and Methods **A375**(1996)269.

[5] Conceptual Design of a 500 GeV e+e− Linear Collider with Integrated X-ray Laser Facility (Editors R. Brinkmann, G. Materlik, J. Rossbach, A. Wagner), DESY Print 97-048, Hamburg, 1997.

[6] E.L. Saldin, E.A. Schneidmiller and M.V. Yurkov, Optics Comm. **95**(1993)141.

[7] J. Feldhaus, E.L. Saldin, J.R. Schneider, E.A. Schneidmiller and M.V. Yurkov, SPIE Proceedings **2988**(1997)145.

Estimation of the thermal emittance of electrons emitted by Cesium Telluride photo cathodes

Klaus Flöttmann

DESY, Notkestr. 85, 22603 Hamburg, Germany

Abstract

Based on early measurements by Powell et al [1] the thermal emittance of electrons emitted by Cesium Telluride (Cs_2Te) photo cathodes is estimated. The applicability of the estimations to the case of an rf gun is discussed and the necessity of additional measurements is emphasized.

Introduction

The thermal (i.e. initial) emittance of an electron beam generated by a (photo) cathode imposes a lower limit for the normalized emittance that can be generated by an injector. In case of the TTF FEL-injector the beam is generated by a Cs_2Te cathode illuminated by frequency quadrupled laser light from a Nd:YLF laser with a photon energy of Eph= 4.72eV (λ=263nm). The normalized thermal emittance depends on the spot size, the momentum distribution and the angular distribution of the emitted electrons. While the spot size has to be optimized with respect to the emittance development in the gun (rf induced emittance vs. emittance growth due to space charge) the energy and the angular distributions are functions of the cathode material and the photon energy. The photoemission process can be considered in three steps: Optical excitation of electrons, migration of the electrons to the solid surface (with or without scattering) and, if the electron energy is high enough, escape across the surface potential barrier into the vacuum. For the excitation process direct and nondirect transitions have to be distinguished. Spicer [2] has suggested to explain strong nondirect transitions that occur for example in Cs_2Te but also in some metals like Cu in terms of many-body effects rather than in terms of phonon assisted transitions. While in a direct transition the photon energy is transferred completely to the electron, the energy is distributed between the electron and the remaining hole in case of the nondirect transition. According to Spicer the hole is localized for a time long compared to the excitation process and electronic and/or ionic relaxation processes lead to a many-body excitation. The photoemission data can be discussed in a model in which the probability $P(E_f,Eph)$ for a photon of energy Eph exciting an electron to a final state energy E_f, is proportional to:

$$P\left(E_f, Eph\right) \propto N_f(E_f) \cdot N_i(E_f - Eph) \qquad (1)$$

where $N_f(E_f)$ and $N_i(E_f\text{-}Eph)$ are the density of initial and final states, respectively.

Photoemission data of Cs_2Te

Figure 1 shows the spectral response of a Cs_2Te cathode as measured by Powell and coworkers [1]. The little shoulder below 3.5eV is likely to be generated by an additional phase of Cs_2Te [4]. Since its quantum yield is low is will not affect the thermal emittance of the electrons. The threshold energy of Cs_2Te is hence $E_T = 3.5eV$. The quantum efficiency increases with increasing photon energy up to ~6.6eV. The photoemission behavior above 6.6eV is influenced by the onset of electron-electron scattering of the optically excited electron (producing an electron-hole pair). Since the scattered electrons have energies below threshold the quantum efficiency decreases. Electron-electron scattering can occur only for electron energies exceeding twice the gap width E_G, which is hence determined as $E_G = 3.3eV$. The electron affinity is given as: $E_A = E_T - E_G = 0.2eV$.

Figure 2 shows the normalized energy distribution of emitted photoelectrons for various photon energies. Since the photon absorption length is smaller than the phonon scattering length in case of Cs_2Te the electrons below the electron-electron threshold lose practically no energy on the way to the surface. The first peak P1 is located independently of the photon energy (nondirect transition) at 4.05eV above the valence band maximum. (The actual position of the maximum may lie somewhat lower but be obscured by the surface potential barrier [1].) The maximum is associated with a maximum in the conduction band density of states.

Peaks P2 and P3 change the position with the photon energy (direct transition) and are associated with maxima in the valence band density of states. The final state energies are given as:

$$E_{P2} = Eph - 0.7eV$$
$$E_{P3} = Eph - 1.4eV \qquad (2)$$

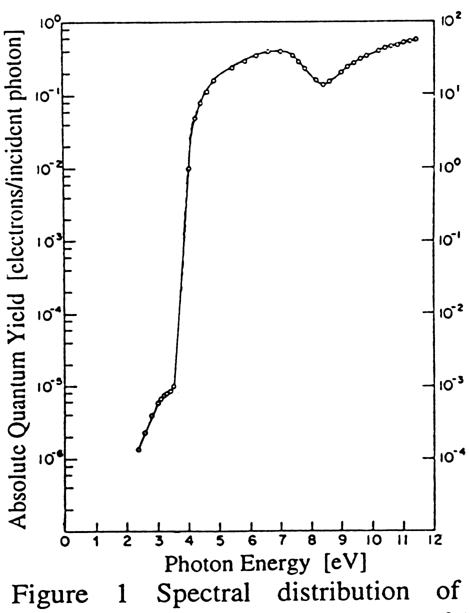

Figure 1 Spectral distribution of the photoelectric yield of Cs_2Te (from ref 1).

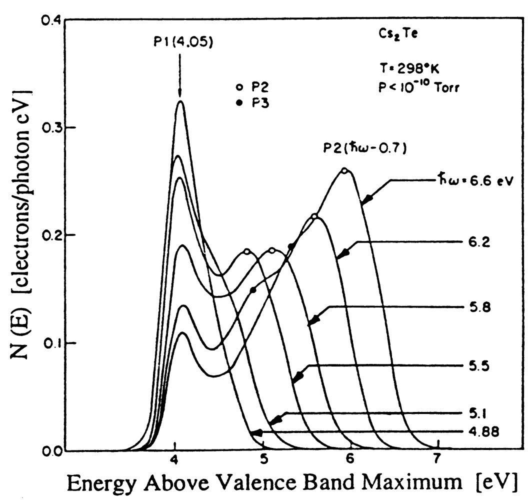

Figure 2 Energy distributions of the photoemitted electrons. The curves have been normalized to the absolute quantum yield shown in Figure 1 (from ref 1).

Higher energy levels in the conduction band density of states will not be discussed, since they can not be excited with the available photon energy of 4.72eV. Neglecting the slight asymmetry of the energy distribution in Figure 2 (for *Eph*=4.88eV) it can be concluded that the electrons are excited to an average final state energy of E_f*=4.05eV*. Figure 3 compiles the data obtained by Powell in a schematic band structure of Cs_2Te.

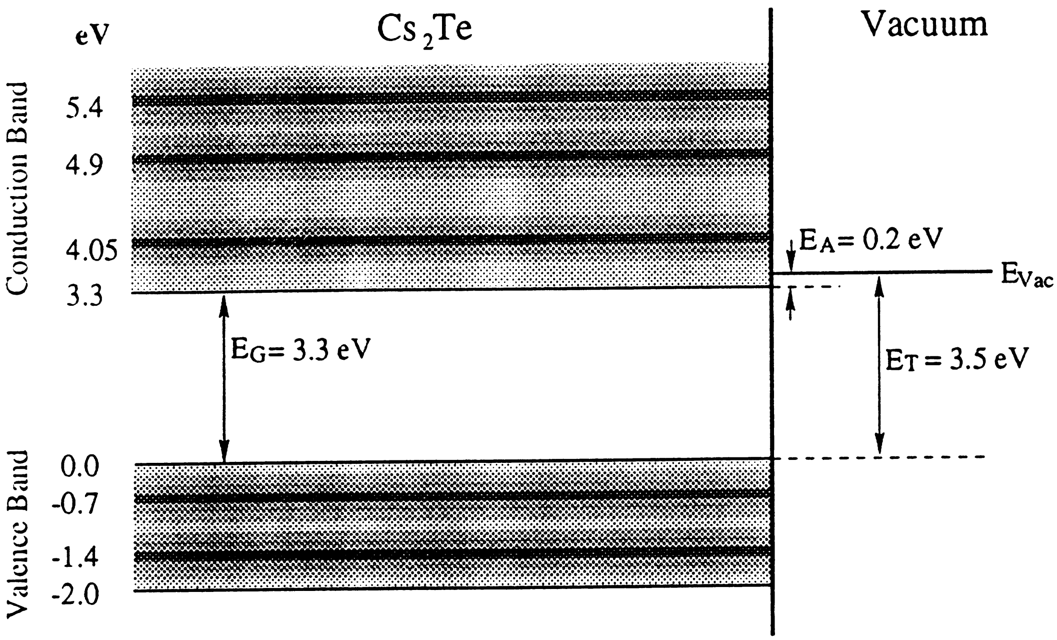

Figure 3 Schematic band structure of Cs_2Te. The maxima of the density of states are indicated as dark shaded areas. The vacuum level is 3.5eV above the valence band maximum. At a photon energy of ~4.7eV electrons are excited to a final state energy of 4.05eV, corresponding to a kinetic energy of a free electron of 0.55eV.

Calculation of the thermal emittance

The rms-emittance ε_{rms} and the normalized rms-emittance $\varepsilon_{n\ rms}$ of a beam with large divergence are defined as:

$$\varepsilon_{rms} = \frac{1}{\overline{pz}} \cdot \sqrt{\langle x^2 \rangle \langle px^2 \rangle - \langle x \cdot px \rangle^2}$$

$$\varepsilon_{n\ rms} = \frac{1}{m_0 c} \cdot \sqrt{\langle x^2 \rangle \langle px^2 \rangle - \langle x \cdot px \rangle^2} \qquad (3)$$

$\langle\ \rangle$ = second central moment of the distribution

$\overline{pz}$ = average longitudinal momentum

At the source $\langle x \cdot px \rangle$ is zero, the normalized emittance can therefore be written as:

$$\varepsilon_{n\ rms} = x_{rms} \cdot \frac{px_{rms}}{m_0 c} \qquad (4)$$

We consider the case of a uniform radial distribution with radius r=1.5mm, hence:

$$x_{rms} = \frac{r}{2} = 0.75 \cdot 10^{-3} m \tag{5}$$

Powell's measurements are made in a spherical geometry, i.e. they represent an integration over all emission angles in the half-sphere over the cathode (details of the measurement device can be found in ref. 3). In order to investigate the effect of the surface potential barrier we consider two model cases:

The first case might be thought of as if a little gap exists between the surface of the cathode and the potential barrier. The electrons are emitted isotropically into the half-sphere over the cathode with the kinetic energy $E_{kin} = E_f - E_G = 0.75eV$. If no scattering occurs in the barrier only the average longitudinal momentum is changed and the normalized emittance would be conserved if all particles would overcome the barrier. Particles with angle φ larger as $\varphi_{\max} = \arccos\sqrt{\frac{E_A}{E_{kin}}}$ (with respect to the surface normal) will however not pass the potential barrier. The emittance can therefore be calculated by restricting the emission angle accordingly. The transverse momentum *px* is given as:

$$px = p \cdot \sin\varphi \cdot \cos\Theta \tag{6}$$

where $\varphi=[0, \varphi_{max}]$ and $\theta=[0, 2\pi]$ are the azimuth and meridian angles, respectively. With

$$p = m_0 c\sqrt{\gamma^2 - 1} \cong m_0 c\sqrt{\frac{2E_{kin}}{m_0 c^2}} \tag{7}$$

and

$$px_{rms} = \sqrt{\frac{\iint px^2 \sin\varphi d\varphi d\Theta}{\iint \sin\varphi d\varphi d\Theta}} \tag{8}$$

the normalized rms emittance is given as:

$$\varepsilon_{n\,rms} = \frac{r}{2} \cdot \sqrt{\frac{2E_{kin}}{m_0 c^2}} \cdot \frac{1}{\sqrt{3}} \cdot \sqrt{\frac{2 + \cos^3\varphi_{\max} - 3\cos\varphi_{\max}}{2 \cdot (1 - \cos\varphi_{\max})}} \tag{9}$$

$$= 0.58\pi\, mrad\; mm \text{ for } E_A = 0.2eV$$

In the second case it is assumed that due to scattering the electrons are emitted isotropically with an average kinetic energy of $E_{kin}=E_f-E_G-E_A=0.55eV$ into the half-sphere over the cathode (already behind the surface potential barrier). With $\varphi_{max}=\pi/2$ equation 9 reduces to

$$\varepsilon_{n\,rms} = \frac{r}{2} \cdot \sqrt{\frac{2E_{kin}}{m_0 c^2}} \cdot \frac{1}{\sqrt{3}} = 0.64\pi\, mrad\; mm \tag{10}$$

Figure 4 shows a comparison of the two models as function of the ratio $E_A/(E_f-E_G)$. The difference of the thermal emittance is only small even though the phase space looks somewhat different for the two cases.

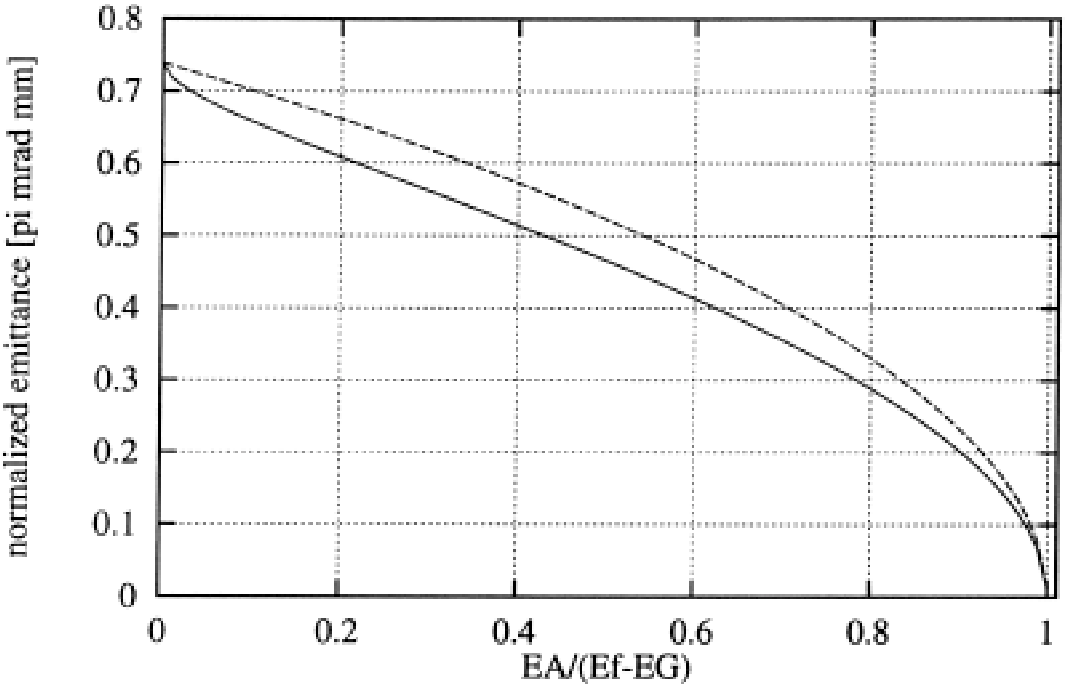

Figure 4 Estimated normalized thermal emittance of electrons emitted from Cs_2Te cathodes as function of the electron affinity (radius of the source r=1.5mm, photon energy *Eph*=4.72eV). The solid line refers to case one (no scattering), the dashed line refers to case two (with scattering).

The nature of the surface potential barrier and the details of the emission process are not well known. The barrier may act as a much stronger filter for particles with large transverse momenta as discussed before. Only angular resolved measurements of the emission spectra will allow a precise determination of the thermal emittance. The previously estimated thermal emittance may hence be considered as an upper limit only.

Discussion

Powell's measurements were made on 120nm thick Cs_2Te specimens on Mo and Pt substrates at room temperature and at a vacuum pressure below 10^{-10}mbar. The cathodes for the TTF gun are produced in a preparation chamber under construction at INFN Milan. They are only about 20nm thick and are deposited on a Mo substrate. Measurements of the spectral response show a similar behavior than Powell's results (Figure 1) [4] indicating that Powl's measurements are applicable in case of the fresh prepared cathodes. In the gun itself, however, the thermal emittance might be influenced by

-the temperature of the cathode
-poisoning of the cathode due to the increased vacuum pressure
-rf fields.

The transition processes in Cs_2Te are known to be insensitive to temperature variations. For this reason Spicer argued about many-body effects rather than phonon assisted nondirect transitions [2]. Measurements at CERN [5] showed no significant variation of the quantum efficiency up to ~120°C. Therefore an effect of the temperature on the thermal emittance is not to be expected in case of Cs_2Te.
While in a high vacuum environment the quantum efficiency of Cs_2Te cathodes is highly independent of time, it drops from the initial value of ~10% down to a level of ~2% in a few hours in the gun environment. At this level the quantum efficiency stays nearly constant for some month. The reduced quantum efficiency is attributed to the increased vacuum pressure in the gun. Poisoning of the cathode with gases like oxygen and carbondioxide has been investigated in some detail under laboratory conditions [4]. Depending on the partial pressure of the gas the reduction of the quantum efficiency seems to be due to a diffusion process into the cathode film or by a passivation of the cathode surface. In the first case the structure of the density of states might be changed while in the second case the electron affinity is changed. Especially in the latter case a reduction of the thermal emittance is to be expected according to the previously discussed models. As a first hint a measurement of the threshold energy of cathodes with reduced quantum efficiency would be useful. It should be noted, that an effect of gases like oxygen on the thermal emittance might be useful in order to reduce the thermal emittance as part of the production procedure.
High electric fields may reduce the surface potential barrier and hence increase the thermal emittance in an rf gun. Schottky has investigated the effect for the electron emission from metals [6, 7]. He assumes that the form of the surface potential barrier is determined by the retracting force of image charges in the metal. Cs_2Te is a dielectric semiconductor, hence Schottky's theory is not applicable. The electron affinity might also be influenced by other effects, for example by to a polarized surface layer due to an asymmetric electron density at the surface. A measurement of the thermal emittance under high field conditions would be difficult but a measurement of the quantum efficiency at different fields can be made in an rf gun. (First indications of a modified Schottky effect at Cs_2Te cathodes have been found at CERN [8].) The quantum efficiency depends on the total number of electrons with energy above the electron affinity, thus it is a function of the density of states. Therefore no general relation exists between the quantum efficiency and the electron affinity as in case of metals. For a given photon energy an approximate relation can be calculated by integrating the energy distribution (Figure 2) as function of the lower integration boundary. Since the density of states between 3.5eV and 3.3eV above the valence band maximum is not known in detail this relation holds only, if the electron affinity is above 0.2eV during the measurement, i.e. if the cathode is appropriately poisoned.

Conclusion

The photoemission of electrons from Cs_2Te is for photon energies below ~5eV dominated by a nondirect transition with a final state energy of 4.05eV. The electron energy is insensitive for a small variations of the photon energy and insensitive to temperature variations. The normalized thermal emittance of electrons emitted from Cs_2Te cathodes in an ultra high vacuum environment has been estimated to be $\varepsilon_{n\,\mathrm{rms}} \leq 0.65\pi$ mrad mm (for a spot size of *r=1.5mm*). In the rf gun environment it is probably lower due to an increased electron affinity. In order to improve the understanding of the thermal emittance, measurements are required that reveal the angular distribution of the emitted electrons. The effect of cathode poisoning and the effect of high electric fields on the thermal emittance have to be investigated experimentally.

Acknowledgment

I'm indebted to J. Roβbach for stimulating discussions and useful suggestions.

References

1 R. A. Powell, W. E. Spicer, G. B. Fisher, P. Gregory 'Photoemission Studies of Cesium Telluride', Physical Review B8, No8, 3978-3995 (1973).

2 W. E. Spicer, 'Possible Non-One-Electron Effects in the Fundamental Optical Excitation Spectra of Certain Crystalline Solids and their Effect on Photoemission' Physical Review 154, No2, 385-394 (1967).

3 R. C. Eden 'Techniques for the Measurement of Photoemission Energy Distribution Curves by the ac Method', Review of the Scientific Instruments 41, No2, 252-258 (1970).

4 P. Michelato, C. Pagani, D. Sertore, A. di Bona, S. Valeri 'Characterization of Cs_2Te photoemissive film formation, spectral response and pollution' FEL Conference 96, Rom and TESLA-FEL 96-13 (1996).

5 G. Suberluq 'Photocathodes for the CERN CLIC Test Facility', Proceedings of the International Workshop SOURCES '94, Schwerin Germany, 557-561 (1994).

6 W. Schottky 'Über den Einfluß von Strukturwirkungen, besonders der Thomsonschen Bildkraft, auf die Elektronenemission der Metalle' Phys. ZS. 15, 872-879 (1914).

7 W. Schottky 'Über kalte und warme Elektronenentladungen' Zeitschrift für Physik 14, 63-106 (1923).

8 G. Suberluq, presented at FEL Conference 96, Rom.

A New Method for Ultrashort Electron Pulse-shape Measurement Using Synchrotron Radiation from a Bending Magnet

J. Krzywinski[a], E.L. Saldin[b], E.A. Schneidmiller[b], M.V. Yurkov[c]

[a] *Institute of Physics of the Polish Academy of Sciences, 02688 Warszawa, Poland*

[b] *Automatic Systems Corporation, 443050 Samara, Russia*

[c] *Joint Institute for Nuclear Research, Dubna, 141980 Moscow Region, Russia*

Abstract

A new non-destructive method for measurement of the longitudinal profile of subpicosecond electron bunches is proposed. The method is based on measurements in frequency domain of correlations between the fluctuations of synchrotron radiation produced by an electron bunch passing a bending magnet. The proposed device is the combination of a monochromator and a counting interferometer which gives directly the square of the modulus of the Fourier transform of the longitudinal electron bunch profile. Reconstruction of the beam profile from these data is performed by means of the standard technique developed for the image reconstruction from the data obtained by means of the Handbury-Brown and Twiss intensity interferometer. Because the principle of the method is based essentially on the statistical properties of the synchrotron radiation and the detection process itself these topics are also considered in detail. The signal to noise ratio is analyzed in terms of degeneracy parameter. The degeneracy parameter increases approximately as a third power of the wavelength which makes the visible range of synchrotron radiation to be a natural choice for the spectral intensity correlation measurement. In the end of the paper we illustrate with numerical example the potential of the proposed method for on line, non-destructive diagnostics of the electron beam in the accelerator driving the TESLA Test Facility Free Electron Laser at DESY.

1. Introduction

The length of electron bunches for the next generation linear colliders are of an order of $\sigma_z \simeq 0.1 - 1$ mm [1, 2, 3]. The projects of X-ray FELs require even shorter bunches, down to 0.025 mm [1, 4, 5]. These values are less by an order of magnitude than those used in the existent accelerators. Development of non-destructive methods for measurements of longitudinal distribution of the beam current in such a short bunches is a challenging problem.

Recently the method for measuring ultrashort pulses of incoherent radiation has been proposed [6]. The method is based on detecting the fluctuations of the visibility of interference fringes in a two-beam interferometer.

Here we describe a new method for nondestructive measurement of the longitudinal profile of the electron bunch. The method is based on the measurements in frequency domain of correlations between the fluctuations of synchrotron radiation produced by a bunch passing a bending magnet.

The proposed device is the combination of a monochromator and a counting interferometer which gives directly the square of the modulus of the Fourier transform of the longitudinal electron bunch profile. Reconstruction of the beam profile from these data is performed by means of a standard technique developed for the image reconstruction from the data obtained by means of the Hanbury-Brown and Twiss intensity interferometer.

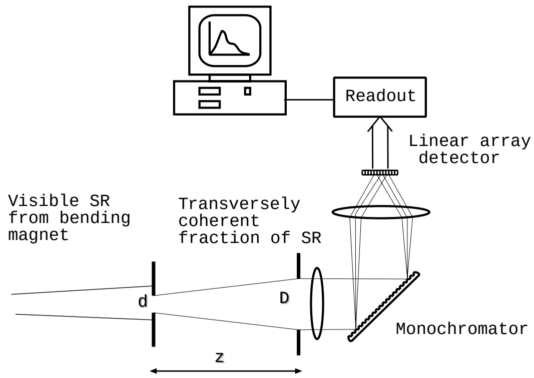

Fig. 1. The layout of the device for measurement the longitudinal profile of the electron pulse.

2. Principle of the method

The layout of the device for measurement the longitudinal profile of the electron pulse is presented in Fig. 1. An ultrarelativistic electron bunch passes a bending magnet and radiates a pulse of synchrotron radiation. The diaphragm of aperture d is used for selection of the transversely coherent fraction of synchrotron radiation which is directed to the monochromator with an aperture D. The monochromator is placed at the distance of z ¿from the diaphragm. The resolution of the monochromator is equal to $\Delta\omega_m$, the central frequency is equal to ω_0 and $\Delta\omega_m/\omega_0 \ll 1$. The radiation reaching the monochromator is transversely coherent when, according to Van Cittert-Zernike theorem, the following condition is fulfilled (see e.g. ref. [7]): $cz/(\omega_0 d) > D$, where c is the velocity of light. A one-dimensional array photodetector is placed at the monochromator exit which performs measurement of the spectral distribution of the radiation energy. The signal from each element of the photodetector is stored in the computer in matrix form. The row index corresponds to the frequency and the column index corresponds to the pulse number. This matrix is used for the calculation of statistical properties of the radiation.

The principle of the operation of the proposed device is based on the statistical properties of synchrotron radiation . The detailed analysis of this subject and the operation of the device is presented in ref [8]. Here, for clarity we present only the main results.

Let us describe an electron bunch profile by the profile function $F(t)$ which gives the probability of the arrival of an electron at the magnet entrance within the time interval $(t, t+dt)$. The electron bunch function $F(t)$ and its Fourier transform $\bar{F}(\omega)$ are connected by Fourier transformation:

$$\bar{F}(\omega) = \int\limits_{-\infty}^{\infty} e^{i\omega t} F(t) dt \ .$$

The first and the second order field correlation functions are defined as

$$g_1(\omega_1 - \omega_2) \equiv \frac{\langle \bar{E}(\omega_1)\bar{E}(\omega_2)\rangle}{\sqrt{\langle |\ \bar{E}(\omega_1)\ |^2\rangle\langle |\ \bar{E}(\omega_2)\ |^2\rangle}} \ ,$$

$$g_2(\omega_1 - \omega_2) \equiv \frac{\langle |\ \bar{E}(\omega_1)\ |^2 |\ \bar{E}(\omega_2)\ |^2\rangle}{\langle |\ \bar{E}(\omega_1)\ |^2\rangle\langle |\ \bar{E}(\omega_2)\ |^2\rangle} \ ,$$

where $\bar{E}(\omega)$ is Fourier component of electric field of the synchrotron radiation.

It is shown in ref. [8] that synchrotron radiation possesses all the features corresponding to completely chaotic polarized light. In particular, the second order correlation function is expressed via the first order correlation function:

$$g_2(\omega_1 - \omega_2) = 1 + |\ g_1(\omega_1 - \omega_2)\ |^2 \ .$$

The explicit expression for the first order correlation function has the form

$$g_1(\omega_1 - \omega_2) = \bar{F}(\omega_1 - \omega_2) \ .$$

We define the interval of spectral coherence $\Delta\omega_c$ as follows:

$$\Delta\omega_c = \int\limits_{-\infty}^{\infty} |\ g_1(\Delta\omega)\ |^2\ d(\Delta\omega) \ .$$

In the case of Gaussian profile of the electron beam:

$$F(t) = \frac{1}{\sqrt{2\pi}\sigma_z} \exp\left(-\frac{t^2}{2\sigma_z^2}\right) \ ,$$

the interval of the spectral coherence is equal to $\Delta\omega_c = \sqrt{\pi}/\sigma_z$.

At sufficient resolution of the monochromator $(\Delta\omega_m \ll \Delta\omega_c)$, it seems to be technically feasible to measure the second order spectral correlation function of Fourier components of electric field of the synchrotron radiation.

$$g_2(\omega_1 - \omega_2) \simeq \frac{\langle K_1 K_2\rangle}{\langle K_1\rangle\langle K_2\rangle}$$

where $K_{1,2}$ - numbers of photocounts of two emblements of the photodetector corresponding to frequencies $\omega_{1,2}$ respectively. This function contains the information about the Fourier transform of the electron bunch profile:

$$g_2(\omega_1 - \omega_2) = 1 + \mid \bar{F}(\omega_1 - \omega_2) \mid^2 \quad .$$

When resolution of the monochromator is worse than the interval of spectral coherence, $\Delta\omega_c \simeq c/\sigma_z$, the mean value-to-dispersion ratio of the photocounts in a given frequency range $\Delta\omega_m$ can be measured. The square of this ratio is equal to M, the number of coherence intervals inside the monochromator linewidth. Analysis of these measurements allows one to estimate the electron bunch length as $\sigma_z \simeq cM/\Delta\omega_m$.

The quantum nature of the photodetection process should be considered when the number K of photocounts in the spectral coherence interval is low . The expression for variance of photocounts fluctuations contains two terms:

$$\sigma_K^2 = \frac{\langle K^2 \rangle - \langle K \rangle^2}{\langle K \rangle^2} = \frac{1}{\langle K \rangle} + \frac{1}{M} \ . \qquad (1)$$

The first term corresponds to the "photon shot noise" and its origin is in the Poisson distribution. The second term corresponds to the classical fluctuations of the energy in the radiation bunch and takes its origin from the shot noise in the electron bunch. The ratio of the classical variance to the "photon shot noise" variance is named as the photocount degeneracy parameter δ_c [7]:

$$\delta_c = \frac{\langle K \rangle}{M} \ . \qquad (2)$$

The formula for calculation of the photocount degeneracy parameter δ_c is given by:

$$\delta_c = \eta R_m \frac{\Delta\omega_m}{M \Delta\omega_c} \delta_W \ , \qquad (3)$$

where η is the quantum efficiency, R_m is the integral reflection coefficient of the monochromator mirrors and the dispersive element and δ_W is the wave degeneracy parameter which is equal to the average number of transversely coherent photons radiated by the electron bunch inside the spectral interval of coherence $\Delta\omega_c$. Physically this parameter describes the average number of photons which can interfere, or, according to the quantum theory, the number of photons in one quantum state (one "mode"). It has been shown in ref. [8] that the value of the wave degeneracy parameter for synchrotron radiation can be estimated as:

$$\delta_W \simeq \frac{B_{peak} \lambda^3}{4c} \ , \qquad (4)$$

where $B_{peak}$is the peak value of spectral brightness and λ is the radiation wavelength.

The signal-to-noise ratio associated with the output of the counting interferometer depends on the photocount degeneracy parameter δ_c as [8]
at $\delta_c \gg 1$:

$$\frac{S}{N} \simeq \frac{\sqrt{N_b} \mid \bar{F}(\omega_1 - \omega_2) \mid^2}{\sqrt{11 \mid \bar{F}(\omega_1 - \omega_2) \mid^4 - 12 \mid \bar{F}(\omega_1 - \omega_2) \mid^2 + 9}} \ , \qquad (5a)$$

at $\delta_c \ll 1$:

$$\frac{S}{N} \simeq \frac{\sqrt{N_b} \delta_c \mid \bar{F}(\omega_1 - \omega_2) \mid^2}{\sqrt{1 + \mid \bar{F}(\omega_1 - \omega_2) \mid^2}} \ , \qquad (5b)$$

where N_b is the number of independent measurements.

For this method to be applicable the radiation wavelength must be much smaller than the bunch length. At a bunch length of the order of 0.1 mm one can use a wide interval of the radiation spectrum, from the infrared down to X-rays. The choice of the optimal value of the operating frequency is influenced by such issues as tolerable value of the signal-to-noise ratio, required resolution of the monochromator ($\Delta\omega_m/\omega \ll c/(\omega\sigma_z)$) and the existence of commercially available detectors and optical elements with the required parameters. The choice of the visible range possesses the following advantages. The degeneracy parameter can reach a value larger than unity and therefore can ensure short measurement time. The required resolution of the monochromator ($\Delta\omega_m/\omega \ll c/(\omega\sigma_z) \simeq 0.1\%$) can be achieved without significant efforts. There is also a highly developed technology of electrooptical devices (optical fibers, fast detectors, electrooptical switches, etc.) operating in the visible wavelength range.

3. Numerical example

The operation of the new method for the electron pulse-shape measurement is illustrated for the TESLA Test Facility which is under construction at DESY [5]. It is supposed to use synchrotron radiation from the last bending magnet of the third bunch compressor (see Table 1). The value of the peak spectral brightness is equal to 10^{17} Phot./(sec$\times$mrad^2$\times$mm^2$\times$0.1% bandw.) and the degeneracy parameter is about of $\delta_W \simeq 10^4$ at the chosen operating wavelength of $\lambda = 5000$ Å .

Table 1. Parameters of SR source

Electron beam	
Energy, $\mathcal{E}_0$	500 MeV
Peak current, I_0	2.5 kA
rms bunch length, σ_z	50 μm
Normalized rms emittance , ϵ_n	2π mm mrad
Number of bunches per train	7200
Repetition rate	10 Hz
Bending magnet	
Length of magnet, L_w	0.5 m
Magnetic field, H	1.3 T
β-function,	11 m
Radiation	
Wavelength, λ_0	5000 Å
Spectral coherence $\Delta\omega_c/\omega_0$	0.3 %
Spectral brightness*	10^{17}
Wave degeneracy parameter, δ_W	10^4

* In units of Phot./(sec$\times$ mrad^2 $\times$mm^2 $\times$0.1% bandw.)

We assume the use of a commercially available monochromator with the resolution of $\Delta\omega_m/\omega \simeq 3\times 10^{-4}$. The electron bunch length is equal to 0.05 mm which corresponds to the relative value of the interval of spectral coherence of $\Delta\omega_c/\omega \simeq 3\times 10^{-3}$. Comparing $\Delta\omega_m$ with $\Delta\omega_c$ one can conclude that ten pixels of the photodetector is sufficient to cover the interval of the spectral coherence. The photocount degeneracy parameter δ_c (see eq. (3)) will be of the order of 10^2 at the quantum efficiency of the detector of $\eta \simeq 0.3$ and the value of the integral reflection coefficient of the monochromator mirrors and dispersive elements of $R_m \simeq 0.3$.

The design value of the emittance of the electron bunch in the TTF accelerator is small, so the visible fraction of the SR from the magnet is always transversely coherent and there is no need in the installation of additional diaphragm (see Fig.1). If the monochromator is placed at the distance of $L = 2$ m from the radiation source, the aperture of the monochromator in the vertical direction should be not smaller than $\Delta\theta_c L \simeq 1$ cm. If vertical aperture is less than this value, the flux of coherent photons is decreased. The aperture of the monochromator in the horizontal plane can not be larger than $\Delta\theta_c L$ due to uniform distribution of the radiation in the horizontal plane.

Let us now estimate the number of shots required for achieving a given accuracy of the formfactor measurement. Suppose we wish to achieve a signal-to-noise ratio of 100. The number of independent measurements required to achieve this accuracy depends on the value of the formfactor at given frequency. Using eq. (5a) we find that the number of shots should be about 10^5 at the value of the formfactor about of unity. If the linear array detector covers, for instance, the frequency range of $10\Delta\omega_c$, one can perform ten independent measurements per one shot (per one radiation pulse). As a result, one can decrease the number of shots which is required for a given accuracy by a factor of ten. In this case, one macropulse of the TTF accelerator should be sufficient to obtain the required accuracy. This requires 10 MHz data acquisition system. One can use photomultipliers or pin-photodiodes as photodetectors. In this case the light from the monochromator exit can be distributed to photomultipliers (or photodiodes) by means of optical fibers.

References

[1] "Conceptual Design of a 500 GeV e+e− Linear Collider with Integrated X-ray Laser Facility" (Editors R.Brinkmann, G. Materlik, J. Rossbach, A. Wagner), DESY 97-048, Hamburg, 1997.

[2] "Zeroth-Order Design Report for the Next Linear Collider", LBNL-PUB-5424,SLAC Report 474, UCRL-ID-124161 (May 1996).

[3] Status reports on CLIC, JLC and VLEPP are given in: Proceedings of the LC'92 ECFA Workshop on e^+e^- Linear Colliders (July,25-August,2,1993,Germany), MPI-PhE/93-14, ECFA 93-154.

[4] R. Tatchyn et. al., Nucl. Instr. and Methods **A375**(1996)274.

[5] J. Rossbach, Nucl. Instr. and Methods **A375**(1996)269.

[6] M.S. Zolotorev and G.V. Stupakov, "Fluctuational Interferometry for Measurement of Short Pulses of Incoherent Radiation", SLAC-PUB-7132, March 1996.

[7] J. Goodman, Statistical Optics, (John Willey and Sons, New York, 1985).

[8] J. Krzywinski, E.L. Saldin, E.A. Schneidmiller and M.V. Yurkov, "A new method for Ultrashort Electron Pulse -shape Measurements Using Synchrotron Radiation from a Bending Magnet," Nucl. Instr. and Methods **A**, in press.

Magnetic measurements on the undulator prototype for the VUV - FEL at the TESLA Test Facility

J. Pflüger, H. Lu, [1] D. Köster, T. Teichmann

Hamburger Synchrotronstrahlungslabor HASYLAB at Deutsches Elektronen-Synchrotron DESY Notkestr85, 22603 Hamburg

Abstract

For the VUV - FEL at the TESLA Test Facility a 30 m long combined function undulator is under construction which integrates an alternating sequence of focusing and defocusing quadrupoles (FODO lattice) with an sinusoidally varying undulator field having a period length of 27.3 mm.

A planar magnet structure with a fixed gap using permanent magnet technology has been proposed. A brief description of the magnetic design and its basic working principle is given.

First results of magnetic measurements were performed on a 0.9 m long prototype structure and are reported and discussed in this contribution. The peak field , the gradient of the superimposed quadrupolar field as well as the adjustability of the quadrupole strength and the exact location of its axis in horizontal and vertical direction were measured. The results demonstrate that the proposed combined function magnet structure is very promising for the use in the SASE FEL at the TESLA Test Facility.

1 Undulator Design

At DESY in Hamburg a Free Electron Laser (FEL) for the VUV spectral range down to 6.4nm using the principle of Self Amplified Spontaneous Emission (SASE) [1,2] is under construction. It will use the electron beam of the TESLA Test Facility (TTF) [3,4] and will be built in two stages:

Phase 1 will have a nominal energy of up to 300 MeV which the potential of going up to 390 MeV. It will serve as a system test for the superconducting accelerator and a proof of principle for the SASE FEL. In this case an undulator

[1] on leave from : FEL Laboratory at Institute for High Energy Physics (IHEP) P.O. Box 2732 Beijing 100080 P.R. China

TESLA FEL-Report 1997-06

Table 1
Parameters for Phase 1 and 2 of the TTF

		Phase 1	Phase 2
Energy	[GeV]	0.3	1.0
normalized Emittance	[mm mrad]	2	2
Energy spread	[%]	0.17	0.1
Bunch length	[μm]	250	50
Peak current	[A]	500	2500
Radiative wavelength	[nm]	72	6.4
Saturation length	[m]	14	25
Saturation Power	[GW]	0.2	3.0

with a minimum length of 14.33 m is required. A detailed description of Phase 1 can be found in [5]. In Phase 2 see ref. [3], the energy will be raised to 1 GeV and the undulator needs to be extended to at least 28.7 m. For practical reasons it has to be subdivided into modules of about 4.5m length which can be handled and manufactured with the required accuracy. There have to be gaps between undulator sections of about 0.3m for beam position monitors and other diagnostic equipment as well as pumping ports etc. The undulator design for Phase 1 and 2 is kept as identical as possible. Table 1 shows some basic parameters of the TTF in Phase 1 and 2. Table 2 specifies the design parameters of the undulator.

The combined function undulator which is needed for the FEL has to integrate two functions:
(i) It has to provide the sinusoidal field so that the FEL process can take place.
(ii) It simultaneously has to provide the alternating gradient field of about $\pm$ 20 T/m for the FODO lattice which is superimposed to the undulator field.

For the small β-function values required for the TTF-FEL (see table 2) there is no alternative to a combined function type undulator. Permanent magnet (PM) technology using state of the art NdFeB magnet material has been chosen for the undulator [6-9]. Fig 1 shows a schematic 3-D view of $1\frac{1}{2}$ periods of the "Four Magnet Focusing Undulator" (4MFU) design which has been proposed to be used for the FEL at the TTF. It is based on a regular Halbach type hybrid structure [10]. There is no gap variation. The gap between the poles is kept fixed at 12mm. To finetune the undulator field the exact strength of each pole can be changed by slightly adjusting each pole tip individually by a few tenths of a millimeter. The magnets between the poles, which are magnetized parallel and antiparallel to the beam axis are recessed by 2.5mm to

Table 2
Undulator and FODO Parameters for Phase 1 and 2

Gap	[mm]	12	
Period Length	[mm]	27.3	
Undulator Peak Field	[T]	0.5	
K - Parameter		1.27	
Design Gradient	[T/m]	18.3	
Number of poles per module		327	
Total length per module	[mm]	4492.2	
Length of FODO quad section	[mm]	136.5	
FODO Period Length	[m]	0.9555	
Number of FODO periods per module		5	
Separation between Undulator Modules	[m]	0.2853	
		Phase 1	Phase 2
Number of undulator modules		3	6
Total length	[m]	14.33	28.67
Focal strength of FODO quads	[m^{-1}]	2.50	0.75
Total natural undulator focal strength	[m^{-1}]	1.788	0.322
Phase advance per FODO cell	[Deg]	52	18
β_{Max} in Undulator	[m]	1.5	3.5
β_{Min} in Undulator	[m]	0.5	2.5
Ave. Beamsize in Undulator	[μm]	55	55

create space for the magnets providing the focusing. These magnets are magnetized parallel / antiparallel to the Y-axis as can be seen in Fig. 1. They can be moved horizontally by set screws. By changing the horizontal separation distance between these magnets in the top and bottom jaw simultaneously the gradient can be changed. Moving all magnets horizontally the horizontal position of the quadrupole axis can be changed accordingly. Increasing / decreasing the separation distance in the top and decreasing / increasing it in the bottom jaw will move the position of the quadrupole axis down or up, respectively. Using geometrical arguments it can be shown that on the quadrupole axis the field generated by the symmetric undulator part is not influenced by the antisymmetric array of focusing magnets and its strength. This was also verified with 3-D calculations using the MAFIA code [6,9]. The 4MFU design therefore combines the following properties:

(i) It is a completely planar structure, which allows for very good access to

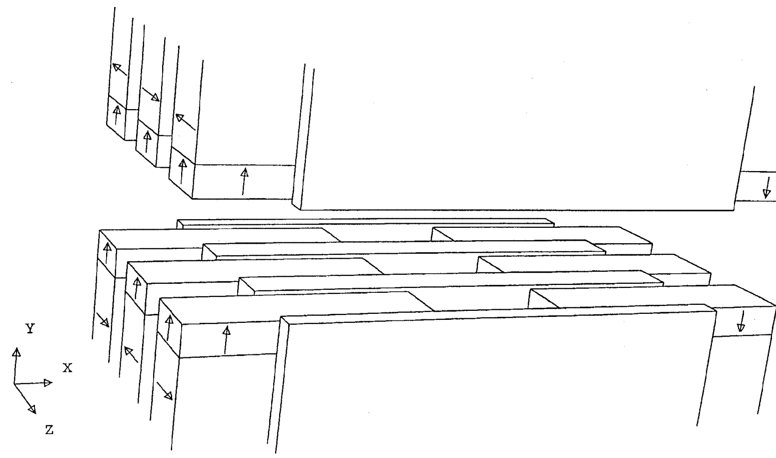

Fig. 1. 3-D perspective view of $1\frac{1}{2}$ periods of the proposed 4MFU structure for the undulator for the TTF. For details see text.

the field region at the beam position allowing for high accuracy field measurements as well as an easy installation of the vacuum chamber without breaking of any magnetic circuits.

(ii) The gradient can be as large as ≈20 T/m.

(iii) The exact value and the precise location of the quadrupole axis is fine tunable.

(iv) Undulator and focusing fields are decoupled. This means that on the quadrupole axis the sign and magnitude of the field gradient has no influence on the undulator field and vice versa.

For these properties the 4MFU principle was chosen as the basis of the undulator setup for the TTF.

2 Prototype Structure

A 0.9m long Prototype structure of this undulator has been built. It is shown in Fig. 2.

In order to reduce design and construction effort, the mechanical support system as well as the girders were already designed for one 4.5m long undulator module for the TTF. Each undulator is planned to consist of 5 magnetic segments of approximately 0.9m each. One of these segments was built and is used for the prototype structure. It is visible at the left end of the stucture. Roughly in the middle of this module the focusing magnet attachment is visible. All components in this prototype structure will later be reused to complete the first 4.5m long undulator module for the Phase 1 undulator.

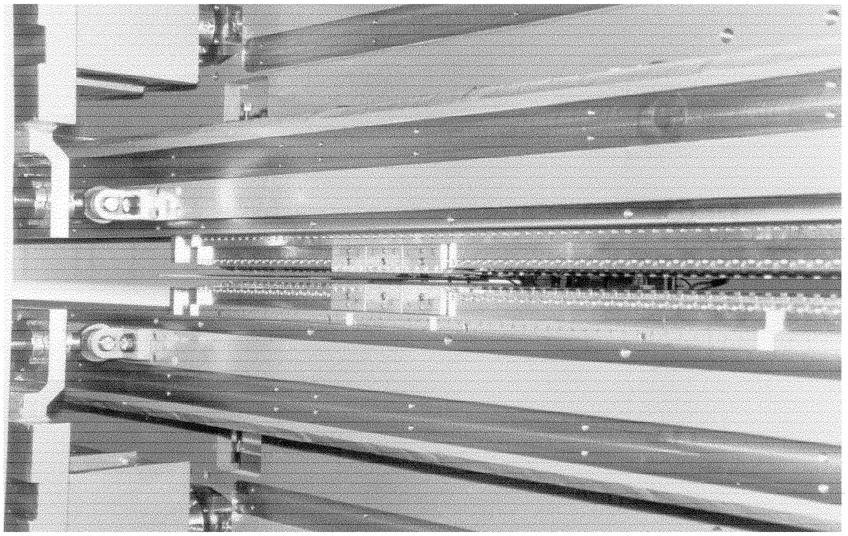

Fig. 2. View of the 0.9m long prototype structure of the 4MFU. One magnetic segment mounted on the left side of the 4.5m long girders designed for the FEL undulator is visible. The focusing section is about in the center of this segment.

3 Magnetic measurements

A new 12m long bench was used to characterize the magnetic performance of the prototype structure. It provides sufficient mechanical accuracy for the magnetic measurements of the combined function undulator for the FEL at the TTF.

Hallprobe measurements using a transverse probe were used to check the quality of the field and to exactly adjust the end poles for field integral correction right before the focusing magnets were installed. This "naked" undulator served as a basis for the following attachment of the focusing magnets.

In order to test the quality as a combined function undulator the focusing strength and the exact location of the quadrupole axis of each quadrupole section was to be measured. The Rectangular Coil Method (RCM) was developed for this purpose and is briefly described: A rectangular coil with a length along the beam axis much longer than that of a quad section is used. At TTF the length of one quad section is 136.5mm and that of a focusing free section is 341.25mm. So this condition can be easily satisfied.

The cross talk resulting from the undulator field can be minimized by choosing the coil length to be a multiple of a period length. we used 327.6mm, which corresponds to 12 periods at a length of the focusing section of 136.5mm. In addition measurements should be averaged over one undulator period. The transverse width of the coil has to be large enough so that the ends are in field free region. 330mm were found sufficient in our case.

If this coil is moved transversely in the horizontal plane along z, starting at z_a of quadrupole having its center at z_0 the flux change $\Delta\Phi$ induced in this coil is given by:

$$\Delta\Phi = N \cdot L \cdot \int_{z_a}^{z} B_y(z') \cdot dz' = N \cdot L \cdot g \cdot \int_{z_a}^{z} (z' - z_0) \cdot dz'$$

$$= N \cdot L \cdot g \cdot \tfrac{1}{2}((z - z_0)^2 - (z_a - z_0)^2)$$

here N is the number of windings of the coil , L is the effective quadrupole length and g is the gradient. The flux is recorded with an analog integrator at equidistant intervalls of z. By fitting a parabola of the form :

$$\Delta\Phi = a \cdot z^2 + b \cdot z + c$$

to the data, the integrated gradient can be evaluated :

$$g \cdot L = 2 \cdot a/N$$

The horizontal center position is given by:

$$z_0 = -b/N \cdot L \cdot g = -b/(2 \cdot a).$$

Analogous results for the vertical (y) direction are obtained if the coil is moved vertically instead of horizontally. In this case $B_y(z)$ has to be replaced by :

$$B_z(y) = -g \cdot (y - y_0)$$

We note that the coefficients of the higher order normal multipoles can be evaluated as well if an appropriate polynomial is fitted. First experience made with this measurement technique shows that a typical reproducibility of 7-8 μm RMS for the quadrupole centers in the horizontal and vertical direction is achievable, so far without any optimization effort. The gradient dertermined in this way was reproducible to 0.5 % RMS.

4 Results and discussion

The objective of the prototype stucture was to test if a combined function undulator following the proposed 4MFU design is doable and suitable for the use in the FEL at the TTF . The most interesting problem was to see how the array of focusing magnets behaves on top of the undulator stucture. First, the "naked" undulator with no focusing magnets attached was measured to have a peak field of almost exactly 0.5T. After this measurement one quadrupolar section was installed and the RCM method descibed above was used to

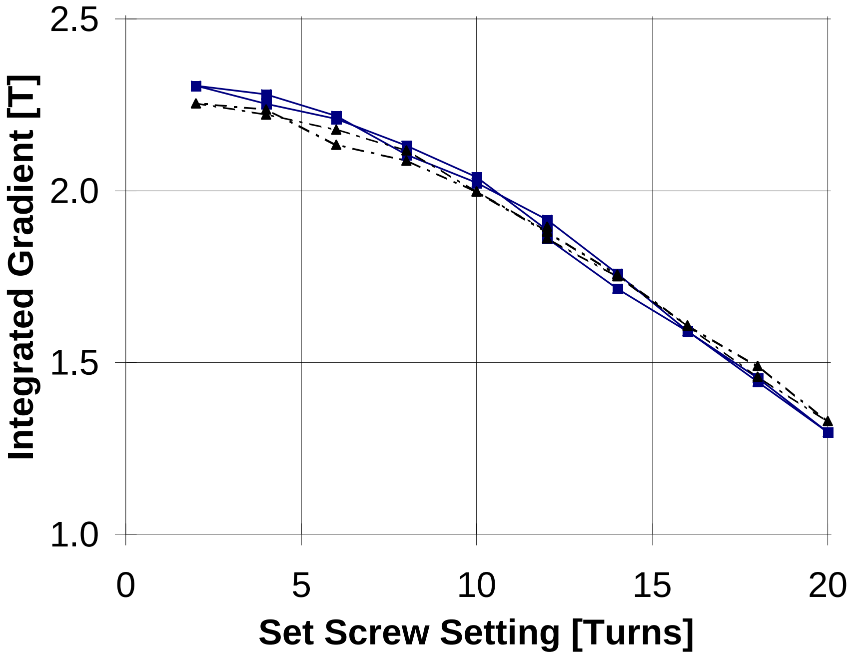

Fig. 3. Integrated Gradient obtained with RC Method. Full Line from Vertical, dot dashed horizontal movement. Set screw pitch is 0.7mm / Turn

measure the properties of this section. Fig. 3 shows the maximum integrated gradient gL as a function of the separation distance of the magnets. Several measurements were taken at identical settings and are hard to distinguish in Fig. 3. The separation distance is most practically measured counting the turns of the set screws which have a 0.7mm pitch. The two curves in Fig. 3 correspond to measurements using vertical and horizontal movement of the coil, i. e. gL is determined independently from B_y and B_z variation They agree better than 1.6%. The small deviation is believed to be due to the artefacts from the superimposed undulator field.

The zero in Fig. 3 corresponds to zero separation distance. It can be seen that it can nicely be adjusted from 2.3 T down to about 1.3 T using the adjustment range of the screws of 20 turns corresponding to 14mm. Using the length of the quadrupole section of 0.1365m as an effective length the maximum average quadrupole gradient is evaluated to 16.85 T/m .

Fig. 4 shows the measured horizontal position of the quadrupole center if all focusing magnets are moved simultaneously. The center is moving at a rate corresponding to the pitch of the set screws. The total range is ± 2.5 mm in this case and can be made larger if required. Note, the zero position shown in Fig. 4 on the vertical axis is arbitrary and does not correspond to the center of the undulator structure.

Fig. 5 finally shows two measurements of the movement of the vertical center. Vertical upward movement can be achieved if the separation distance of the

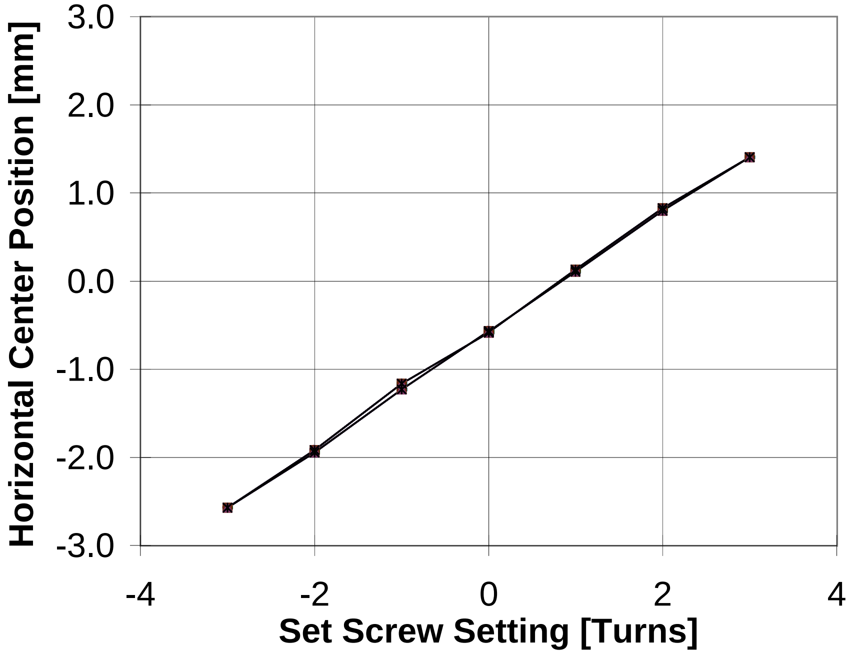

Fig. 4. Horizontal center position as a function of set screw position

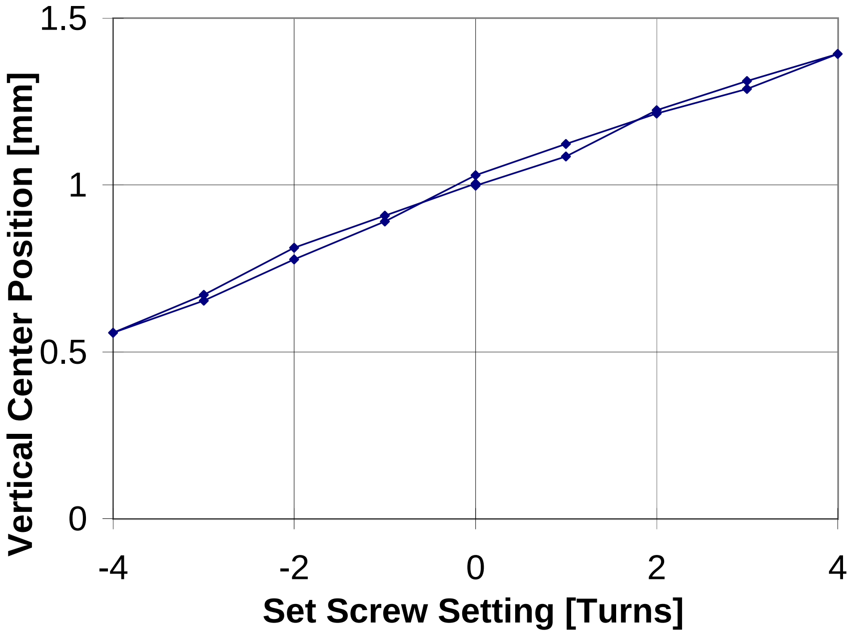

Fig. 5. Vertical center position as a function of set screw position.

upper magnets is increased while that of the lower magnets is decreased. The adjustment range is small, only ± 0.4mm, but still sufficient. Again the vertical zero position does not correspond to the zero position of the undulator structure.

The cross talk between the adjustments is small. For example if the vertical center position is changed only minor changes are observed in the horizontal

Table 3
Results of magnetic measurements on the prototype structure

Undulator Peak Field	[T]	0.5
Max. average Gradient @ Separation=0	[T/m]	16.93
Gradient Variation	[T]	1.3 - 2.3
Vertical center adjustment range	[mm]	$\pm$0.4
Horizontal center adjustment range	[mm]	$\pm$ 2.5
Integrated normal Quadrupole @ 4.2mm	[T]	2.078$\pm$0.069
Integrated normal Sextupole —"—	[T/m]	70.6$\pm$69.1
Integrated normal Octupole —"—	[T/m^2]	22856$\pm$151015

center position and the magnitude of the gradient. Moreover such changes can be easiliy adjusted by slight changes in a second iteration step if needed.

The adjustability demonstrated above is very important for a combined function undulator. Extended computer simulations have demonstrated that the overlap between electron and laser beam can only be guaranteed if the alignment of the quadrupole axes is about 10-15 μm [11,12]. So all ten FODO quads of an undulator module have to be aligned with this precision. In this contribution it has been shown that both, the adjustability and a measurement procedure, the RCM which provides sufficient accuracy are readily available.

Table 3 reproduces some of the magnetic results for this structure. The first normal multipole coefficients were also determined in the good field region near the electron beam Because this region extends to only $\pm$ 2mm, the uncertainty at the higher multipoles is rather large.

References

[1] A. M. Kondratenko, E. L. Saldin, Part. Accel. 10 (1980), 207.

[2] R. Bonifacio, C. Pellegrini, L. Narducci, Opt. Comm. 50 (1984), 373.

[3] "A VUV Free Electron Laser at the TESLA Test Facility at DESY, Conceptual Design Report" TESLA-FEL Report 95-03, DESY, Hamburg, April 1995.

[4] "Tesla Test Facility Linac Design Report" Editor :D. A. Edward , TESLA Report 95-01, Hamburg, March 1995.

[5] W. Brefeld, B. Faatz, Y. M. Nikitina, J. Pflüger , J. Roßbach, E.L. Saldin, E.A. Schneidmiller, M. V. Yurkov Proceedings of the FEL96 Conference August 26-31, 1996 Rome, Italy.

[6] Y. M. Nikitina, J. Pflüger, Nucl. Instr. and Methods A375 (1996), 325.

[7] J. Pflüger, Y. M. Nikitina, TESLA - FEL 96-02, 1996.

[8] Y. M. Nikitina, J. Pflüger, TESLA - FEL 96-03, 1996.

[9] J. Pflüger, Y. M. Nikitina, Nucl. Instr. and Methods A381 (1996) 554.

[10] K. Halbach, Journal de Physique, C1, suppl.2 , (1983) C1-211.

[11] B. Faatz, J. Pflüger, P. Pierini Nucl. Instr. and Methods A375 (1996), 441.

[12] B. Faatz, J. Pflüger, Y. Nikitina, Proceedings of the FEL96 Conference, August 26-31, 1996 Rome, Italy.

Numerical Study of Performance Limitations of X-ray Free Electron Laser Operation due to Quantum Fluctuation of Undulator Radiation

S. Reiche[a], E.L. Saldin[b], E.A. Schneidmiller[b], M.V. Yurkov[c]

[a] *Deutsches Elektronen Synchrotron, 22607 Hamburg, Germany*
[b] *Automatic Systems Corporation, 443050 Samara, Russia*
[c] *Joint Institute for Nuclear Research, Dubna, 141980 Moscow Region, Russia*

Abstract

One of the fundamental limitations towards achieving very short wavelength in a self amplified spontaneous emission free electron laser (SASE FEL) is connected with the energy diffusion in the electron beam due to quantum fluctuations of undulator radiation. Parameters of the LCLS and TESLA X-ray FEL projects are very close to this limit and there exists necessity in upgrading FEL simulation codes for optimization of SASE FEL for operation at a shortest possible wavelength. In this report we describe a one-dimensional FEL simulation code taking into account the effects of incoherent undulator radiation. Using similarity techniques we have calculated universal functions describing degradation of the FEL process due to quantum fluctuations of undulator radiation.

1 Introduction

It has been realized more than ten years ago that single-pass free electron laser (FEL) can provide the possibility to generate powerful, coherent VUV and X-ray radiation [1–3]. Several projects of such FEL amplifiers are under development at present [4–6].

When designing an FEL amplifier operating at the wavelength around 1 Å one should also take into account the effect of energy diffusion in the electron beam due to quantum fluctuations of undulator radiation. Recent study of performance limitations of an X-ray free electron laser has shown that this

TESLA FEL-Report 1997-06

effect leads to the growth of the energy spread in the electron beam, $\sigma_{\rm E}$, when the electron beam passes the undulator. This effect imposes fundamental limit towards achieving very short wavelength given by the following estimation [7] (for the case of zero energy spread at the undulator entrance):

$$\lambda_{\rm min} \simeq 45\pi \left[\lambda\!\!\!^{-}_{\rm c} r_{\rm e} \right]^{1/5} L_{\rm w}^{-7/15} \left[\epsilon_n^2 \frac{I_{\rm A}}{I} \right]^{8/15} , \qquad (1)$$

or, to a good approximation

$$\lambda_{\rm min}[\mathring{A}] \simeq 4 \frac{\pi \epsilon_n [\rm mm \ mrad]}{\sqrt{I[\rm kA] L_{\rm w}[\rm m]}} ,$$

where $\lambda\!\!\!^{-}_{\rm c} = \hbar / mc$, $\hbar$ is Planck constant, $r_{\rm e} = e^2 / m_{\rm e} c^2$, $(-e)$ and $m_{\rm e}$ are the charge and the mass of the electron, respectively, c is the spead of light, $I_{\rm A} \simeq 17$ kA is Alfven's current, $L_{\rm w}$ is the length of the undulator, $\epsilon_n = \gamma\epsilon$ is normalized emittance, and γ is the relativistic Lorentz factor.

All the existent FEL simulation codes do not take into account the effect of the energy diffusion in the electron beam due to quantum fluctuations of undulator radiation. On the other hand, design parameters of existent projects of X-ray FELs (LCLS at SLAC [5] and X-ray FEL at linear collider TESLA [6]) are very close to this limit and there exists an urgent necessity in more rigorous simulations of their parameters.

In this report we describe a one-dimensional FEL simulation code taking into account the effects of incoherent undulator radiation. Using similarity techniques we have calculated universal functions describing degradation of the FEL process due to quantum fluctuations of undulator radiation.

2 Numerical simulation algorithm

In this section we present brief description of the one-dimensional simulation code upgraded with the equations including the effects of incoherent undulator radiation. The self-consistent FEL equations are identical to those described in paper [8] (section 3). To describe the influence of incoherent undulator radiation on the FEL process we have included two physical effects into the FEL code. The first one is additional energy loss which is given by well known classical expression:

$$\mathrm{d} < \mathcal{E} > /\mathrm{d}z = -2r_{\mathrm{e}}^2\gamma^2 H_{\mathrm{w}}^2(z)/3 \ , \tag{2}$$

where H_{w} is the magnetic field of the undulator on axis.

Another effect is energy diffusion in the electron beam due to quantum fluctuations of the undulator radiation. The rate of energy diffusion is given by the expression:

$$\frac{\mathrm{d} < (\delta\mathcal{E})^2 >}{\mathrm{d}t} = \int \mathrm{d}\omega\hbar\omega\frac{\mathrm{d}I}{\mathrm{d}\omega} \ , \tag{3}$$

where $\mathrm{d}I/\mathrm{d}\omega$ is the spectral intensity of an undulator radiation. Explicit expression for the rate of the energy diffusion has the following form [9]:

$$\frac{\mathrm{d} < (\delta\gamma)^2 >}{\mathrm{d}t} = \frac{14}{15}c\lambda\!\!\!^{-}_{\mathrm{c}} r_{\mathrm{e}}\gamma^4\kappa_{\mathrm{w}}^3 K^2 F(K) \ , \tag{4}$$

where $\kappa_{\mathrm{w}} = 2\pi/\lambda_{\mathrm{w}}$, λ_{w} is the undulator period length, $K = eH_{\mathrm{w}}/m_{\mathrm{e}}c^2\kappa_{\mathrm{w}}$ is the dimensionless undulator parameter, and $F(K)$ is given by the following fitting formulae:

$$F(K) = 1.42K + \frac{1}{1 + 1.50K + 0.95K^2} \qquad \text{for helical undulator} \ , \tag{5a}$$

$$F(K) = 0.60K + \frac{1}{2 + 2.66K + 0.80K^2} \qquad \text{for planar undulator} \ . \tag{5b}$$

The simulation algorithm is organized as follows. Equations of motion of macroparticles and the field equations (see ref. [8], section 3) are integrated by means of Runge-Kutta scheme. An additional loss of the electron energy is calculated with eq. (2) and additional energy spread is introduced by means of random generator after each integration step in accordance with eq. (4). For the latter procedure to be physically correct, one should care about suppression of numerical noise connected with finite number of macroparticles. In other words, all the moments of the distribution function $f(\Psi, P, z)$ (here $P = \mathcal{E} - \mathcal{E}_0$):

$$a_k = \int P^k \exp(-\mathrm{i}\Psi) f(\Psi, P, z) \mathrm{d}P \mathrm{d}\Psi \ , \tag{6}$$

must have the same values before and after performing the procedure of introducing an additional energy spread. Otherwise, an additional (unphysical) bunching due to numerical noise will appear which will produce an error in the results of calculations. The necessity of compensation of the numerical noise can be explained in the following way. Suppose one has a problem to prepare an initial ensemble of the particles corresponding to unmodulated electron beam:

$$a_0(0) = \int \exp(-\mathrm{i}\Psi) f(\Psi, P, 0) \mathrm{d}P \mathrm{d}\Psi = 0 \ , \tag{7}$$

and some arbitrary distribution in the energy. Let us consider the evolution of such a distribution function $f(\Psi, P, z)$ in a drift space (no FEL process):

$$\frac{\mathrm{d}f(\Psi, P, z)}{\mathrm{d}z} - \alpha P f(\Psi, P, z) = 0 \ . \tag{8}$$

It follows from this equation that distribution functions at coordinates z and $z + \Delta z$ are connected by the relation:

$$f(\Psi, P, z + \Delta z) = f(\Psi, P, z) \exp(\alpha P \Delta z) \ . \tag{9}$$

Using eqs. (9) and (7) the evolution of the bunching factor a_0 is as follows:

$$a_0(z) = a_0(0) + \sum_{k=1}^{\infty} a_k \frac{\alpha^k}{k!} z^k \ . \tag{10}$$

It can been seen in eq. (10) that although starting with bunching factor $a_0(0) = 0$, bunching can occur if higher moments exist non equal to zero. In the presence of the FEL process this can introduce an error in the results of the calculation.

For the correction of the moments the phase space is divided up into N stripes with a limited range of the momentum ($P_{min} < P < P_{max}$), where the correction scheme is applied for each stripe. A larger number of stripes improves the results because a correlation between P and $\exp(-\mathrm{i}\Psi)$ is reduced. In general all higher moments, caused by the numerical noise, are reduced in the limit of $N \to \infty$. Numerical simulations show that for practical calculations it is sufficient to compensate only the first two moments of the distribution function, a_0 and a_1. In this case the accuracy of calculations is better than 1 % for $N = 150$ and 10000 macroparticles.

3 Simulation results

We consider simplified situation of a "cold" electron beam at the undulator entrance and neglect the influence of the space charge field. It is assumed that the FEL amplifier is tuned to the resonance frequency. Under these approximations operation of the conventional FEL amplifier is described in terms of the gain parameter Γ and the efficiency parameter ρ (see, e.g. refs. [2,8,10]):

$$\Gamma = \left[\frac{2\pi^2 j_0 K^2}{I_{\mathrm{A}}\lambda_{\mathrm{w}}\gamma^3}\right]^{1/3}, \qquad \rho = \frac{\lambda_{\mathrm{w}}\Gamma}{4\pi}, \tag{11}$$

where j_0 is the beam current density (for the case of a helical undulator).

We assume that the mean energy loss (see eq. (2)) are compensated by an appropriate undulator tapering and study pure effect of the energy diffusion in the electron beam due to quantum fluctuations of undulator radiation (see eq. (4)). When simulating SASE FEL with steady-state simulation code, one should set the value of the "effective" power of input shot noise which is given approximately by the relation [11,12]:

$$W_{\mathrm{sh}} \simeq \frac{3\sqrt{4\pi}\rho^2 P_{\mathrm{b}}}{N_\lambda \sqrt{\ln(N_\lambda/\rho)}} \ , \qquad (12)$$

where $P_{\mathrm{b}} = \gamma m_{\mathrm{e}} c^2 I/e$ is the power of the electron beam and $N_\lambda = I\lambda/(ec)$. For the case of the X-ray SASE FEL at TESLA [6] the value of the reduced input power is of about $\hat{W}_{\mathrm{sh}} = W_{\mathrm{sh}}/\rho P_{\mathrm{b}} \simeq 3 \times 10^{-7}$. This value has been used in the simulations.

Under accepted approximations the value of the reduced power at saturation, $\hat{\eta} = P_{\mathrm{out}}/\rho P_{\mathrm{b}}$, and the saturation length, $\hat{L}_{\mathrm{sat}} = L_{\mathrm{sat}}\Gamma$ are universal functions of the reduced input power $\hat{W}_{\mathrm{sh}}$ and the parameter of quantum fluctuations $\hat{q}$ (see eq. (4)):

$$\hat{q} = \frac{7}{15} \frac{\lambda\!\!\!^{-}_{\mathrm{c}} r_{\mathrm{e}}}{\rho^3} \gamma^2 k_{\mathrm{w}}^2 K^2 F(K) \ . \qquad (13)$$

Fig. 1 presents the plots of these universal functions in dependency of $\hat{q}$ for four diffferent settings of the reduced input power $\hat{W}_{\mathrm{sh}}$. It is seen that operation of the FEL amplifier degrades significantly when the value of the parameter of quantum fluctuations is increased.

Operating point of 1 Å FEL at TESLA (50 GeV energy of the electron beam [6]) corresponds to the value of the parameter of quantum fluctuations $\hat{q} = 9 \times 10^{-3}$. Fig. 2 illustrate the degradation of the FEL performance of the 1 ÅFEL at TESLA. It is seen that parameters of the project have been chosen correctly and there is only a slight degradation of the FEL performance due to quantum fluctuations of undulator radiation.

References

[1] Derbenev, Y.S., Kondratenko, A.M., and Saldin, E.L., *Nucl. Instrum. and Methods* **193** (1982) 415.

[2] Bonifacio, R., Pellegrini, C., and Narducci, L., *Opt. Commun.* **50** (1984) 373.

[3] Murphy, J.B., and Pellegrini, C., *Nucl. Instrum. and Methods* **A237** (1985) 159.

[4] "A VUV Free Electron Laser at the TESLA Test Facility: Conceptual Design Report", *DESY Print TESLA-FEL 95-03*, Hamburg, DESY, (1995).

[5] Tatchyn, R., et al., *Nucl. Instrum. and Methods* **A375** (1996) 274.

[6] Linear Collider Conceptual Design Report, *DESY print 97-048*, Hamburg, DESY, (1997).

[7] Rossbach, J., Saldin, E.L., Schneidmiller, E.A., and Yurkov, M.V., *Nucl. Instrum. and Methods* **A374** (1996) 401.

[8] Saldin, E.L., Schneidmiller, E.A., and Yurkov, M.V., *Phys. Rep.* **260** (1995) 187.

[9] Saldin, E.L., Schneidmiller, E.A., and Yurkov, M.V. *Nucl. Instrum. and Methods* **A381** (1996) 545.

[10] Bonifacio, R., et al., *Riv. Nuovo Cimento*, Vol.13, No.9 (1990).

[11] Kim, K.J., *Phys. Rev. Lett.* **57** (1986) 1871.

[12] Saldin, E.L., Schneidmiller, E.A., and Yurkov, M.V., *DESY Print TESLA-FEL 96-07*, Hamburg, DESY, (1996).

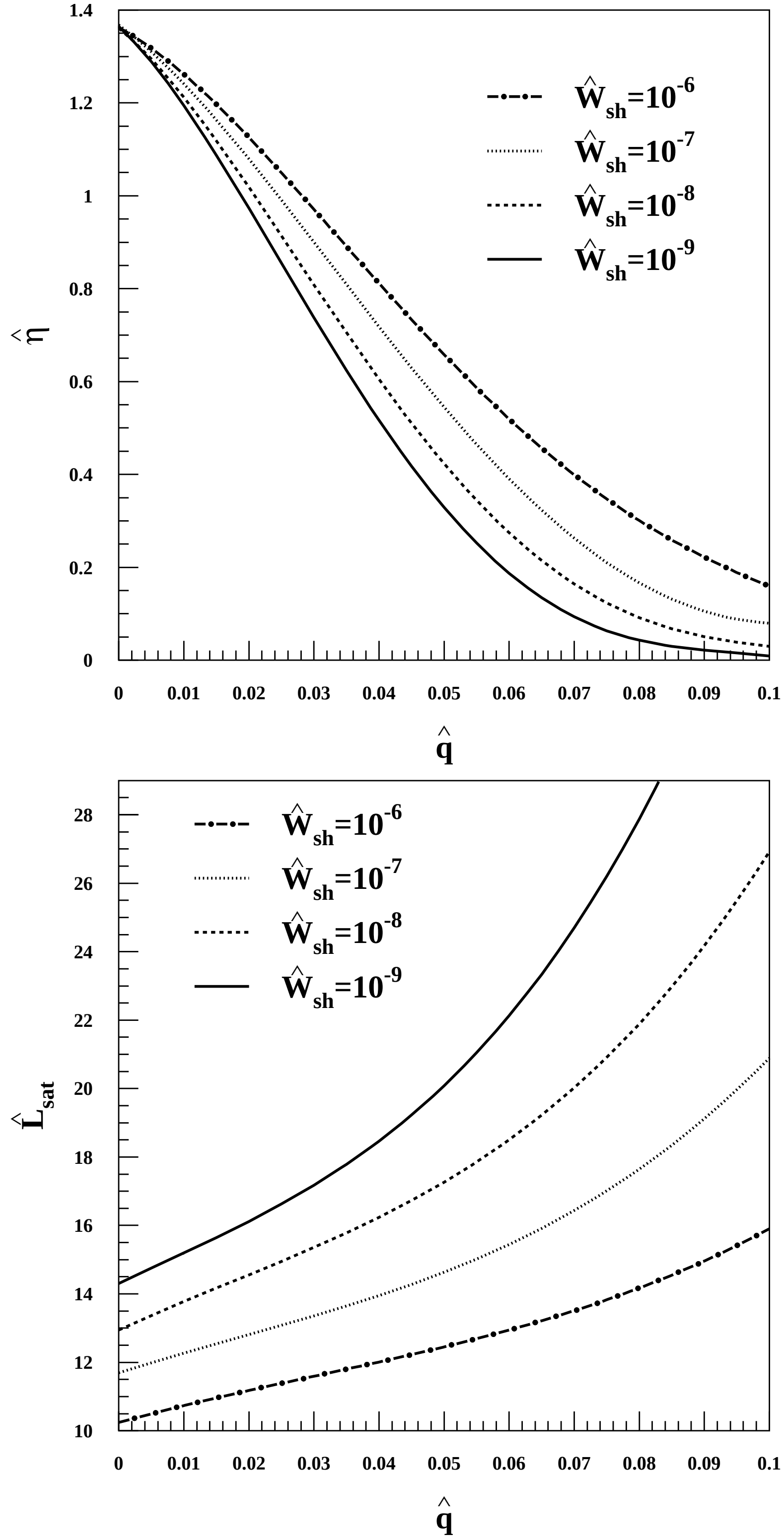

Fig. 1. Dependency of the saturation efficiency $\hat{\eta} = P_{\mathrm{out}}/\rho P_{\mathrm{b}}$ and saturation length $\hat{L}_{\mathrm{sat}} = L_{\mathrm{sat}}\Gamma$ on the value of the parameter of quantum fluctuations $\hat{q}$ and reduced input power $\hat{W}_{\mathrm{sh}}$.

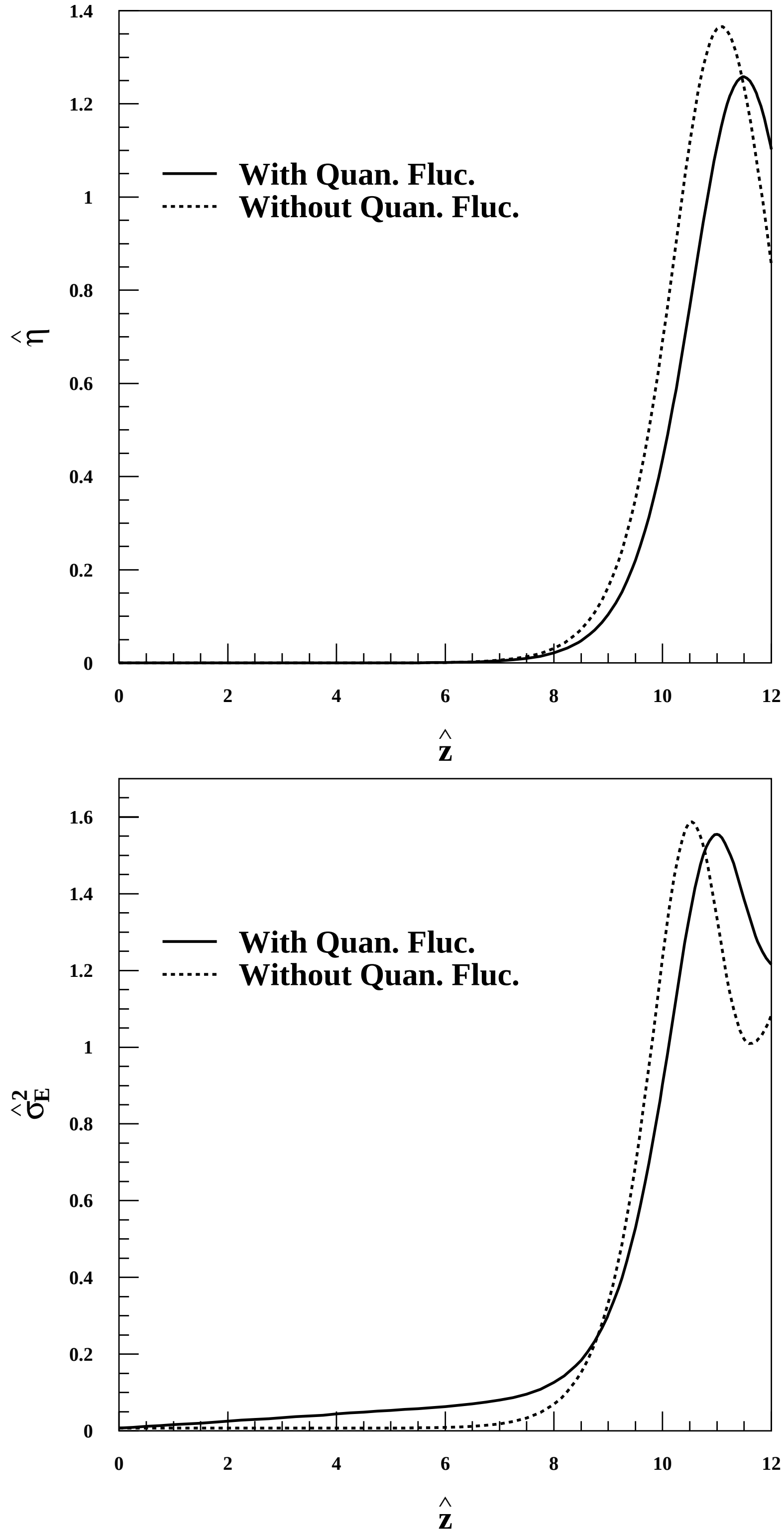

Fig. 2. Reduced efficiency $\hat{\eta} = P_{\mathrm{out}}/\rho P_{\mathrm{b}}$ and induced energy spread $\hat{\sigma}_E^2 = \langle \mathcal{E}^2 - \langle \mathcal{E} \rangle^2 \rangle / \rho^2 \langle \mathcal{E} \rangle^2$ for different position $\hat{z}$ in the TESLA 50 GeV FEL. Results including quantum fluctuations are drawn by a solid line ($\hat{q} = 9 \times 10^{-3}$), without – by a dashed line.

Analytical Treatment of the Radiative Interaction of Electrons in a Bunch Passing a Bending Magnet

E.L. Saldin[a], E.A. Schneidmiller[a], M.V. Yurkov[b]

[a] *Automatic Systems Corporation, 443050 Samara, Russia*

[b] *Joint Institute for Nuclear Research, Dubna, 141980 Moscow Region, Russia*

Abstract

The paper presents some analytical results of the theory of coherent synchrotron radiation (CSR) describing the case of finite curved track length.

1. Introduction

Analysis of project parameters of linear colliders [1, 2] and short-wavelength FELs [1, 3, 4] shows that the effects of coherent synchrotron radiation of short electron bunches passing bending magnets influence significantly on the beam dynamics (see, e.g., [5, 6]). The first investigations in the theory of coherent synchrotron have been performed about fifty years ago [7, 8, 9]. In these papers the main emphasis was put on the calculations in far zone of CSR produced by a bunch of relativistic electrons moving on a circular orbit. Another part of the problem, namely that of the radiative interaction of the electrons inside a bunch has been studied for the first time in refs. [10, 11] and later in refs. [5, 12] where the energy loss along the bunch has been calculated. The results of the above mentioned CSR theories are valid for a model situation of the motion of an electron bunch on a circular orbit and do not describe the case of an isolated bending magnet. The first analytical results describing this case have been presented in ref. [13]. In particular, analytical expressions have been obtained for the radiative interaction force, for the energy loss distribution along the bunch and for the total energy loss of the bunch. The criterium for the applicability region of the previous theories to the case of a finite magnet length has been derived. In this report some analytical results of ref. [13] are presented.

2. Results for a rectangular bunch

Let us consider a rectangular bunch of the length l_b passing a magnet with the bending angle ϕ_m and the bending radius R. We use the model of ultrarelativistic electron bunch with a linear distribution of the charge (zero transverse dimensions) and assume the bending angle to be small, $\phi_m \ll 1$. We neglect the interaction of the bunch with the chamber walls assuming the electrons to move in free space. The total number of particles in the bunch is equal to N and the linear density is equal to $\lambda = N/l_b$.

When the electron bunch passes the magnet, the electromagnetic field slips over the electrons due to the curvature and the difference between the electron's velocity and velocity of light c. The slippage length L_{sl} is given by the expression:

$$L_{sl} \simeq \frac{R\phi_m}{2\gamma^2} + \frac{R\phi_m^3}{24} , \qquad (1)$$

where γ is relativistic factor. When applying the results of steady-state CSR theory (periodical circular motion) to the case of isolated magnet it is assumed usually that the bunch length is much shorter than the slippage length. To obtain more correct criterium for the applicability region one has to develop more general theory including transient effects when the bunch enters and leaves the magnet. Such an investigation has been performed in ref. [13]. In particular, it has been stressed that the radiation formation length of the order of $l_b\gamma^2$ before and after magnet plays an important role in CSR effects. In practically

TESLA FEL-Report 1997-06

important case when the conditions $\gamma\phi_m \gg 1$ and $R/\gamma^3 \ll l_b < L_{sl}$ are satisfied, the expression for the total energy loss of the bunch can be written in the following form [13]:

$$\Delta\mathcal{E}_{tot} = -\left(\frac{3^{2/3}e^2N^2}{l_b^{4/3}R^{2/3}}\right)(R\phi_m) \times \left\{1 + \frac{3^{1/3}4}{9}\frac{l_b^{1/3}}{R^{1/3}\phi_m}\left[\ln\left(\frac{l_b\gamma^3}{R}\right) + C\right]\right\} \quad (2)$$

where e is the charge of the particle and

$$C = 2\ln 2 - \frac{1}{2}\ln 3 - \frac{11}{2} \simeq -4 \ .$$

The first term in eq. (2) is the solution obtained in the framework of steady-state approach (see, e.g., refs. [9, 11, 5]). Therefore, with logarithmical accuracy we can set the applicability region of the results of the steady-state theory for the case of a finite curved track length:

$$\frac{l_b^{1/3}}{R^{1/3}\phi_m}\ln\left(\frac{l_b\gamma^3}{R}\right) \ll 1 \ . \quad (3)$$

In particular, the steady-state theory provides completely incorrect results for the case of the electron bunch much longer than the slippage length, $l_b \gg L_{sl}$. In this case the energy losses of the particles in the bunch due to CSR are proportional to the local linear density and take place mainly after the magnet [13]. For a "short" magnet, $\gamma\phi_m \ll 1$, the total energy loss of rectangular bunch is equal to

$$\Delta\mathcal{E}_{tot} = -\frac{2}{3}\frac{e^2N^2}{l_b}\ \gamma^2\phi_m^2 \ . \quad (4)$$

The energy loss of the rectangular bunch passing a "long" magnet, $\gamma\phi_m \gg 1$, is equal to:

$$\Delta\mathcal{E}_{tot} = -\frac{N^2e^2}{l_b}\left[4\ln(\gamma\phi_m) - 2\right] \ . \quad (5)$$

These results has been obtained in ref. [13] by means of calculation the radiative interaction of the electrons in the bunch. It is interesting to compare the total energy loss of the bunch with the energy of coherent radiation in far zone. The radiation energy in far zone can be calculated as an integral over frequency of the spectral density of the radiation energy:

$$\frac{dW_{coh}}{d\omega} = N^2\eta(\omega)\frac{dW}{d\omega} \ , \quad (6)$$

where $\eta(\omega)$ is the bunch form factor (squared module of the Fourier transform of the linear density distribution). The form factor for the rectangular bunch of the length l_b is given by the expression:

$$\eta(\omega) = \left(\sin\frac{\omega l_b}{2c}\right)^2\left(\frac{\omega l_b}{2c}\right)^{-2} \ . \quad (7)$$

Function $dW/d\omega$ entering eq. (6) is the spectral density of the radiation energy of a single electron. The angular and the spectral characteristics of the radiation of an electron moving in an arc of a circle have been studied in ref. [14][1]. It has been shown that the spectrum of the radiation emitted by an electron moving in an arc of a circle differs significantly from that of conventional synchrotron radiation of an electron executing periodical circular motion. In the latter case the spectral density at low frequencies is proportional to $\omega^{1/3}$ [16]. In the case of a finite curved track length the spectral density is constant at $\omega \to 0$. When the bending angle is small, $\phi_m \ll 1$, the spectral density of the radiation energy emitted by ultrarelativistic electron is function of the only parameter $\gamma\phi_m$ [14]:

$$\frac{dW}{d\omega} = \frac{e^2}{\pi c}f_m \ , \quad (8)$$

where

$$f_m = \left(\mu + \frac{1}{\mu}\right)\ln\frac{1+\mu}{1-\mu} - 2 \ ,$$

and

$$\mu = \frac{\gamma\phi_m/2}{\sqrt{1+(\gamma\phi_m/2)^2}} \ .$$

Formula (8) is valid in the frequency range $\omega \ll c/L_{sl}$. Taking into account formula (7) we can estimate that typical frequencies of the coherent radiation are below the frequency $\omega \sim c/l_b$. It means that we can use the asymptotical expression (8) in the case when $l_b \gg L_{sl}$. Integrating eq. (6) over the frequency, we obtain:

$$W_{coh} = \frac{e^2N^2}{l_b}f_m \ . \quad (9)$$

It is easy to obtain that in the case of a "long" magnet, $\gamma\phi_m \gg 1$, the energy of coherent radiation (9) coincides exactly with the bunch energy loss given by eq. (5) taken with opposite sign. In the limit of a "short" magnet, $\gamma\phi_m \ll 1$, there is also complete agreement between formulae (9) and (4).

3. Bunch with an arbitrary density profile

The solutions obtained in ref. [13] for the rectangular bunch can be generalized for the case of an arbitrary linear charge density. We present here the results of the calculation of the transition process when the bunch enters the magnet. Let the bunch have the density distribution $\lambda(s)$ which satisfies the condition

$$\frac{R}{\gamma^3}\frac{d\lambda(s)}{ds} \ll \lambda(s) \ . \quad (10)$$

[1] The same problem has been considered later in ref.[15], but the results of this paper are incorrect.

Under this condition the rate of the energy change of an electron is given by the expression [13]:

$$\frac{d\mathcal{E}(s,\phi)}{d(ct)} = -\frac{2e^2}{3^{1/3}R^{2/3}}\left\{\left(\frac{24}{R\phi^3}\right)^{1/3}\left[\lambda\left(s-\frac{R\phi^3}{24}\right)- \lambda\left(s-\frac{R\phi^3}{6}\right)\right] + \int\limits_{s-R\phi^3/24}^{s}\frac{ds'}{(s-s')^{1/3}}\frac{d\lambda(s')}{ds'}\right\} , \qquad (11)$$

where s is the position of the electron in the bunch and ϕ is azimuthal angle.

For the Gaussian density distribution:

$$\lambda(s) = \frac{N}{(2\pi)^{1/2}\sigma}\, exp\left[-\frac{s^2}{2\sigma^2}\right] , \qquad (12)$$

expression (11) takes the form:

$$\frac{d\mathcal{E}}{d(ct)} = -\frac{2e^2 N}{3^{1/3}(2\pi)^{1/2}R^{2/3}\sigma^{4/3}}G(\xi,\rho) , \qquad (13)$$

where function $G(\xi,\rho)$ is given by the expression:

$$G(\xi,\rho) = \rho^{-1/3}\left[e^{-(\xi-\rho)^2/2} - e^{-(\xi-4\rho)^2/2}\right] + \int\limits_{\xi-\rho}^{\xi}\frac{d\xi'}{(\xi-\xi')^{1/3}}\frac{d}{d\xi'}e^{-(\xi')^2/2} . \qquad (14)$$

Here $\xi = s/\sigma$ and $\rho = R\phi^3/24\sigma$. Function $G(\xi,\rho)$ reduces to

$$G(\xi,\rho) \simeq -\frac{9}{2}\xi\exp(-\xi^2/2)\rho^{2/3}$$

at $\rho \ll 1$. In the opposite case, at $\rho \to \infty$, expression (14) tends to the steady-state solution [11, 5, 12]. In Fig.1 we present the plot of function (13). One can see that there is excellent agreement of analytical results [13] and the results obtained by means of numerical simulation code [6].

Acknowledgement

We wish to thank C.L. Bohn, R. Brinkmann, Ya.S. Derbenev, M. Dohlus, K. Floettmann, D. Jaroszynski, T. Limberg, H. Mais, A. Piwinski, J. Rossbach, V.D. Shiltsev and D. Trines for useful discussions.

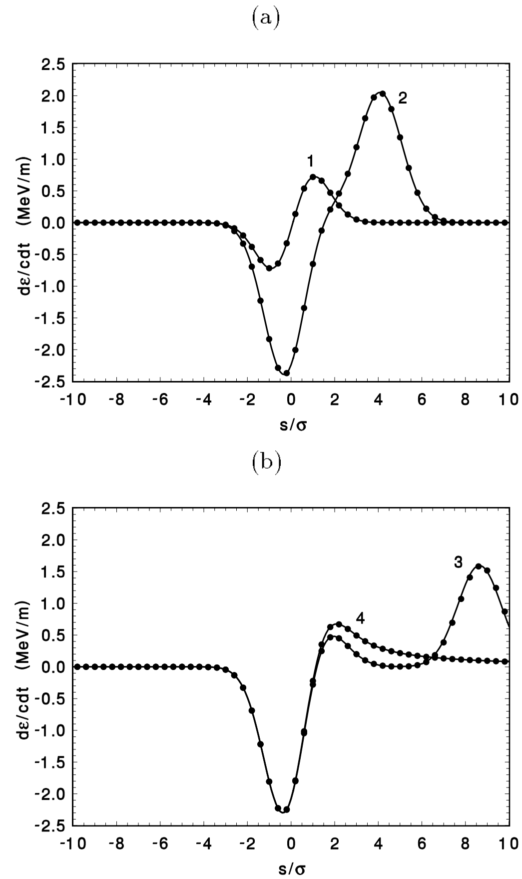

The rate of an electron energy change as a function of its position along the Gaussian bunch entering the magnet. Curve (1) in the graph (a): 5 cm after the begin of the magnet. Curve (2) in the graph (a): 14 cm after the begin of the magnet. Curve (3) in the graph (b): 18 cm after the begin of the magnet. Curve (4) in the graph (b): steady state. The curves are the results of calculations with formula (13) and the circles are the results of numerical simulations presented in ref. [6]. The parameters are as follows: $R = 1.5$ m, $\sigma = 50$ μm, $q = 1$ nC.

References

[1] "Conceptual Design of a 500 GeV e+e− Linear Collider with Integrated X-ray Laser Facility" (Editors R.Brinkmann, G. Materlik, J. Rossbach, A. Wagner), DESY 97-048, Hamburg, 1997.

[2] "Zeroth-Order Design Report for the Next Linear Collider", LBNL-PUB-5424,SLAC Report 474, UCRL-ID-124161 (May 1996).

[3] R. Tatchyn et al., Nucl. Instr. and Methods **A375**(1996)274.

[4] J. Rossbach, Nucl. Instr. and Methods **A375**(1996)269.

[5] Ya.S. Derbenev, J. Rossbach, E.L. Saldin, V.D. Shiltsev, "Microbunch Radiative Tail-Head Interaction", DESY Print, TESLA-FEL 95-05, Hamburg(1995).

[6] M. Dohlus, T. Limberg, "Emittance Growth due to Wake Fields on Curved Bunch Trajectories", presented at XVIII International Free Electron Laser Conference (Rome,1996); DESY print, TESLA-FEL 96-13 (1996).

[7] L.I. Schiff, Rev. Sci. Instr. **17**(1946)6.

[8] J. Schwinger, "On radiation by electrons in a betatron", 1945 (unpublished), see references in [9].

[9] J.S. Nodvick and D.S. Saxon, Phys. Rev. **96**(1954)180.

[10] I.E. Tamm, Report of the Institute of Physics, Acad. of Sciences, USSR, 1948 (in Russian).

[11] L.V. Iogansen and M.S. Rabinovich, Sov. Phys. JETP, vol.37(10), 1960, p.83.

[12] J.B. Murphy, S. Krinsky and R.L. Glukstern, "Longitudinal Wakefield for Synchrotron Radiation", Proc. of IEEE PAC 1995, Dallas(1995).

[13] E.L. Saldin, E.A. Schneidmiller, M.V. Yurkov, "On the Coherent Radiation of an Electron Bunch Moving in an Arc of a Circle", DESY Print, TESLA-FEL 96-14 (November 1996).

[14] V.G. Bagrov, I.M. Ternov and N.I. Fedosov, Sov. Phys. JETP, vol.55(5), 1982, p.835; Phys. Rev. **D28** (1983)2464.

[15] D.J. Wingham, Phys. Rev. **D35**(1987)2584.

[16] J. Schwinger, Phys. Rev. **75**(1949)1912.

Statistical properties of the radiation from SASE FEL operating in the linear regime

E.L. Saldin[a], E.A. Schneidmiller[a], M.V. Yurkov[b]

[a] *Automatic Systems Corporation, 443050 Samara, Russia*

[a] *Joint Institute for Nuclear Research, Dubna, 141980 Moscow Region, Russia*

Abstract

The paper presents analysis of statistical properties of the radiation from self amplified spontaneous emission (SASE) free electron laser operating in linear mode. The investigation has been performed in a one-dimensional approximation, assuming the electron pulse length to be much larger than a coherence length of the radiation. The following statistical properties of the SASE FEL radiation have been studied: field correlations, distribution of instantaneous power, distribution of the radiation energy after monochromator installed at the FEL amplifier exit and photoelectric counting statistics of SASE FEL radiation. It is shown that the radiation from SASE FEL operating in linear regime possesses all the features corresponding to completely chaotic polarized radiation.

1. Introduction

Correct design of the SASE FEL and planning of user's equipment and experiments depend strongly on knowledge of the radiation amplification process in the SASE FEL and properties of the output radiation. The process of amplification in the SASE FEL starts from the shot noise in the electron beam having stochastic nature. It means that the SASE FEL radiation is also stochastic object, that is why there exists definite problem for description of the SASE FEL process requiring development of time-dependent theory of the FEL amplifier. Some averaged output characteristics of SASE FEL have been obtained in refs. [1, 2, 3, 4, 5, 6, 7, 8]. Quantum consideration of photon statistics in SASE FEL has been performed in ref. [9, 10]. An approach for time-dependent numerical simulations of SASE FEL has been developed in ref. [8].

Nevertheless, the previous studies do not give comprehensive description of the output radiation from SASE FEL and the following statistical properties should studied in detail: field correlations, statistics of instantaneos power, statistics of the radiation energy after the monochromator installed at the exit of SASE FEL, photoelectric counting statistics of SASE FEL radiation etc. This paper gives answers on all the above mentioned problems describing statistical properties of the radiation from SASE FEL operating in linear regime. The investigation has been performed in a one-dimensional approximation. It is shown that the radiation from SASE FEL operating in the linear regime possesses all the features corresponding to completely chaotic polarized radiation. In particular, the higher order correlation functions are expressed via the first order correlation function and the probability density function of the energy after monochromator follows the gamma distribution.

2. Analysis of radiation properties in frequency domain

In the linear mode of operation the SASE FEL can be treated as a narrow band linear device which filters a wide band random input signal – shot noise. General property of such devices is that an output signal is a Gaussian random process. Since electron pulse at the entrance of SASE FEL has finite duration, we deal with nonstationary random process. Analytical study of such a process in general case is very complicated. Analysis of design parameters of VUV and X-ray SASE FELs shows that the feature of these devices is that the bunch length is much larger than the radiation coherence length. So, one can use the model

TESLA FEL-Report 1997-06

of rectangular profile of the electron bunch and the steady-state spectral Green's function. In the frame of this model it becomes possible to describe analytically all statistical properties of the radiation from SASE FEL operating in the high gain linear regime.

Let us consider microscopic picture of the electron beam current at the entrance into the undulator. The electron beam current is constituted by moving electrons randomly arriving to the entrance of the undulator:

$$I(t) = (-e) \sum_{k=1}^{N} \delta(t - t_k) \ ,$$

where $\delta(\dots)$ is delta-function, (-e) is the charge of the electron, N is the number of electrons in a bunch and t_k is random arrival time of the electron to the undulator entrance. The electron beam current $I(t)$ and its Fourier transform $\bar{I}(\omega)$ are connected by Fourier transformation:

$$\bar{I}(\omega) = \int\limits_{-\infty}^{\infty} e^{i\omega t} I(t) dt = (-e) \sum_{k=1}^{N} e^{i\omega t_k} \ ,$$

Let us calculate the correlation of $\bar{I}(\omega)$ and $\bar{I}(\omega')$:

$$\langle \bar{I}(\omega) \bar{I}^*(\omega') \rangle = e^2 \langle \sum_{k=1}^{N} \sum_{n=1}^{N} \exp(i\omega t_k - i\omega' t_n) \rangle \ .$$

Here $\langle \dots \rangle$ means the averaging over ensemble of bunches. The electron bunch profile is described by the profile function $F(t)$: $\langle I(t) \rangle = (-e) N F(t)$. Taking into account this relation we obtain that

$$\langle \exp(i\omega t_k) \rangle = \int\limits_{-\infty}^{\infty} F(t_k) e^{i\omega t_k} dt_k = \bar{F}(\omega) \ .$$

In the case when $N \mid \bar{F}(\omega) \mid^2 \ll 1$, we can write the following expressions:

$$\langle \bar{I}(\omega) \bar{I}^*(\omega') \rangle = e^2 N \bar{F}(\omega - \omega') \ , \qquad (1)$$

$$\begin{aligned} &\langle \mid \bar{I}(\omega) \mid^2 \mid \bar{I}(\omega') \mid^2 \rangle = \\ &\langle \mid \bar{I}(\omega) \mid^2 \rangle \langle \mid \bar{I}(\omega') \mid^2 \rangle + \mid \langle \bar{I}(\omega) \bar{I}^*(\omega') \rangle \mid^2 \ . \end{aligned} \qquad (2)$$

In the following we will analyze in detail the case of rectangular profile of the electron bunch. Transversely coherent fraction of the input shot noise signal is defined by the total beam current, so Fourier amplitude of the electric field at the exit of SASE FEL operating in the linear high-gain regime can be written as follows: $\bar{E}(\omega) = H_A(\omega - \omega_0) \bar{I}(\omega)$, where $H_A(\omega - \omega_0)$ is the Green's function and ω_0 is the resonance frequency. For many applications and for diagnostic measurements of SASE FEL radiation a monochromator with transmission function H_m will be installed at the FEL amplifier exit. In this case the expression for $\bar{E}(\omega)$ takes the form: $\bar{E}(\omega) = H_m(\omega - \omega_0) H_A(\omega - \omega_0) \bar{I}(\omega)$. Using eqs. (1) and (2) we obtain

$$g_1(\omega, \omega') = \frac{\langle \bar{E}(\omega) \bar{E}^*(\omega') \rangle}{\left[\langle \mid \bar{E}(\omega) \mid^2 \rangle \langle \mid \bar{E}(\omega') \mid^2 \rangle \right]^{1/2}} = \bar{F}(\omega - \omega') \ , \qquad (3)$$

$$g_2(\omega, \omega') = \frac{\langle \mid \bar{E}(\omega) \mid^2 \mid \bar{E}(\omega') \mid^2 \rangle}{\langle \mid \bar{E}(\omega) \mid^2 \rangle \langle \mid \bar{E}(\omega') \mid^2 \rangle} = 1 + \mid g_1(\omega, \omega') \mid^2 \ . \qquad (4)$$

We should note that eq. (4) is a property of a completely chaotic polarized radiation. It follows from this conclusion that $\mid \bar{E}(\omega) \mid^2$ is distributed in accordance with the negative exponential probability density function (see ref. [11] for more detail):

$$p(\mid \bar{E}(\omega) \mid^2) = \frac{1}{\langle \mid \bar{E}(\omega) \mid^2 \rangle} \exp\left(- \frac{\mid \bar{E}(\omega) \mid^2}{\langle \mid \bar{E}(\omega) \mid^2 \rangle} \right) \ . \qquad (5)$$

The next problem is description of the fluctuations of the radiation bunch energy W at a detector installed after a monochromator. From the expression for Pointing's vector and Parseval's theorem we can write the expression for the average energy measured by the detector:

$$\begin{aligned} \langle W \rangle &= \frac{cS}{4\pi^2} \int\limits_{0}^{\infty} \langle \mid \bar{E}(\omega) \mid^2 \rangle d\omega = \\ &\frac{ce^2 SN}{4\pi^2} \int\limits_{0}^{\infty} \mid H_m(\omega - \omega_0) \mid^2 \mid H_A(\omega - \omega_0) \mid^2 d\omega \end{aligned} \qquad (6)$$

where S is the transverse area of the detector. Taking into account relation (4) we can write the expression for normalized dispersion:

$$\sigma_W^2 = \frac{\langle (W - \langle W \rangle)^2 \rangle}{\langle W \rangle^2} = \frac{\int\limits_0^\infty d\omega \int\limits_0^\infty d\omega' \langle \mid \bar{E}(\omega) \mid^2 \rangle \langle \mid \bar{E}(\omega') \mid^2 \rangle \mid g_1(\omega', \omega') \mid^2}{\int\limits_0^\infty d\omega \langle \mid \bar{E}(\omega) \mid^2 \rangle \int\limits_0^\infty d\omega' \langle \mid \bar{E}(\omega') \mid^2 \rangle} \qquad (7)$$

Let us derive analytical expression for σ_W^2. In the framework of the one-dimensional model and when the effects of the space charge field and energy spread in the beam can be neglected, operation of the

FEL amplifier is described in terms of the gain parameter Γ and the efficiency parameter ρ (see, e.g. refs. [3, 12, 13]) which are connected by the relation $\rho = \lambda_{\mathrm{w}}\Gamma/4\pi$, where λ_{w} is the undulator period. Using expression for the solution of the initial-value problem in a high-gain limit we can write [1, 4, 6]:

$$\mid H_A \mid^2 = A \exp\left[-\frac{(\omega-\omega_0)^2}{2\sigma_A^2}\right] , \qquad \sigma_A = 3\sqrt{\frac{2}{\sqrt{3}}\frac{\rho\omega_0}{\sqrt{\hat{z}}}} . \tag{8}$$

Substituting expressions (8) into eq. (7) we obtain for the case of a Gaussian profile of the monochromator line $\mid H_m \mid^2 = \exp\left[-(\omega-\omega_0)^2/2\sigma_m^2\right]$:

$$\sigma_W^2 = \frac{\sqrt{\pi}}{\hat{\sigma}^2}\int\limits_0^{\hat{\sigma}} \mathrm{erf}(x) dx , \qquad \hat{\sigma} = \frac{\hat{\sigma}_A\hat{\sigma}_m}{\sqrt{\hat{\sigma}_A^2+\hat{\sigma}_m^2}} , \qquad \hat{\sigma}_m = \sigma_m T . \tag{9}$$

We assume pulse duration T to be large, $\sigma_A T \simeq \rho\omega_0 T \gg 1$. The value $\rho\omega_0 T$ is of the order of $10^2 \div 10^3$ for modern projects of VUV and X-ray SASE FELs, so the obtained result can be used for practical calculations.

The next practical problem is to find the probability density distribution of the radiation energy after monochromator, $p(W)$. Using arguments similar to that of ref. [11] one can show that the distribution of the radiation energy after the monochromator is described rather well by a gamma probability density function:

$$p(W) = \frac{M^M}{\Gamma(M)}\left(\frac{W}{\langle W\rangle}\right)^{M-1}\frac{1}{\langle W\rangle}\exp\left(-M\frac{W}{\langle W\rangle}\right) , \tag{10}$$

where $\Gamma(M)$ is gamma function and $M = 1/\sigma_W^2$. Parameter M can be interpreted as the average number of "degrees of freedom" or "modes" in a radiation pulse. It follows from eq. (7) that this parameter can not be less than unity. When M tends to unity, the distribution (10) tends to the negative exponential distribution (5). When $M \gg 1$, the distribution (10) tends to the Gaussian distribution.

3. Analysis of the radiation properties in time domain

Time dependence of the radiation field has the form $E(z,t) = \left[\tilde{E}(z,t)e^{-i\omega_0(z/c-t)} + C.C.\right]$ at any position along the undulator. The first and second order time correlation functions are defined as follows:

$$g_1(t-t') = \frac{\langle \tilde{E}(t)\tilde{E}^*(t')\rangle}{\left[\langle\mid \tilde{E}(t)\mid^2\rangle\langle\mid \tilde{E}(t')\mid^2\rangle\right]^{1/2}} . \tag{11}$$

$$g_2(t-t') = \frac{\langle\mid \tilde{E}(t)\mid^2\mid \tilde{E}(t')\mid^2\rangle}{\langle\mid \tilde{E}(t)\mid^2\rangle\langle\mid \tilde{E}(t')\mid^2\rangle} . \tag{12}$$

Using approximation $\rho\omega_0 T \gg 1$ and formulae (3), (4) we can write

$$g_1(t-t') = \frac{\int\limits_{-\infty}^{\infty} d(\Delta\omega) \mid H_A(\Delta\omega)\mid^2 \exp\left[-i\Delta\omega(t-t')\right]}{\int\limits_{-\infty}^{\infty} d(\Delta\omega) \mid H_A(\Delta\omega)\mid^2} , \tag{13}$$

$$g_2(t-t') = 1 + \mid g_1(t-t')\mid^2 . \tag{14}$$

The distribution of the instantaneous radiation power $P \propto \mid \tilde{E}\mid^2$ is the negative exponential distribution:

$$p(\mid \tilde{E}(t)\mid^2) = \frac{1}{\langle\mid \tilde{E}(t)\mid^2\rangle}\exp\left(-\frac{\mid \tilde{E}(t)\mid^2}{\langle\mid \tilde{E}(t)\mid^2\rangle}\right) , \tag{15}$$

and finite-time integrals of the instantaneous power follow the gamma distribution (10).
Substitution expression (8) into eq. (13) we obtain ($\tau = (t-t')$):

$$g_1(\tau) = \exp\left(-\frac{9\rho^2\omega_0^2\tau^2}{\sqrt{3}\hat{z}}\right) . \tag{16}$$

Following the approach of ref. [11], we define the coherence time τ_c as

$$\tau_c = \int\limits_{-\infty}^{\infty} \mid g_1(\tau)\mid^2 d\tau = \frac{\sqrt{\pi}}{\sigma_A} = \sqrt{\frac{\sqrt{3}\pi\hat{z}}{18}}\frac{1}{\rho\omega_0} . \tag{17}$$

Let us discuss the problem how to measure statistical properties of the SASE FEL radiation. Typical pulse duration of existent projects of SASE FELs is of about a fraction of picosecond. The resolution time of modern fast photoelectric detectors is much larger than this value, of about a fraction of nanosecond, which allows to measure total energy of the radiation pulse only. On the other hand, there are no such evident technical limitations for measurement of statistical properties of SASE FEL radiation in frequency domain.

4. Photoelectric Detection of SASE FEL Radiation

It has been shown above that the energy, W, in the radiation pulse reaching the photodetector is unpredictable, we can predict the probability density $p(W)$ only. In this case the probability of detection of K photons by a photodetector is given by [11]:

$$P(K) = \int_0^\infty \frac{(\alpha W)^K}{K!} \exp(-\alpha W) p(W) dW \ , \qquad (18)$$

where $\alpha = \eta/\hbar\omega_0$ and η is the quantum efficiency of the photodetector. Using formula (18) we get the expressions for the mean and for the variance of K value [11]:

$$\langle K \rangle = \alpha \langle W \rangle \ , \qquad \sigma_K^2 = \frac{\langle K^2 \rangle - \langle K \rangle^2}{\langle K \rangle^2} = \frac{1}{\langle K \rangle} + \sigma_W^2 \ , \qquad (19)$$

where $\sigma_W^2 = 1/M$ is given by formula (7). The ratio of the classical variance to the "photon shot noise" variance is equal to $\delta_c = \langle K \rangle / M$. Parameter δ_c is named as the photocount degeneracy parameter.

When SASE FEL operates in the linear regime, the probability density of the energy after monochromator, $p(W)$, is the gamma distribution (10). Substituting (10) into (18) and performing integration we come to the negative binomial distribution [11]:

$$P(K) = \frac{\Gamma(K+M)}{\Gamma(K+1)\Gamma(M)} \left(1 + \frac{M}{\langle K \rangle}\right)^{-K} \times \left(1 + \frac{\langle K \rangle}{M}\right)^{-M} \ . \qquad (20)$$

It can be shown that the negative binomial distribution tends to the gamma distribution (10) at large values of the photocount degeneracy parameter δ_c.

The formula for calculation of the photocount degeneracy parameter δ_c is given by $\delta_c \simeq \eta R_m \Delta\omega_m N_{ph}(\omega)/M$, where R_m is integral reflection coefficient of the mirrors and dispersive element of the monochromator, N_{ph} is spectral density of photons radiated within one pulse. Peculiar feature of SASE FEL is that the degeneracy parameter is always extremely large. Typical values of δ_c will be about $10^8 \div 10^{10}$ for X-ray FELs, so we can state that classical approach is adequate for description of statistical properties of the radiation from SASE FEL.

Acknowledgement

We wish to thank R. Bonifacio, J. Feldhaus, P. Gürtler, J. Krzywinski, B. Lengeler, G. Materlik, J. Pflüger, J. Roßbach, J.R. Schneider and B. Sonntag for useful discussions.

References

[1] A.M. Kondratenko and E.L. Saldin, Part. Acc. **10**(1980)207.

[2] Ya.S. Derbenev, A.M. Kondratenko and E.L. Saldin, Nucl. Instrum. and Methods **193**(1982)415.

[3] R. Bonifacio, C. Pellegrini and L. Narducci, Opt. Commun. **50**(1984)373.

[4] K.J. Kim, Nucl. Instrum. and Methods **A250**(1986)396.

[5] K.J. Kim, Phys. Rev. Lett. **57**(1986)1871.

[6] J.M. Wang and L.H. Yu, Nucl. Instrum. and Methods **A250**(1986)484.

[7] S. Krinsky and L.H. Yu, Phys. Rev. **A35**(1987)3406.

[8] R. Bonifacio et al., Phys. Rev. Lett. **73**(1994)70.

[9] R. Bonifacio and F. Casagrande, Optics Commun. **50**(1984)251.

[10] R. Bonifacio and F. Casagrande, Nucl. Instrum. and Methods **A237**(1985)168.

[11] J. Goodman, Statistical Optics, (John Wiley and Sons, New York, 1985).

[12] R. Bonifacio et al., Riv. Nuovo Cimento, Vol.13, No.9 (1990).

[13] E.L. Saldin, E.A. Schneidmiller and M.V. Yurkov, Phys. Rep. **260**(1995)187.

Influence of Nonlinear Effects on Statistical Properties of the Radiation from SASE FEL

E.L. Saldin[a], E.A. Schneidmiller[a], M.V. Yurkov[b]

[a] *Automatic Systems Corporation, 443050 Samara, Russia*

[a] *Joint Institute for Nuclear Research, Dubna, 141980 Moscow Region, Russia*

Abstract

The paper presents analysis of statistical properties of the radiation from self amplified spontaneous emission (SASE) free electron laser operating in nonlinear mode. The present approach allows one to calculate the following statistical properties of the SASE FEL radiation: time and spectral field correlation functions, distribution of the fluctuations of the instantaneous radiation power, distribution of the energy in the electron bunch, distribution of the radiation energy after monochromator installed at the FEL amplifier exit and the radiation spectrum. It has been also obtained that statistics of the instantaneous radiation power from SASE FEL operating in the nonlinear regime changes significantly with respect to the linear regime. All numerical results presented in the paper have been calculated for the 70 nm SASE FEL at the TESLA Test Facility being under construction at DESY.

1. Introduction

It is expected that VUV and X-ray free electron lasers [1, 2] will be constructed in the nearest future. The projects of X-ray FELs are developed at SLAC and DESY [3, 4] and 6 nm SASE FEL is under construction at the TESLA Test Facility (TTF) at DESY [5, 6]. An appropriate design of the SASE FELs and planning of user's equipment and experiments depend strongly on the knowledge of the radiation amplification process in the SASE FEL and on the properties of the radiation.

At present there is significant progress in the description of the linear stage of SASE FEL operation in terms of statistical optics (time and spectral correlation functions, time of coherence, interval of spectral coherence, probability density functions of the instantaneous radiation power and of the finite-time integrals of the instantaneous power, probability density function of the radiation energy after the monochromator installed at the exit of SASE FEL) [7]. In particular, it has been shown that the radiation from SASE FEL operating in the linear regime possesses all the features corresponding to completely chaotic polarized radiation: the higher order correlation functions (time and spectral) are expressed via the first order correlation function, the probability density distribution of the instantaneous radiation power follows the negative exponential distribution and the probability density function of the finite-time integrals of the instantaneous power and of the energy after monochromator follows the gamma distribution.

Nevertheless, a reasonable question arises what are the features of the radiation from SASE FEL operating in the nonlinear mode and, in particular, at saturation. This question can be answered only on the base of the results obtained with nonlinear simulation codes. There exist several time-dependent simulation codes [7, 8, 9, 10, 11]. At present, only limited number of SASE FEL characteristics have been calculated. They are average output power [8], correlation time and variation of the energy in the radiation pulse [9]. There was an attempt to calculate radiation spectra, but the accuracy of calculation was not sufficient [11]. In this paper we present complete description of the nonlinear mode of SASE FEL radiation in terms of statistical optics. To be specific, we calculated all the numerical results for the 70 nm SASE FEL at the TESLA Test Facility being under construction at DESY [12]. Nevertheless, they can be simply scaled for calculation of other SASE FELs by applying similarity techniques (see, e.g. ref. [13, 14]).

2. Description of SASE FEL in terms of statistical optics

In all existent time-dependent simulation codes the radiation pulse is simulated by discrete representation of the radiation field $E(z,t)$ with the step in longitudinal coordinate equal to radiation wavelength λ (see, e.g. refs. [8, 9, 10, 11]). Each simulation run starts from original statistical set of initial data and output results change from run to run. To obtain information about general properties of the output radiation one should use statistical methods. It has been shown in ref. [7] that description of SASE FEL in terms of statistical optics is adequate to the problem. In this paper we apply this approach for the description of the nonlinear mode of SASE FEL operation.

To calculate spectral characteristics of the radiation pulse we use Fourier transformation:

$$\bar{E}(z,\omega) = \int\limits_{-\infty}^{\infty} e^{i\omega t}[\tilde{E}(z,t)e^{-i\omega_0 t} + C.C.]dt \ . \qquad (1)$$

The first and the second order time and spectral correlation functions, $g_1(t,t')$, $g_2(t,t')$, $g_1(\omega,\omega')$ and $g_2(\omega,\omega')$, are calculated in accordance with the definitions:

$$\begin{aligned} g_1(t-t') &= \frac{\langle \tilde{E}(t)\tilde{E}^*(t')\rangle}{\left[\langle \mid \tilde{E}(t)\mid^2\rangle\langle\mid \tilde{E}(t')\mid^2\rangle\right]^{1/2}} \ , \\ g_2(t-t') &= \frac{\langle \mid \tilde{E}(t)\mid^2\mid \tilde{E}(t')\mid^2\rangle}{\langle \mid \tilde{E}(t)\mid^2\rangle\langle\mid \tilde{E}(t')\mid^2\rangle} \ , \\ g_1(\omega,\omega') &= \frac{\langle \bar{E}(\omega)\bar{E}^*(\omega')\rangle}{\left[\langle \mid \bar{E}(\omega)\mid^2\rangle\langle\mid \bar{E}(\omega')\mid^2\rangle\right]^{1/2}} \ , \\ g_2(\omega,\omega') &= \frac{\langle \mid \bar{E}(\omega)\mid^2\mid \bar{E}(\omega')\mid^2\rangle}{\langle \mid \bar{E}(\omega)\mid^2\rangle\langle\mid \bar{E}(\omega')\mid^2\rangle} \ , \qquad (2) \end{aligned}$$

where $\langle\ldots\rangle$ means shot-to-shot averaging. The coherence time τ_c [15] and interval of the spectral coherence $\Delta\omega_c$ [7] are calculated as follows:

$$\begin{aligned} \tau_c &= \int\limits_{-\infty}^{\infty} \mid g_1(\tau)\mid^2 d\tau \ , \\ \Delta\omega_c &= \int\limits_{-\infty}^{\infty} \mid g_1(\omega-\omega')\mid^2 d(\omega-\omega') \ . \qquad (3) \end{aligned}$$

Normalized envelope of the radiation spectrum is reconstructed from the first order time correlation function as follows (see refs. [7, 16] for more detail):

$$G(\Delta\omega) = \frac{1}{2\pi}\int\limits_{-\infty}^{\infty} d\tau g_1(\tau)\exp(-i\Delta\omega\tau) \ . \qquad (4)$$

To obtain output characteristics of the radiation from SASE FEL one should perform large number of simulation runs with time-dependent simulation code. The result of each run contains parameters of the output radiation (field and phase) stored in the boxes over the full length of the radiation pulse. At the next stage of numerical experiment the arrays of data should be handled to extract information on statistical properties of the radiation (see eq. (1) – (4)). Probability distribution functions of the instantaneous radiation power, of the finite-time integrals of the instantaneous power and of the radiation energy after the monochromator installed at the exit of SASE FEL are calculated by plotting histograms of large number of statistical data.

3. Results of numerical simulations

In this section we illustrate with numerical example the results of computer modelling of statistical properties of the radiation from SASE FEL operating in nonlinear regime. Simulations have been performed by means of 1-D time-dependent nonlinear simulation code [7, 10] with 100 statistically independent runs. Then the arrays of the output data have been handled with postprocessor codes to extract statistical properties of the SASE FEL radiation.

In Fig. 1a we present the dependence of the average radiation power on the reduced undulator length (solid line). Dotted line in this plot presents the output power for the steady-state FEL amplifier starting with the value of input power of 8 W (corresponding to the value of effective power of shot noise). It is seen that the main difference occurs at the nonlinear stage of amplification. It is seen that the output power of SASE FEL continues to grow due to the spectrum broadening (see ref. [7, 16]). Coherence time, τ_c, decreases drastically in the nonlinear regime (see Fig. 1b).

In Fig. 1c we present the results of calculation of the normalized rms deviation of the instantaneous fluctuations of the radiation power, $\sigma_{\mathrm{P}} = \langle(P-\langle P\rangle)^2\rangle^{1/2}/\langle P\rangle$, as function of the undulator length. One can see from this plot that at the linear stage of the SASE FEL operation the value of the deviation is equal to unity. It has been shown in refs. [7, 17] that in this case the probability density distribution of the radiation power is described by the negative exponential law. In the nonlinear mode of operation the deviation of the power fluctuations differs significantly ¿from unity. It indicates that the probability density function should differ from the negative exponential law. Fig. 2 presents the distributions of the instantaneous radiation power at different undulator lengths. It is seen that this distribution near the saturation point (upper right plot) differs cardinally from a negative exponential one. Nevertheless, in the deep nonlinear regime the power distribution tends again to the negative exponential one and the value of the rms deviation also tends to unity (see Fig. 2, lower right plot).

We performed numerical study of the fluctuations of the energy in the radiation pulse integrated over finite time. Fig. 1d presents the normalized rms deviation of the energy fluctuations in the radiation pulse as function of the undulator length. It is seen that the fluctuations achieve their maximum in the end of linear regime. The first local minimum corresponds to the saturation point. This is in a good agreement with Fig. 1c showing that relative fluctuations of the instantaneous radiation power achieve their minimum at the saturation point.

In Fig. 2 we present the results of calculations of the first and the second order time correlation functions. It is seen that there is significant difference with respect to the linear mode of operation (see ref. [17]). First, we obtain that relation $g_2(\tau) = 1 + |g_1(\tau)|^2$ does not takes place in the nonlinear regime. Second, the first order time correlation function begins to have two maxima at the increase of the undulator length (which is connected with the shape of the radiation spectrum (see ref. [7, 16] for more detail).

From practical point of view it is important to know characteristics of the output radiation from SASE FEL operating at saturation. Fig. 3a presents distribution of the instantaneous power at saturation point. In Fig. 3b we present the results of calculations of the first and the second order time correlation functions. In Fig. 3c we present the histogram of the probability density distribution of the radiation energy after the monochromator. The width of the monochromator is less than the interval of spectral coherence (3). It is seen from this plot that at a small window of the monochromator the fluctuations of the radiation energy follow the negative exponential law. We also performed calculations of the first and the second order spectral correlation functions for the radiation of SASE FEL operating at saturation (see Fig. 3d). Solid circles in this plot correspond to to the spectral correlation functions of the radiation pulse from SASE FEL operating in linear regime [7, 17]. With the accuracy of performed calculation we can state that spectral correlation functions are the same as those for the linear mode of the SASE FEL operation.

4. Conclusion

We have shown in this paper that description of SASE FEL radiation in terms of statistical optics (time and spectral correlation functions, time of coherence, interval of spectral coherence, probability density functions of the instantaneous radiation power and of the finite-time integrals of the instantaneous power, probability density function of the radiation energy after the monochromator installed at the exit of SASE FEL) is adequate for the problem. All these characteristics of SASE FEL operating in the nonlinear regime are presented in the paper. It has been also obtained that statistics of the instantaneous radiation power from SASE FEL operating in the nonlinear regime changes significantly with respect to the linear regime. Precise calculations of the time correlation functions have shown their complicated behaviour. In particular, it has been found that the relation $g_2(\tau) = 1 + |g_1(\tau)|^2$ is not fulfilled in the nonlinear regime. On the other hand, the spectral correlation functions and distribution of the radiation energy after monochromator calculated in the saturation point are the same as in the linear regime (see ref. [7]).

References

[1] Ya.S. Derbenev, A.M. Kondratenko and E.L. Saldin, Nucl. Instrum. and Methods **193**(1982)415.

[2] J.B. Murphy and C. Pellegrini, Nucl. Instrum. and Methods **A237**(1985)159.

[3] R. Tatchyn et al., Nucl. Instrum. and Methods **A375**(1996)274.

[4] Linear Collider Conceptual Design Report, DESY print, April 1997.

[5] "A VUV Free Electron Laser at the TESLA Test Facility: Conceptual Design Report", DESY Print TESLA-FEL 95-03, Hamburg, DESY, 1995.

[6] J. Rossbach, Nucl. Instrum. and Methods **A375**(1996)269.

[7] E.L. Saldin, E.A. Schneidmiller and M.V. Yurkov, "Statistical Properties of Radiation from VUV and X-ray Free Electron Laser", DESY print TESLA-FEL 97-02, Hamburg, 1997.

[8] R. Bonifacio et al., Phys. Rev. Lett. **73**(1994)70.

[9] P. Pierini and W. Fawley, Nucl. Instrum. and Methods **A375**(1996).

[10] E.L. Saldin, E.A. Schneidmiller and M.V. Yurkov, "Simulation Studies of 6 nm Free Electron Laser at the TESLA Test Facility Starting from Noise", DESY print TESLA-FEL 96-07, Hamburg, 1996.

[11] W.M. Fawley, SPIE Proceedings **2988**(1997)98.

[12] W. Brefeld et al., "Parameter Study on Phase I of the VUV FEL at the TESLA Test Facility", DESY Print TESLA-FEL 96-13, to be published in Nucl. Instrum. and Methods (Proc. of 19th FEL Conf.).

[13] R. Bonifacio et al., Riv. Nuovo Cimento, Vol.13, No.9 (1990).

[14] E.L. Saldin, E.A. Schneidmiller and M.V. Yurkov, Phys. Rep. **260**(1995)187.

[15] L. Mandel, Proc. Phys. Soc. (London), 1959, v.74, p.223.

[16] E.L. Saldin, E.A. Schneidmiller and M.V. Yurkov, "Possible Application of Fourier Spectroscopy for Precise Reconstruction of the Radiation Spectrum from SASE FEL", these Proceedings.

[17] E.L. Saldin, E.A. Schneidmiller and M.V. Yurkov, "Statistical Properties of the Radiation from SASE FEL Operating in the Linear Regime", these Proceedings.

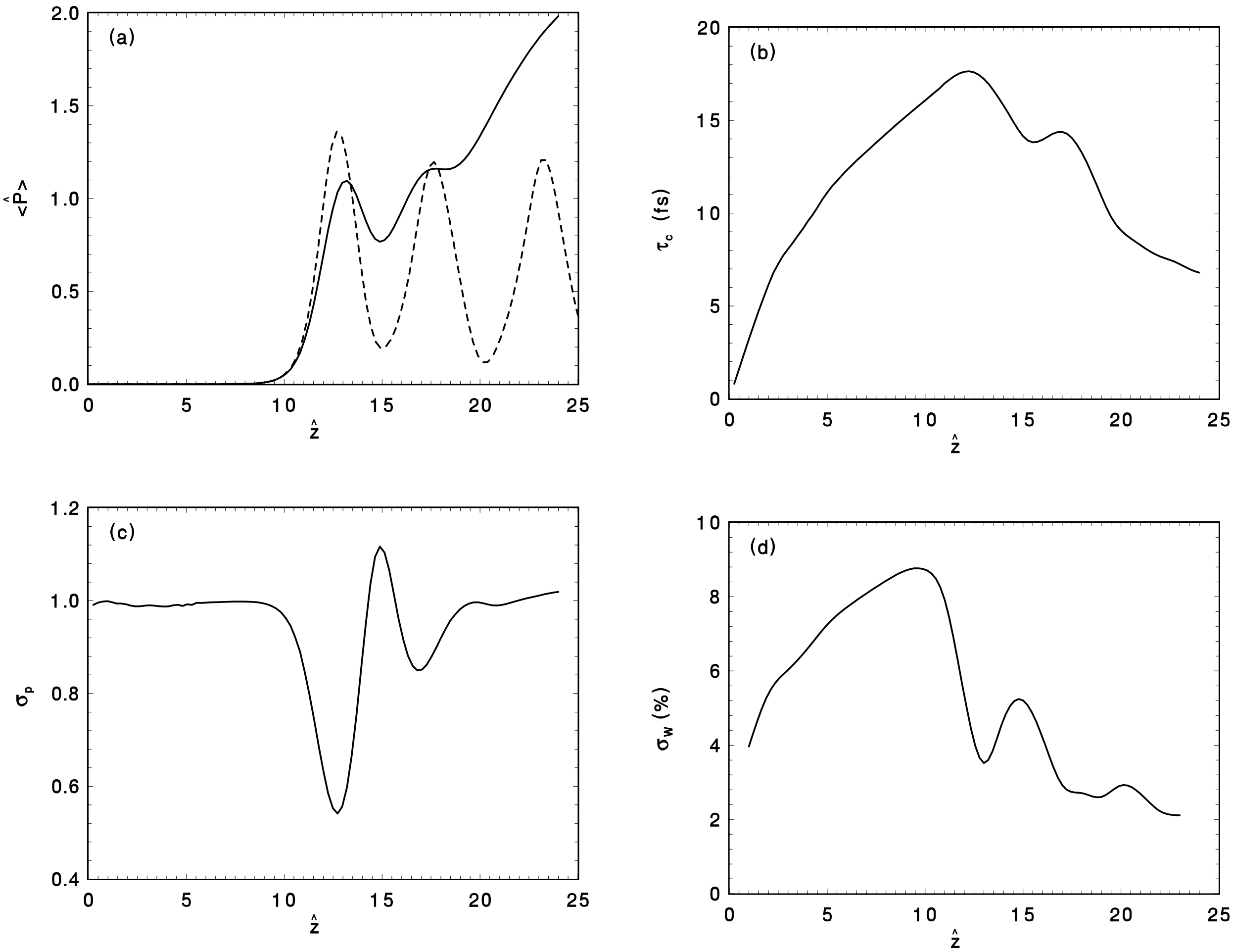

Fig. 1. Averaged characteristics of SASE FEL as function of undulator length: averaged output power (plot (a)), coherence time (plot (b)), normalized rms deviation of the instantaneous fluctuations of the radiation power (plot (c)) and normalized rms deviation of the energy fluctuations in the radiation pulse (plot (d)).

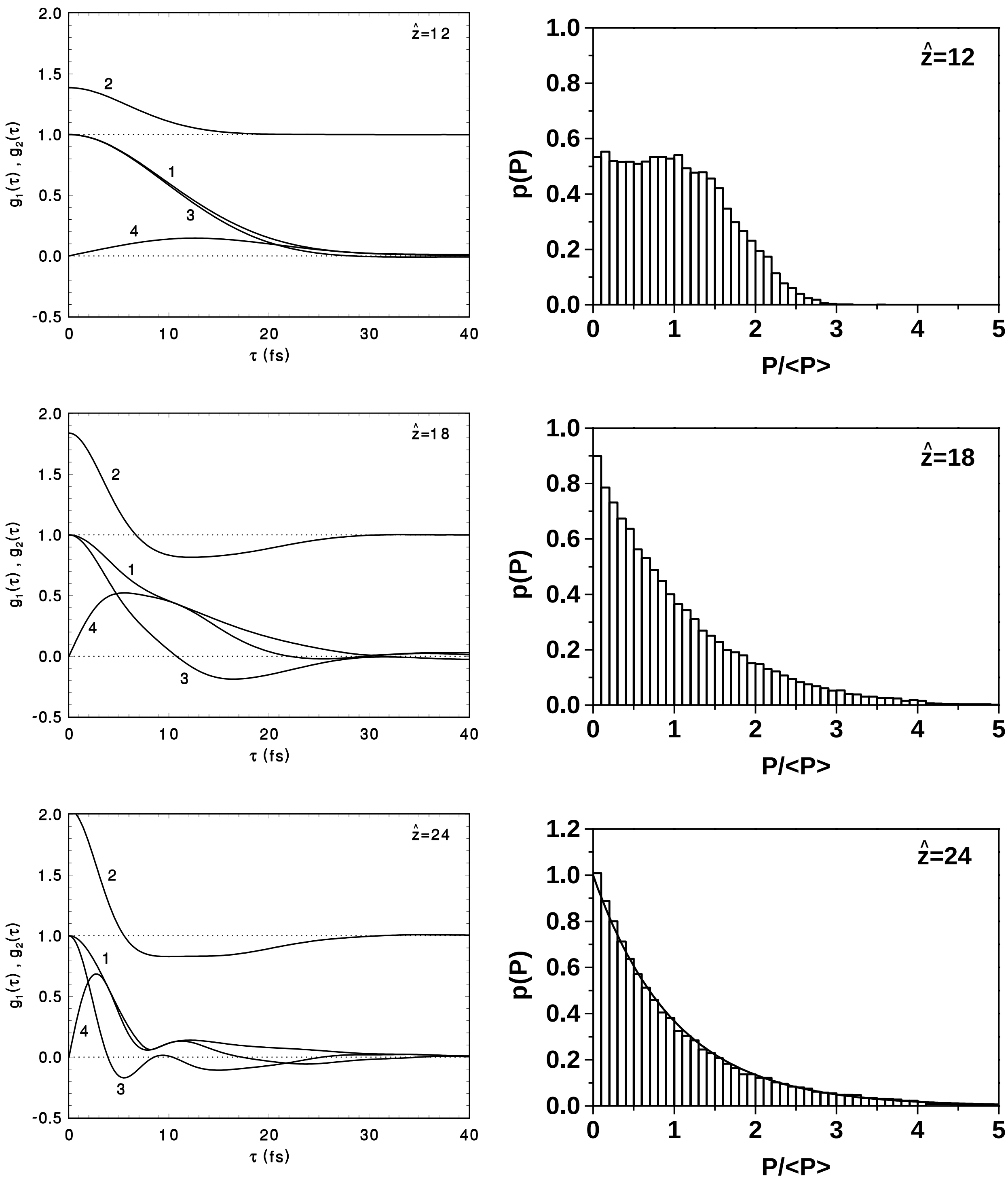

Fig. 2. The first and the second order time correlation functions, $|g_1(\tau)|$ (curve 1), $g_2(\tau)$ (curve 2), $\mathrm{Re}(g_1(\tau))$ (curve 3) and $\mathrm{Im}(g_1(\tau))$ (curve 4) of the radiation pulse (at left) and histograms of the probability density distribution, $p(P)$, of the instantaneous output power at different reduced length of the FEL amplifier (at right). Calculations have been performed with nonlinear simulation code over 10^4 independent statistical events. $\langle P \rangle$ denotes the average power.

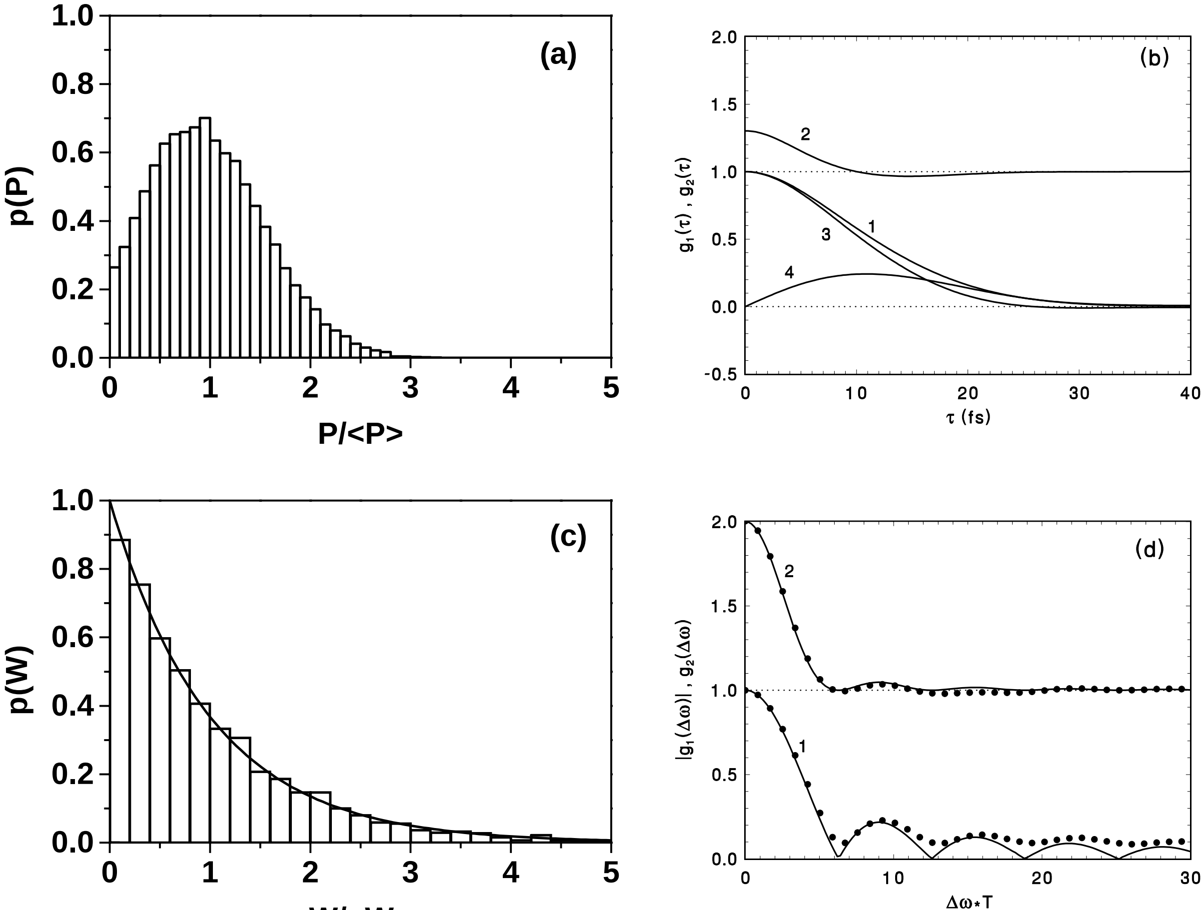

Fig. 3. Characteristics of the output radiation from SASE FEL operating at saturation: probability density function of the instantaneous radiation power (plot (a)), the first and the second order time correlation functions, $|g_1(\tau)|$ (curve 1), $g_2(\tau)$ (curve 2), $\mathrm{Re}(g_1(\tau))$ (curve 3) and $\mathrm{Im}(g_1(\tau))$ (curve 4) (plot (b)), a histogram of the probability density distribution, $p(W)$, of the radiation energy after narrow bandwidth monochromator (plot (c)) and the first and the second order spectral correlation functions, $|g_1(\Delta\omega)|$ (curve 1)and $g_2(\Delta\omega)$ (curve 2) (plot (d)).

Possible Application of Fourier Spectroscopy for Precise Reconstruction of the Radiation Spectrum from SASE FEL

E.L. Saldin[a], E.A. Schneidmiller[a], M.V. Yurkov[b]

[a] *Automatic Systems Corporation, 443050 Samara, Russia*

[a] *Joint Institute for Nuclear Research, Dubna, 141980 Moscow Region, Russia*

Abstract

This paper presents a method for numerical calculation of the radiation spectrum from SASE FEL. The idea of the method is similar to that used in Fourier spectroscopy when the radiation spectrum is reconstructed using Fourier transformation of the first order time correlation function. Proposed numerical method is universal and can be applied for linear and nonlinear modes of SASE FEL operation.

1. Introduction

A self amplified spontaneous emission free electron laser (SASE FEL) [1, 2, 3, 4] is considered now as future source of coherent VUV and X-ray radiation. An appropriate design of the SASE FEL and planning of user's equipment and experiments depend strongly on the knowledge of the radiation amplification process in the SASE FEL and on the properties of the radiation. Recently it has been achieved significant success in the analytical description of a high gain SASE FEL [5]. Nevertheless, analytical techniques are of limited possibilities in the description of SASE FEL process in a general case, so numerical simulation codes should be developed. At present there exist several time-dependent simulation codes developed by different teams [5, 6, 7, 8, 9]. Common feature of these codes is that they produce an output of data for discrete representation of the radiation field. Then these data should be handled to extract different information about the properties of the SASE FEL radiation.

In this paper we describe a method for precise reconstruction of the radiation spectrum from numerical simulation data. Calculation of the radiation spectrum proceeds in three steps. First, several runs of time-dependent FEL simulation code are performed. The result of each run contains parameters of the output radiation (amplitudes and phases of the electromagnetic field). Second, the first order time correlation function is calculated from these statistical data. At the final step spectrum of the radiation from SASE FEL is reconstructed using Fourier transformation of the first order time correlation function. This method is universal and can be applied for linear and nonlinear modes of SASE FEL operation.

2. Method for time-dependent simulation

Time-dependent algorithm for the simulation of the FEL amplifier should take into account the slippage effect which connected with the fact that electromagnetic wave moves with the velocity of light c, while the electron beam moves with the longitudinal velocity v_{z}. Electron motion in the undulator is a periodic one, so the radiation of each electron $E(z,t)$ is also periodic function:

$$E(z,t) = f(z-ct) = f(z-ct+\lambda) \ ,$$

with period

$$\lambda = \lambda_{\mathrm{w}} \frac{c - v_{\mathrm{z}}}{v_{\mathrm{z}}} \simeq \frac{\lambda_{\mathrm{w}}}{2\gamma_{\mathrm{z}}^2} = \lambda_{\mathrm{w}} \frac{1 + K^2/2}{2\gamma^2} \ ,$$

where λ_{w} is the undulator period, K is undulator parameter, γ is relativistic factor and $\gamma_{\mathrm{z}}^2 = \gamma^2/(1 + K^2/2)$.

It seems to be natural to construct the following algorithm [6]. Suppose, we have electron bunch of length l_{b}. We divide this length into $N_{\mathrm{b}} = l_{\mathrm{b}}/\lambda$ boxes. FEL equations are used in each box for calculation of the

TESLA FEL-Report 1997-06

motion of the electrons and evolution of the radiation field within one undulator period. The using of steady-state FEL equations averaged over undulator period is justified by the fact that FEL amplifier is resonance device with a narrow bandwidth. Then we should take into account the slippage effect, i.e. that electromagnetic radiation advances the electron beam by the wavelength λ while electron beam passes one undulator period. It means that the radiation which interacted with the electrons in the j th box slips to the electrons located in the next, $j+1$ th box. Then procedure of integration is repeated, etc.

This algorithm allows one to calculate the values of radiation field for each box as function of longitudinal coordinate z. Time dependence of the radiation field has the form:

$$E(z,t) = \tilde{E}(z,t)e^{-i\omega_0(z/c-t)} + C.C. \qquad (1)$$

at any position along the undulator. Here we explicitly segregated slowly varying complex amplitude $\tilde{E}(z,t)$. At any fixed point z along the undulator the time interval between the arrival of the radiation connected with adjacent boxes is equal to $\Delta t = t_{j+1} - t_j = \lambda/c$, so we have discrete representation of $\tilde{E}(z,t_j)$. To calculate spectral characteristics of the radiation we use Fourier transformation:

$$\bar{E}(z,\omega) = \int\limits_{-\infty}^{\infty} e^{i\omega t}[\tilde{E}(z,t)e^{-i\omega_0 t} + C.C.]dt \ . \qquad (2)$$

The first order time correlation function, $g_1(t,t')$, is calculated in accordance with the definitions:

$$g_1(t-t') = \frac{\langle \tilde{E}(t)\tilde{E}^*(t')\rangle}{\left[\langle \mid \tilde{E}(t)\mid^2\rangle\langle\mid \tilde{E}(t')\mid^2\rangle\right]^{1/2}} \ , \qquad (3)$$

where $\langle\ldots\rangle$ means shot-to-shot averaging. Normalized envelope of the radiation spectrum and the first order time correlation function are connected by the relation [10]:

$$G(\Delta\omega) = \frac{1}{2\pi}\int\limits_{-\infty}^{\infty} d\tau g_1(\tau)\exp(-i\Delta\omega\tau) \ . \qquad (4)$$

To obtain output characteristics of the radiation from SASE FEL one should perform large number of simulation runs with time-dependent simulation code. The result of each run contains parameters of the output radiation (field and phase) stored in the boxes over the full length of the radiation pulse. At the next stage of numerical experiment the arrays of data should be handled to extract information on statistical properties of the radiation.

3. Results of numerical simulations

Fig. 1 presents typical time structure of a radiation pulse and its spectrum when a SASE FEL operates in the high gain linear regime. The time and spectral structure of the radiation pulse change from shot to shot and the information about the properties of the radiation can only be obtained by statistical analysis of a series of shots. A visual analysis of the spectrum of the radiation pulse for several shots (see Fig. 1b) indicates that the spikes in the spectrum are approximately inside some envelope. The straightforward way to obtain this envelope is to average a large number of spectral data. In Fig. 2a we present the spectrum of SASE FEL radiation averaged over 2400 shots (piecewise curve). It is seen that even at such a number of independent runs the accuracy of the reconstructed spectrum is not excellent and the errors in the spectrum are still visible.

Another technique for obtaining the envelope of the spectrum consists in its reconstruction from the first order time correlation function (4). It should be no-

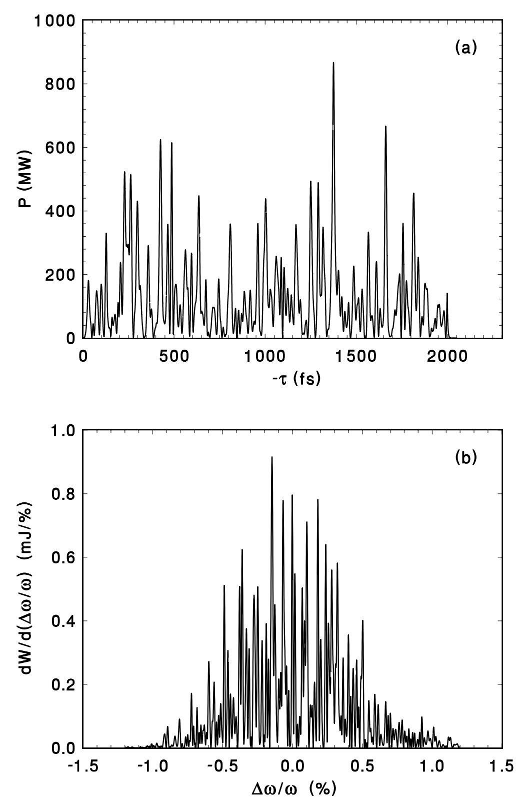

Fig. 1. Typical temporal structure (graph (a)) and spectrum of the radiation pulse (graph (b)) from SASE FEL operating in high gain linear regime. Calculations have been performed with the linear simulation code.

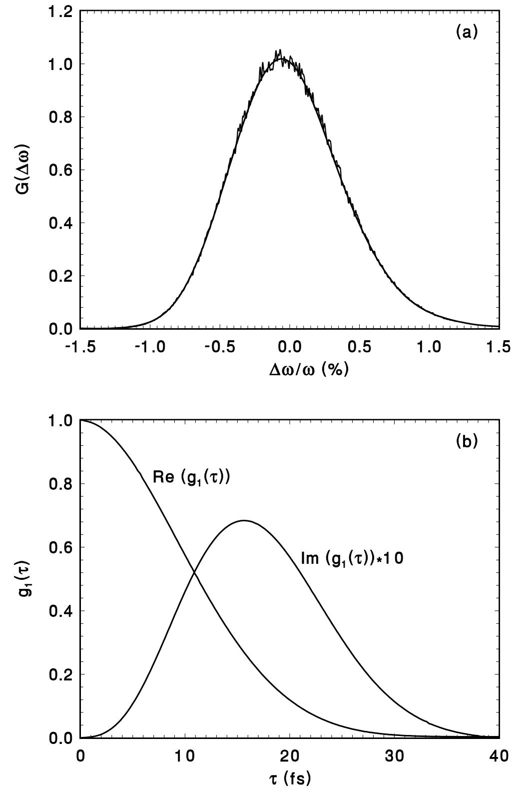

Fig. 2. Normalized spectrum of the radiation from SASE FEL, $G(\Delta\omega)$, at $\hat{z} = 11$ (graph (a)). Averaging has been performed over 2400 shots. Smooth curve is the result of spectrum reconstruction using the first order time correlation function presented in graph (b)). Calculations of the first order time correlation function have been performed with linear simulation code over 5×10^4 independent statistical events.

ticed that the first order time correlation function is calculated with much higher accuracy. This is connected with the fact that the statistics for the correlation function calculations is larger by a factor of the number of spikes in the bunch. The data from Fig. 2b have been used for the spectrum reconstruction (solid curve in Fig. 2a). It is seen that this technique gives very precise results. It is our experience that this technique allows almost perfect reconstruction of the spectrum at the number of runs of several tens.

In conclusion, we present evolution of the radiation spectrum from SASE FEL from the beginning up to deep nonlinear regime. Longitudinal coordinate is normalized in accordance with ref. [3, 5, 6]. The normalized position $\hat{z} = 13$ corresponds to saturation point. Simulations have been performed with nonlinear simulation code using 100 shots. The temporal structures of the radiation pulses have been used for calculating

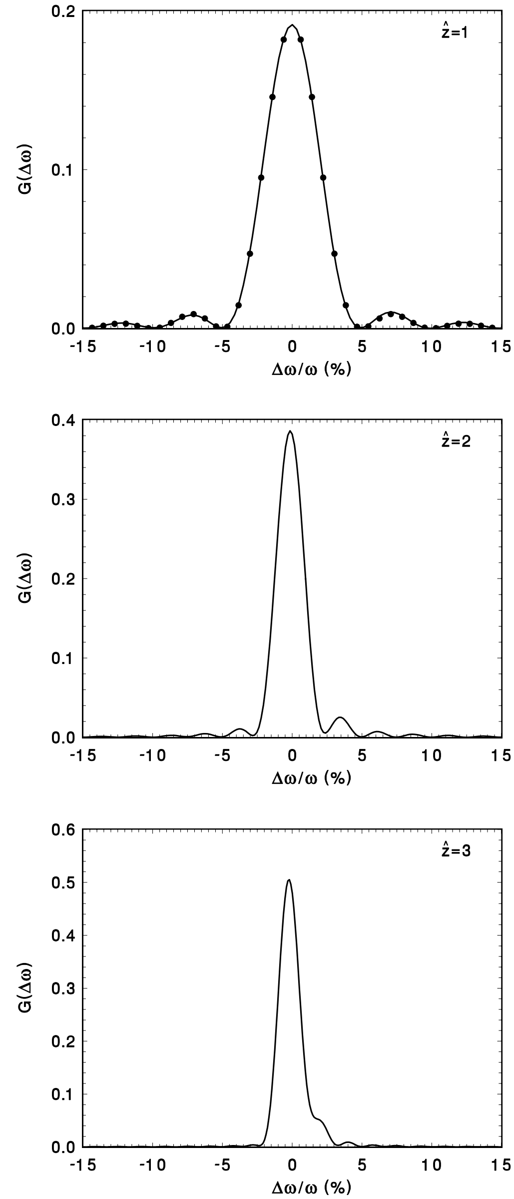

Fig. 3. Evolution of the radiation spectrum $G(\Delta\omega)$ from SASE FEL at the initial stage of amplification. Calculations have been performed with linear simulation code over 100 shots. Spectrum has been reconstructed from the first order time correlation function. Circles correspond to normalized spectrum of the undulator radiation.

the first order time correlation function. Then the radiation spectra have been reconstructed by Fourier transformation of the first order time correlation function. Figure 3 shows the evolution of the radiation spectrum at the beginning of the amplification process with the step equal to one field gain length. After the first gain length the spectrum of the SASE FEL is

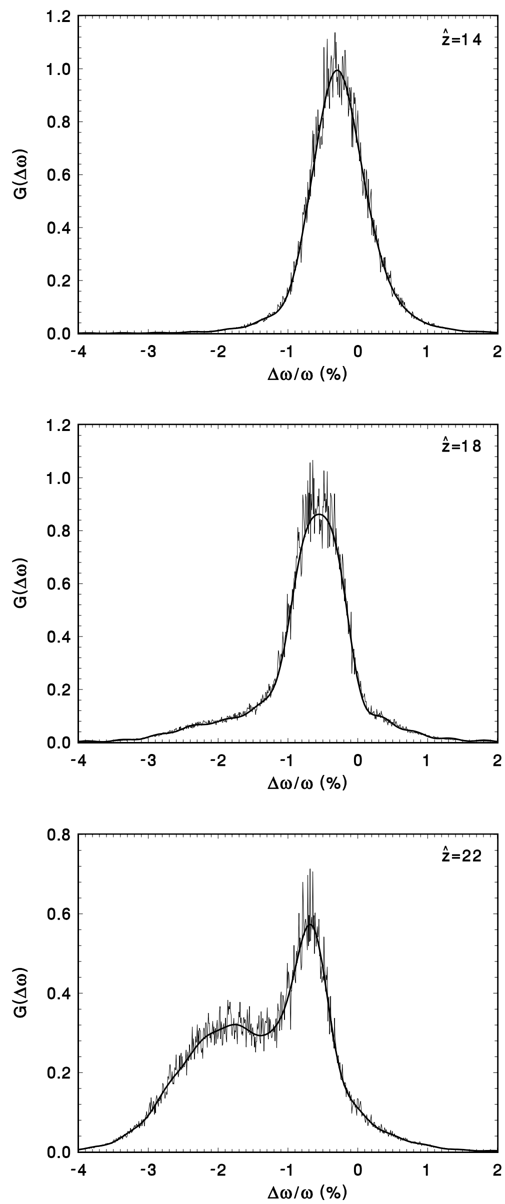

Fig. 4. Evolution of the radiation spectrum $G(\Delta\omega)$ from SASE FEL operating in the nonlinear regime. Calculations have been performed with nonlinear simulation code over 100 shots. Smooth curves are the results of spectrum reconstruction from the first order correlation function. Piecewise curves are the results of straightforward averaging of the radiation spectra.

identical to the spectrum of the undulator radiation. After several gain lengths the spectrum transforms to that of the high gain FEL amplifier (see also Fig. 2). In Fig. 4 we present the results of calculations of the radiation spectrum from SASE FEL operating in nonlinear regime. Smooth curves in these plots are the results of spectrum reconstruction from the first order correlation function. Piecewise curves are the results of straightforward averaging of the radiation spectra over 100 shots. It is seen that spectrum reconstruction using Fourier spectroscopy provides much more higher accuracy.

References

[1] A.M. Kondratenko and E.L. Saldin, Part. Acc. **10**(1980)207.

[2] Ya.S. Derbenev, A.M. Kondratenko and E.L. Saldin, Nucl. Instrum. and Methods **193**(1982)415.

[3] R. Bonifacio, C. Pellegrini and L. Narducci, Opt. Commun. **50**(1984)373.

[4] J.B. Murphy and C. Pellegrini, Nucl. Instrum. and Methods **A237**(1985)159.

[5] E.L. Saldin, E.A. Schneidmiller and M.V. Yurkov, "Statistical properties of radiation from VUV and X-ray free electron laser", DESY print TESLA-FEL 97-02, Hamburg, 1997.

[6] R. Bonifacio et al., Phys. Rev. Lett. **73**(1994)70.

[7] P. Pierini and W. Fawley, Nucl. Instrum. and Methods **A375**(1996).

[8] E.L. Saldin, E.A. Schneidmiller and M.V. Yurkov, "Simulation Studies of 6 nm Free Electron Laser at the TESLA Test Facility Starting from Noise", DESY print TESLA-FEL 96-07, Hamburg, 1996.

[9] W.M. Fawley, SPIE Proceedings **2988**(1997)98.

[10] J. Goodman, Statistical Optics, (John Wiley and Sons, New York, 1985).

Beam Dynamics of the DESY FEL Photoinjector Simulated with MAFIA and PARMELA

Min Zhang
Deutsches Elektronen-Synchrotron (DESY) -MPY-, Notkestr. 85, 22603 Hamburg, Germany

Abstract– **We present a wake field simulation of the DESY FEL [1] gun by using the MAFIA self-consistent solver TS2. It has been found that the wake field induced emittance degradation is not very significant. Different options of emittance-conserving beam transport using triplets, doublets, or solenoids are discussed. The solenoid option appears to be the best, thanks to the space charge compensation.**

I. Introduction

For low emittance guns the wake field is a big issue. There are already many gun simulations which address the dynamics of the beam in a non-self-consistent way with no physical boundaries included. There is increasing concern about the effects of wake fields on beam emittances. In this context, we present a self-consistent wake field simulation with full gun geometry using the MAFIA Finite Difference Time Domain Particle-In-Cell (FDTD/PIC) solver TS2.

It is important to be able to conserve the emittance of a beam while it is transported over long distances. Several options are discussed using triplets, doublets, or solenoids.

II. MAFIA Wake Field Simulation

The gun geometry is shown in Fig. 1, where the accelerating gradient at the cathode is $E_h = 50\text{MV/m}$, the final beam energy $E = 5\text{MeV}$, the injection phase $\phi_{rf} = 32^o$, the laser FWHM=10ps, and the maximum on-axis $B_z = 2080\text{G}$. Since the initial bunch length was 0.43mm, a mesh with a total number of points equal to 990,000 was employed. A total of 5800 macro particles were generated and the simulation took 53 cpu hours on a SUN workstation. The error numbers for the run are:

$$\eta_t = 10\frac{(\delta t)^2 T}{\tau^3} = 10 \times \frac{(9.6\times 10^{-14})^2 \times 1.086\times 10^{-9}}{(10^{-11})^3} \approx 0.1$$

$$\eta_r = 10\frac{(\delta r)^2 L_r}{\lambda_r^3} \approx 6$$

$$\eta_z = 10\frac{(\delta z)^2 L_z}{\lambda_z^3} \left\{ \begin{array}{ll} 5 \rightarrow 0.05 & z = 0 \rightarrow 2\text{cm} \\ 6 & z = 2 \rightarrow 25\text{cm} \end{array} \right.$$

If a simulation satisfies $\eta_t < 0.1$ and $\eta_s < 5$, the results will be reasonably accurate.

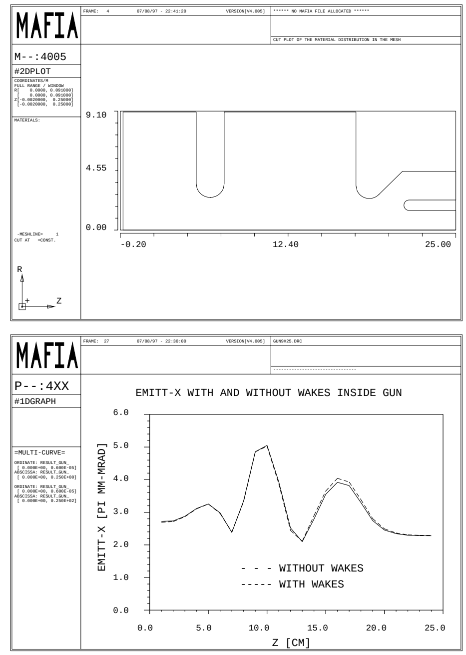

Fig. 1: Upper: DESY FEL Gun with Coaxial RF Input; Lower: Emittance with and without Wakes

Since TS2 is a 2D solver employing $r\phi$ geometry, we use the following relation to evaluate the transverse emittances:

$$(2\epsilon_x)^2 = \epsilon_r{}^2 + \epsilon_\phi{}^2,$$

with

$$\epsilon_r = \sqrt{< r^2 >< p_r^2 > - < rp_r >^2},$$

$$\epsilon_\phi = \sqrt{< r^2 >< p_\phi^2 >}.$$

For the two runs, with and without wake fields, the numerical settings, such as mesh sizes, particle numbers, integration time steps and ultimately, the error numbers were approximately the same. The emittances inside the gun are presented in Fig. 1. It is seen that there is only a very slight difference between the two. What is more interesting is that the one with wake fields is smaller than that without. There are two possible explanations for this. One is numerical, the other physical. The open absorbing boundary condition for the non-wake case is not perfect for all frequency components, causing some reflections from the boundary, which act back on the bunch. If this is ruled out, the following physical explanation will be more convincing. Non-linear contributions of the wake fields behave in a similar "favorable" way to the space charge forces in the emittance compensation process [2].

Due to the results of this simulation, we can now be more confident of the results obtained by non-wake simulations, like those with PARMELA. We can eventually rely on faster space charge based algorithms. However, at high energies, wake field emittance dilutions can be significant, for example, through port step junctions or bunch compressors.

III. Emittance Conserving Beam Transport

In the DESY FEL injector there exists a long beam transport section of 7 meters from the minimum emittance to the first main accelerator (Fig. 2). In order to avoid

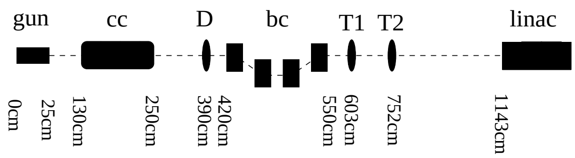

Fig. 2: Beam Line Layout for DESY FEL Injector

emittance increase over this section, one has to apply appropriate focusing elements along the line. Three versions have been investigated with PARMELA: two triplets (T1 and T2), one doublet (at T1), or one solenoid (at T1). Table I lists the emittances measured at 12 m for all the cases. The beam coming from the gun is round and emittance symmetrical. It reaches the minimum emittance of 0.9 π mm-mrad at about 5.2 m from the cathode. Without any focusing elements, the emittance would drift gradually up to 2.5 π mm-mrad.

TABLE I

Emittance Measured At Linac Entrance

Setup (10K particles)	$\epsilon_x^n/\epsilon_y^n$ (π mm-mrad)
Two triplets (T1 & T2)	2.3/1.9
One doublet at T1	1.4/1.8
Solenoid shielded Neumann	1.3/1.4 No fringe B_z
Solenoid shielded 2cm hole	1.4/1.5 Small fringe B_z
Solenoid shielded 3cm hole	1.4/1.5 Small fringe B_z

Note: BC is switched off.

The version with two thick triplets, each of size DOFOD=8cm-6cm-14cm-6cm-8cm, seems to be the worst. The lowest emittances ($\epsilon_x^n/\epsilon_y^n$) achieved are 2.3/1.9 π mm-mrad. The emittances are not symmetrical and moreover, they are usually hard to control.

A better choice would be a thin doublet. By using a FOD doublet of size 5cm-3cm-5cm with a gradient of 500 G/cm, we are able to reduce the emittances to 1.4/1.8 π mm-mrad, although symmetry is still a problem.

With the effectiveness of the solenoid driven space charge compensation in a gun in mind, one automatically turns to solenoids in place of quadrupoles. In addition, solenoid focusing is symmetrical by nature. These two advantages make the solenoid version the best choice. The space charge compensation process along a beam line is exactly the same as that after a gun with respect to the phase space precession (Fig. 3).

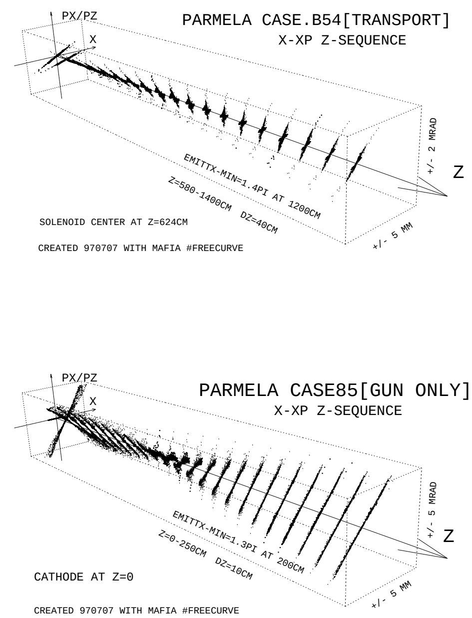

Fig. 3: Upper: 3D $x-x'$ Space Charge Compensation Process along Beam Line; Lower: Emittance Compensation Process after Gun

IV. Conclusion

We have presented a wake field simulation of the DESY FEL low emittance gun by using the MAFIA FDTD-based self-consistent solver TS2. It was found that the wake field induced emittance growth is quite small. Thus space charge codes are usually accurate enough for such gun simulations.

It has been seen that solenoids are best suited for conserving the beam emittances of a symmetric beam along transport lines, when beam emittance is a primary concern. This is, in fact, an extension of the space charge compensation technique to beam lines.

References

[1] "A VUV free electron laser at the TESLA test facility at DESY, Conceptual design report", *DESY Print*, **TESLA-FEL 95-03**, June 1995

[2] Carlsten, B.E., "New photoelectric injector design for the Los Alamos National Laboratory XUV FEL accelerator", *Nucl. Instr. and Meth.*, A285 (1985)